Measurement of the Decay Asymmetries of the Omega-Minus Baryon

A THESIS
SUBMITTED TO THE FACULTY OF THE GRADUATE SCHOOL
OF THE UNIVERSITY OF MINNESOTA
BY

Gerald Michael Guglielmo

IN PARTIAL FULFILLMENT OF THE REQUIREMENTS
FOR THE DEGREE OF
DOCTOR OF PHILOSOPHY

August, 1994

Measurement of the Decay Asymmetries of the Omega-Minus Baryon

by Gerald Michael Guglielmo
Under the supervision of Professor Kenneth J. Heller

ABSTRACT

In an experiment at Fermilab, samples of Ω^-s produced by polarized and unpolarized 400 GeV neutral beams have been collected using a multi-wire proportional chamber and magnetic spectrometer. The data consisted of both polarized and unpolarized samples of Ω^- baryons. These samples were used to measure the decay asymmetry parameters for the decay $\Omega^- \to \Lambda K^-$. An analysis of 252,000 Ω^- baryons has yielded a measurement of 0.0126 ± 0.0042 for the decay asymmetry $\alpha_\Lambda \alpha_{\Omega^-}$. Using a polarized sample of 234,600 Ω^- baryons the $\beta_{\Omega^-}/\gamma_{\Omega^-}$ ratio, ϕ_{Ω^-}, has been measured to be $-3.4° \pm 10.3°$. The results for the sign of the asymmetry parameter γ_{Ω^-} favored a positive value, but were inconclusive.

Acknowledgements

Without the help of many people the work for this dissertation could not have been completed. High energy physics experiments require a combined effort on the part of many people in all stages of the experiment.

The entire Fermilab staff deserves credit for making the fixed target run a success. I would like to personally thank the Fermilab Data Acquisition Software Group, especially Eileen Berman and Carmenita Moore, for their help in setting up and maintaining our data acquisition system. The efforts of the accelerator and the fixed target operations people, for delivering beam often 24 hours a day over the many months the experiment ran, are greatly appreciated.

Kam-Biu Luk and Tom Diehl have provided a great deal of help over the past several years. Jeff Duryea authored the second pass reconstruction and helped modify it for E800. Keith Thorne was always willing to help with the theory of weak decays and using Tex. Ken Heller, my advisor, played a vital role in getting the experiment approved and allowed the graduate students a great deal of freedom. Gina Rameika tuned the beam and showed that the neutral collimator was not too narrow. I am extremely grateful to Ken Johns for all his help throughout my years in graduate school and I consider myself lucky to have him as a friend and colleague. Pete Border provided invaluable help with the really strange hardware problems and many conversations about toys. To Dave Woods and Noah Wallace, friends and fellow graduate students, thanks for being there

when I needed you and thanks for all the good times at work and at play. Thanks to G. Allan, A. Ayala-Mercado, D. Ciampa, V. DeCarlo, D. Fein, Y. T. Gao, S. Hansen, M. J. Longo, J. Jalilian-Marian, E. James, and T. Tynan for their contributions. Crow, Tom, Hobbes, Dogbert, Mickey, Woody and Sir Oinks Latin for providing endless hours of amusement and laughter.

Finally I wish to thank my relatives and friends who, whether they realize it or not, helped me through the hardest stages of this long journey. Thanks Joe, John and Jim for being great brothers. Thanks mom and dad, for your love and support my entire life. To Eileen, your love and faith in me has helped more than I can put in words except to say I love you.

Dedication

This dissertation is dedicated to all teachers who put in the extra effort to make a difference, especially Ms. Johnson who made a difference in my life when it really mattered.

Table of Contents

List of Tables

List of Figures

Chapter 1

Introduction

1.1 Introduction

High energy physics is the study of the fundamental constituents of nature and the forces that govern their interactions. Much of the information known today in the field has come from the study of the decay properties of elementary particles. As far as we know, quarks are elementary particles which decay via the weak force. The study of the decay properties of quarks has provided valuable insights into the weak force. Because quarks are not free, their decays have to be observed while they are bound inside a hadron where the strong force between quarks greatly influences their decay properties. Thus, although quark decay is caused by the weak interaction, their decay inside hadrons is modified by the strong force.

The Ω^- decay is an important decay to study for several reasons. First, the Ω^- is composed of quarks of the same flavor , three strange quarks, and thus provides a good means of studying the decay of the strange quark. Second, the Ω^- is assumed to be a spin-$\frac{3}{2}$ particle and is the only 'stable' spin-$\frac{3}{2}$ baryon. Finally, the decays of the Ω^- have not been studied in great detail and therefore should provide useful new information in a area were the knowledge is sparse.

1.2 Nonleptonic Hyperon Decays

Even though the weak interaction is well understood, the decay properties of strange quarks inside hadrons are not. One way of studying strange quark decay is through the decay of hyperons, baryons which contain at least one strange quark. The dominant mode of these decays is for a strange (s) quark in the parent hyperon to be converted into an up (u) or down (d) quark as the hyperon itself decays into a meson and a baryon. The dominant decay modes for spin-$\frac{1}{2}$ hyperons, except for the Σ^0 which decays electromagnetically, all have a π meson in the final state and so the decays are usually represented by $B_i \rightarrow B_j\pi$. The Dominant decay mode for the Ω^-, a hyperon with an assumed spin of $\frac{3}{2}$, is $\Omega^- \rightarrow \Lambda K^-$.

The basic Feynman diagrams for the nonleptonic decays of spin-$\frac{1}{2}$ hyperons are shown in Figure 1.1 for quark annihilation, quark decay, and the penguin diagrams for one gluon exchange. The "W" in the diagrams is a charged vector boson, represented by a dashed line, which carries the weak force. The "g" in the the penguin diagrams is the gluon. The gluon is the carrier of the strong force and is represented by a curly line. Note that the Ω^-, like the Σ^- and Ξ^-, does not have an annihilation diagram. The basic interaction diagrams for the decay $\Omega^- \rightarrow \Lambda K^-$ are shown in Figure 1.2. While progress has been made in understanding the qualitative nature of these decays, the ability to quantitatively predict the influence of the strong force on the nonleptonic weak decays of hyperons has not been achieved. More experimental data could help this situation.

Conservation of angular momentum (l) plays an important role in understanding these decays. When a spin-$\frac{1}{2}$ hyperon decays nonleptonically, the daughter baryon is also a spin-$\frac{1}{2}$ particle while the daughter meson has spin zero. Because of the complications of the strong interaction, one needs an effective weak Hamiltonian to describe these decays. This Hamiltonian, because of angular momentum conservation, is restricted to having only $l = 0$ (s-wave) and $l = 1$ (p-wave) components. In order to satisfy Lorentz invariance, the matrix element must be a sum of scalar and pseudoscalar quantities. With this in mind, the weak Hamiltonian matrix element for these decays can be written [1]:

$$m = \langle B_j\pi \mid H_w \mid B_i\rangle = \overline{u}(A + B\gamma_5)u \tag{1.1}$$

where A and B are the s-wave and the p-wave amplitudes respectively. Note that the final state pion is a pseudoscalar and has negative parity. The term $\overline{u}B\gamma_5 u$ is also a pseudoscalar and so B is called the parity conserving amplitude. The term $\overline{u}Au$ is a scalar and has positive parity. Since this term has the opposite parity of the pion, A is called the parity violating amplitude.

A more physically meaningful quantity than B is $\overline{B} = ((E_j - m_j)/(E_j + m_j))B$, where E_j is the daughter baryon energy and m_j is its mass in the parent particle's rest frame. The amplitude $\overline{B}$ appears in an analogous manner to A in the formulas for the decay rate and asymmetries, and is thus more easily extracted from these measurable quantities than B. Using these definitions and the weak Hamiltonian matrix element the decay rate becomes:

$$\Gamma = \frac{1}{4\pi} \mid q \mid (\mid A \mid^2 + \mid \overline{B} \mid^2)\frac{(E_j + m_j)}{M_i} \tag{1.2}$$

where M_i is the parent baryon mass and $\mid q \mid$ is the decay momentum. The decay rate can also be written as $\Gamma = \hbar(BR)/\tau$, where (BR) is the branching ratio for the decay in question and τ is the lifetime of the parent baryon.

A similar analysis can be used for the decay $\Omega^- \rightarrow \Lambda K^-$. Now a spin-$\frac{3}{2}$ baryon decays into a spin-$\frac{1}{2}$ baryon and a spin-0 meson. In this case the weak Hamiltonian matrix element is [1]:

$$m = \langle \Lambda K^- \mid H_w \mid \Omega^- \rangle = \frac{q^\mu}{m_\pi}\overline{u}(B + C\gamma_5)u_\mu \tag{1.3}$$

where B and C are the p-wave and d-wave ($l = 2$) amplitudes, and u_μ is a Rarita-Schwinger vector-spinor. In this case B is the parity conserving amplitude and C is the parity violating amplitude. Also note that C is kinematically suppressed by a factor of $(M_{\Xi^0} - M_\Lambda)/(M_{\Xi^0} + M_\Lambda)$ with respect to B [2]. This suppression factor has a value of approximately 0.08. Once again the higher angular momentum term has the more meaningful expression $\overline{C} = ((E_\Lambda - m_\Lambda)/(E_\Lambda + m_\Lambda))C$. Using the above weak Hamiltonian matrix element the decay rate becomes [1]:

$$\Gamma = \frac{1}{4\pi}\frac{|q|^3}{3m_\pi^2}(|B|^2 + |\overline{C}|^2)\frac{(E_\Lambda + m_\Lambda)}{M_{\Omega^-}} \tag{1.4}$$

1.2.1 Decay Asymmetries for Spin-$\frac{1}{2}$ Baryons

Before preceding to a description of the spin-$\frac{3}{2}$ amplitudes, it is useful to consider the principles with the spin-$\frac{1}{2}$ decay amplitudes. In fact a comparison between these two cases provides valuable insight into the harder to understand spin-$\frac{3}{2}$ decay. In the spin-$\frac{1}{2}$ decay, and in the spin-$\frac{3}{2}$ as will be seen later, there are several other useful relations involving the decay amplitudes.

Other useful relations involving A and B amplitudes are the decay asymmetries proposed by Lee and Yang [3]:

$$\alpha = \frac{2Re(A^*\overline{B})}{(|A|^2 + |\overline{B}|^2)}, \quad \beta = \frac{2Im(A^*\overline{B})}{(|A|^2 + |\overline{B}|^2)}, \quad \gamma = \frac{|A|^2 - |\overline{B}|^2}{(|A|^2 + |\overline{B}|^2)} \tag{1.5}$$

and the normalization condition $\alpha^2 + \beta^2 + \gamma^2 = 1$. These decay asymmetries describe the angular distribution of the daughter baryon and its polarization. The angular distribution of the daughter baryon in the rest frame of the parent hyperon can be written as:

$$I(\theta_n, \phi_n) = \frac{1}{4\pi}(1 + \alpha_{B_i}\vec{P_{B_i}} \cdot \hat{n}) \tag{1.6}$$

with $\vec{P_{B_i}}$ being the polarization of the decaying baryon and $\hat{n}$ the momentum direction of the daughter baryon in the rest frame of the parent baryon. The polarization of the daughter baryon in its own rest frame is:

$$\vec{P}_\Lambda = \frac{1}{1 + \alpha_\Xi \vec{P}_\Xi \cdot \hat{\Lambda}}[(\alpha_\Xi + \vec{P}_\Xi \cdot \hat{\Lambda})\hat{\Lambda} + \beta_\Xi(\vec{P}_\Xi \times \hat{\Lambda}) + \gamma_\Xi[\hat{\Lambda} \times (\vec{P}_\Xi \times \hat{\Lambda})]]. \tag{1.7}$$

where the subscripts for the decay $\Xi^- \rightarrow \Lambda\pi^-$ were used for clarity. Note that a 3 vector polarization is only well defined in the rest frame of the polarized particle [4], and so the polarization terms on the left hand side of equation 1.7 are measured in the Λ rest frame, while those on the right hand side are measured in the Ξ^- rest frame. For most purposes time reversal invariance can be assumed and the situation becomes less complex. In this case, the A and B amplitudes are real up to an overall phase factor if final state interactions are neglected. Because A and B are relatively real, $\beta = 0$ and $\alpha = 2A\overline{B}/(|A|^2 + |\overline{B}|^2)$. Now except for an overall phase factor, measurements of (BR), τ and α for nonleptonic hyperon decays are sufficient for determining A and B. Final state interactions can give a small nonzero value to β [5].

The decay asymmetry parameters α, β, and γ describe both the daughter baryon polarization and its angular distribution in the rest frame of the parent hyperon. While the following discussion will focus on the decay sequence $\Xi^- \rightarrow \Lambda\pi$ followed by $\Lambda \rightarrow p\pi^-$, the equations involved can be easily converted for other nonleptonic weak hyperon decays. In order to convert the equations to another decay sequence, all that need be done is replace all occurrences of the subscript Ξ^- by the new parent hyperon, and all occurrences of the subscript Λ by the new daughter baryon.

First consider the decay $\Xi^- \rightarrow \Lambda\pi$. From section 1.2 the angular distribution can be written in terms of the decay asymmetry α_{Ξ^-} and the polarization P_{Ξ^-} as:

$$I(\theta_\Lambda, \phi_\Lambda) = \frac{1}{4\pi}(1 + \alpha_{\Xi^-}\vec{P}_{\Xi^-} \cdot \hat{\Lambda}) \tag{1.8}$$

where θ_Λ and ϕ_Λ are the spherical angles describing the momentum direction of Λ ($\hat{\Lambda}$) with respect to $\vec{P}_{\Xi^-}$. The angular distribution can be expanded in terms of an arbitrary axis $\hat{n}$. Consider a spherical coordinate system about the axis $\hat{n}$. The angular distribution then can be rewritten in this system as:

$$I(\theta_n, \phi_n) = \frac{1}{4\pi}(1 + \alpha_{\Xi^-} \vec{P}_{\Xi^-} \cdot \hat{n}\hat{n} \cdot \hat{\Lambda}) \tag{1.9}$$

where θ_n and ϕ_n are the usual spherical angles describing the direction of $\hat{\Lambda}$ with respect to the axis $\hat{n}$ (see Figure 1.3). In the above equation, $\cos\theta_n = \hat{n} \cdot \hat{\Lambda}$. Also, the equation is independent of ϕ_n, so by substituting in $\cos\theta_n$ and integrating over ϕ_n, the angular distribution reduces to:

$$I(\theta_n) = \frac{1}{2}(1 + \alpha_{\Xi^-} \vec{P}_{\Xi^-} \cdot \hat{n} \cos\theta_n) \tag{1.10}$$

Now consider the angular distribution of the proton from the decay of the daughter Λ. The distribution can then be projected onto the 3 helicity frame axes

$$\hat{\Lambda}, \quad \hat{Y} = \frac{\hat{P}_{\Xi^-} \times \hat{\Lambda}}{|\hat{P}_{\Xi^-} \times \hat{\Lambda}|}, \quad \hat{X} = \frac{\hat{Y} \times \hat{\Lambda}}{|\hat{Y} \times \hat{\Lambda}|}. \tag{1.11}$$

This distribution can be integrated over the appropriate ϕ angle for each of the helicity frame axes. Finally, after integrating over $\cos\theta_i$ and ϕ_i, the spherical angles describing the Λ direction in the Ξ^- rest frame about an arbitrary axis, the angular distribution projections become [6]:

$$\begin{aligned}
I(\hat{\Lambda} \cdot \hat{p}) &= \frac{1}{2}(1 + \alpha_\Lambda \alpha_\Xi \hat{\Lambda} \cdot \hat{p}) && (1.12)\\
I(\hat{X} \cdot \hat{p}) &= \frac{1}{2}(1 - \frac{\pi}{4}\alpha_\Lambda P_\Xi \gamma_\Xi \hat{X} \cdot \hat{p}) && (1.13)\\
I(\hat{Y} \cdot \hat{p}) &= \frac{1}{2}(1 + \frac{\pi}{4}\alpha_\Lambda P_\Xi \beta_\Xi \hat{Y} \cdot \hat{p}) && (1.14)
\end{aligned}$$

The first projection can be used to measure α_{Ξ^-}. The second two provide measurements of β_{Ξ^-} and γ_{Ξ^-} if the cascade sample is polarized ($P_{\Xi^-} \neq 0$). Notice that in the ratio of the slopes for the $\hat{X}$ and $\hat{Y}$ projections only the terms β_{Ξ^-} and γ_{Ξ^-} do not cancel out. Therefore, the ratio of $\beta_{\Xi^-}/\gamma_{\Xi^-}$ only requires that $P_{\Xi^-} \neq 0$.

1.2.2 Decay Asymmetries for the $\Omega^- \rightarrow \Lambda K^-$ Decay

The decay asymmetries for the decay $\Omega^- \rightarrow \Lambda K^-$ have the same basic form and normalization condition as in the case of spin-$\frac{1}{2}$ baryon decay. In this case, the decay asymmetries are defined in terms of the B and C amplitudes as:

$$\alpha_{\Omega^-} = \frac{2Re(B^*\overline{C})}{(|B|^2 + |\overline{C}|^2)}, \quad \beta_{\Omega^-} = \frac{2Im(B^*\overline{C})}{(|B|^2 + |\overline{C}|^2)}, \quad \gamma_{\Omega^-} = \frac{|B|^2 - |\overline{C}|^2}{(|B|^2 + |\overline{C}|^2)} \tag{1.15}$$

As mentioned earlier, C is kinematically suppressed and so the expected values are $\alpha_{\Omega^-} = 0$, $\beta_{\Omega^-} = 0$, and $\gamma_{\Omega^-} = 1$. In this case measurements of (BR), τ and α for $\Omega^- \rightarrow \Lambda K^-$ are sufficient for determining the magnitudes of B and C. Therefore measurements must be of sufficient precession to test beyond this kinematic suppression.

The polarization of the daughter Λ from this decay is [7, 8, 9]:

$$\vec{P}_\Lambda = \frac{1}{2(J+1)}[1 + (2J+1)\gamma_{\Omega^-}]\vec{P}_{\Omega^-} \tag{1.16}$$

where J is the spin of the Ω^-. This formula was derived by integrating the angular distribution over the spherical angles describing the Λ direction in the Ω^- rest frame about an arbitrary axis.

The angular distribution projections can be found by doing the same integrations as was done in the spin-$\frac{1}{2}$ case. Assuming that the Ω^- has a spin of $J = \frac{3}{2}$ [10, 11], the angular distribution projections onto the helicity frame axes are (see appendix A):

$$\begin{aligned}
I(\hat{\Lambda} \cdot \hat{p}) &= \frac{1}{2}(1 + \alpha_\Lambda \alpha_\Omega \hat{\Lambda} \cdot \hat{p}) && (1.17)\\
I(\hat{X} \cdot \hat{p}) &= \frac{1}{2}[1 - \frac{3\pi}{10}\alpha_\Lambda \gamma_\Omega \hat{X} \cdot \hat{p}(P_\Omega - \frac{5}{16}\sqrt{\frac{7}{5}}t_{30})] && (1.18)\\
I(\hat{Y} \cdot \hat{p}) &= \frac{1}{2}[1 + \frac{3\pi}{10}\alpha_\Lambda \beta_\Omega \hat{Y} \cdot \hat{p}(P_\Omega - \frac{5}{16}\sqrt{\frac{7}{5}}t_{30})] && (1.19)
\end{aligned}$$

The projection onto the $\hat{\Lambda}$ axis is completely analogous to the spin-$\frac{1}{2}$ case. The $\hat{X}$ and $\hat{Y}$ projections are complicated by the tensor polarization term t_{30}. Fortunately, if the quantity $(P_\Omega - \frac{5}{16}\sqrt{\frac{7}{5}}t_{30})$ is nonzero, then the ratio $\beta_{\Omega^-}/\gamma_{\Omega^-}$ can still be measured. In this case, the measurement will be independent of P_{Ω^-} and t_{30}.

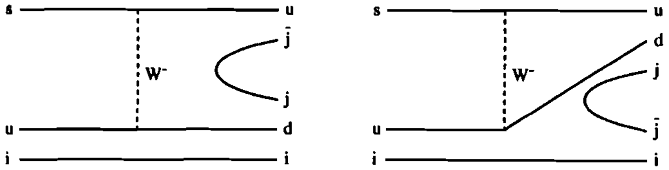

Annihilation Diagram Annihilation Diagram

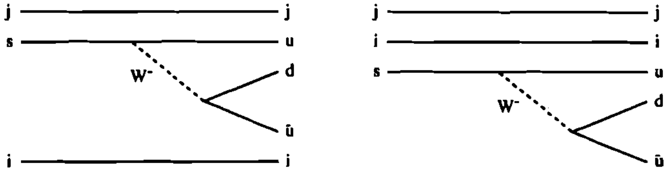

Quark Decay Diagram Quark Decay Diagram

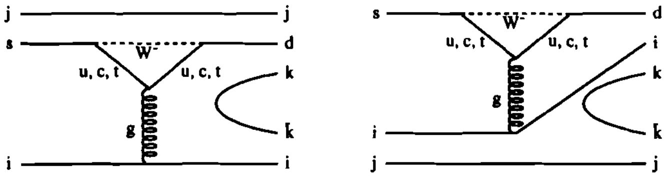

Penguin Diagram Penguin Diagram

Figure 1.1: Feynman diagrams for quark annihilation, quark decay and penguins for nonleptonic weak decays of the spin-$\frac{1}{2}$ hyperons. The symbols i, j and k stand for u, d or s quarks.

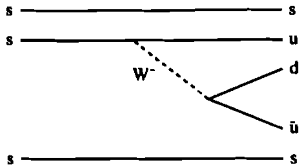

Quark Decay Diagram

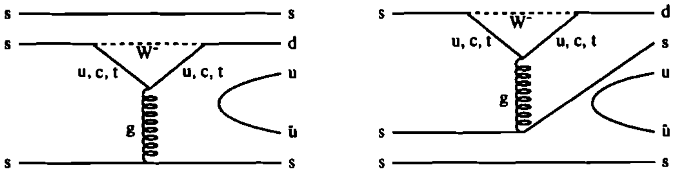

Penguin Diagram Penguin Diagram

Figure 1.2: Feynman diagrams for quark decay and penguins for the nonleptonic weak decay $\Omega^- \to \Lambda K^-$.

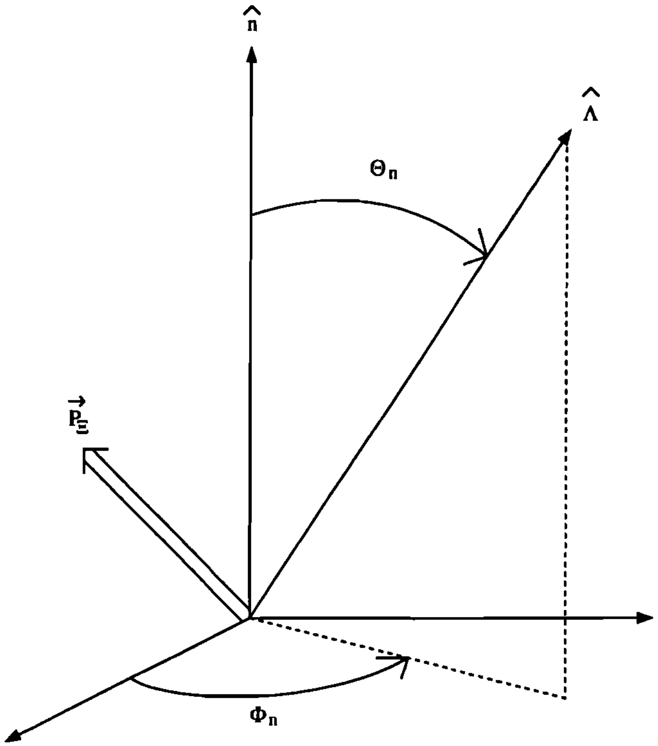

Figure 1.3: Spherical coordinate system in the Ξ^- rest frame.

1.3 Experimental Status of the Decay Asymmetries

The present world averages for the measurements of the decay asymmetries are given in Table 1.1 [12]. The usual way of reporting the ratio of β/γ is in terms of the angle ϕ:

$$\phi = \tan^{-1}\left(\frac{\beta}{\gamma}\right) \qquad (1.20)$$

For both the decays $\Lambda \to n\pi^0$ and $\Omega^- \to \Lambda K^-$ no previous measurement has been made of the β/γ angle ϕ. Although ϕ_{Ω^-} is expected to be small or zero, it is still important to check this experimentally. α_{Ω^-} has been measured before and shown to be consistent with zero, as expected [7, 13]. Using the world average values for the lifetime, branching ratio and alpha asymmetry parameter listed in Table 1.1, the magnitudes of the B and C amplitudes for the decay $\Omega^- \to \Lambda K^-$ can be calculated. Table 1.2 shows the magnitudes of the B and C amplitudes based on these measurements. Two of the theoretical predictions for the magnitude of the B amplitude are 4.73×10^{-7} [14] and 7.70×10^{-7} [15], neither of which show very good agreement with experimental results. The prediction for the C amplitude is zero, which agrees well with experiment. The ratio of the C amplitude to the B amplitude is 0.14 ± 0.14, which is in good agreement with the kinematic suppression factor of 0.08. Still, an improvement of the α_{Ω^-} measurement should provide a better limit on the suppression of the d-wave in this decay process. Also, the world average for α_{Ω^-} is based on two previous measurements neither of which were high statistics measurements (1743 events and 12,000 events). Having low statistics in these types of measurements makes it hard to control the systematics. All of the events go into making the minimal measurement and thus precluding a strong study of the signal for systematic effects. Therefore, a sample of several hundred thousand of these events would greatly improve the understanding of this measurement.

The A and B amplitudes from the spin-$\frac{1}{2}$ hyperon decays are listed in Table 1.3 for comparison, and were calculated using the world average lifetime, branching ratio, and alpha asymmetry parameter listed in Table 1.1 for the various modes. In both cases the amplitudes are on the order of 10^{-7}.

Decay	α asymmetry	lifetime (10^{-10})	branching ratio	ϕ
$\Lambda \to n\pi^0$	0.638 ± 0.066	2.624 ± 0.008	0.3581 ± 0.0049	none
$\Lambda \to p\pi^-$	0.642 ± 0.013	2.624 ± 0.008	0.6419 ± 0.0049	-6.5° ± 3.5°
$\Sigma^+ \to n\pi^+$	0.068 ± 0.013	0.7997 ± 0.0036	0.4836 ± 0.0030	167.° ± 20.°
$\Sigma^+ \to p\pi^0$	-0.980 ± 0.015	0.7997 ± 0.0036	0.5164 ± 0.0030	36.° ± 34.°
$\Sigma^- \to n\pi^-$	-0.0681 ± 0.0077	1.482 ± 0.011	> 0.99	10.° ± 15.°
$\Xi^0 \to \Lambda\pi^0$	-0.399 ± 0.015	2.97 ± 0.04	> 0.99	21.° ± 12.°
$\Xi^- \to \Lambda\pi^-$	-0.455 ± 0.015	1.642 ± 0.015	> 0.99	4.° ± 4.°
$\Omega^- \to \Lambda K^-$	-0.026 ± 0.026	0.822 ± 0.012	0.678 ± 0.007	none

Table 1.1: Measured hyperon decay asymmetry parameters.

Decay	B (10^{-7})	C (10^{-7})
$\Omega^- \to \Lambda K^-$	5.60 ± 0.05	0.78 ± 0.78

Table 1.2: The parity conserving and parity violating amplitudes, B and C respectively, from experimental results.

Decay	A (10^{-7})	B (10^{-7})
$\Lambda \to n\pi^0$	-2.39 ± 0.04	-15.61 ± 1.26
$\Lambda \to p\pi^-$	3.25 ± 0.02	22.11 ± 0.52
$\Sigma^+ \to n\pi^+$	0.14 ± 0.03	42.19 ± 0.16
$\Sigma^+ \to p\pi^0$	-3.26 ± 0.10	26.73 ± 1.24
$\Sigma^- \to n\pi^-$	4.26 ± 0.02	-1.43 ± 0.16
$\Xi^0 \to \Lambda\pi^0$	3.40 ± 0.02	-11.72 ± 0.47
$\Xi^- \to \Lambda\pi^-$	-4.49 ± 0.02	17.41 ± 0.61

Table 1.3: The parity violating and parity conserving amplitudes, A and B respectively, from experimental results.

Chapter 2

The Apparatus

2.1 Introduction

In order to make a measurement of the Ω^- decay asymmetry, a large sample of Ω^-s were required. In addition to the Ω^-s, a much larger sample of Ξ^-s were collected simultaneously. Collecting data under different target and beam conditions allowed for greatly improved background and systematic studies. The various samples of Ω^-s and Ξ^-s were produced by using a high energy proton beam and a series of two target and magnet stations. By varying the fields in the two magnets and removing the first target, the production of Ω^- and Ξ^- particles under several different conditions was possible.

The usual decay mode for the Ω^- particle (occurring 67.8% of the time) is $\Omega^- \rightarrow \Lambda K^-$, while for Ξ^-s the primary decay mode is $\Xi^- \rightarrow \Lambda\pi^-$ (occurring over 99% of the time). The subsequent decay of the Λ into a proton and π^- occurs 64.1% of the time. In both cases, there are two negatively charged daughter mesons and one daughter proton after the primary and the Λ decay. Table 2.1 gives the typical decay distances for the Ω^-, Ξ^-, and Λ hyperons in this experiment. Measurements of the positions and the momenta of the proton and two mesons were made with a magnetic spectrometer. A signal developed by the presence of at least two oppositely charged tracks indicated a possible decay event in the spectrometer. This signal triggered the data acquisition system which read out the detector information and wrote it to buffered memory. The buffered memory was read out by a computer between proton spills and the information was written to magnetic tape for future analysis.

Particle	From	Average Momentum (Gev/c)	γ	$\gamma c\tau$ (cm)
Ξ^-	target	396.	300.	1473.
Ω^-	target	394.	236.	580.
Λ	$\Xi^- \rightarrow \Lambda\pi^-$	334.	299.	2359.
Λ	$\Omega^- \rightarrow \Lambda K^-$	262.	235.	1854.

Table 2.1: The relativistic parameter γ and the lifetime $\gamma c\tau$ for Λ, Ξ^- and Ω^- based on their average momentum in this experiment.

2.2 The Proton Beam

The Fermi National Accelerator Laboratory (Fermilab) has been the site of numerous fixed target experiments as well as several collider experiments. One of these fixed target experiments, E800, which operated during the 1991 and 1992 fixed target run, collected the data used in this dissertation. The accelerator provided 800 GeV protons, at an intensity of over 1.2×10^{13} protons per 23 second period (or spill), which was divided among the various beamlines and subsequently among the fixed target experiments. The duty cycle of the accelerator was 60 seconds.

E800 was located at the end of the Proton Center beamline and required intensities which varied from 5.0×10^{10} to 2.0×10^{12} protons per spill, depending on the mode of operation. The Proton Center beamline provided several functions beyond simple beam transport. First the beam was required to be 2 mm or less in diameter when it hit the target, and thus had to be focused as it was being transported. The focusing was accomplished by a series of quadrapole magnets. Since quadrapole magnets focus in one plane and defocus in the plane perpendicular to the first, the quadrapole magnets' polarity had to be alternated so that the overall effect was focusing in both the vertical and the horizontal planes. Another task required of the beamline was the ability to steer the beam off the centerline so that it could be brought to the targets at various angles in the vertical plane. The three typical angles used in this experiment were ±1.8 mrad and 0 mrad.

To accomplish the nonzero angles, the beam was bent using two dipole magnets. First the beam was bent away from the vertical zero line by a magnet called PC3V1 (see Figure 2.1). Next the beam was bent back toward the vertical zero line, by a magnet called PC3V2, so that it would cross the centerline at the desired target (either the upstream target or the downstream target depending on the mode of operation). The position of the beam along the beamline was monitored by a series of segmented wire ion chambers (SWICs) placed at various locations along the beamline. Three of these SWICs (PC3WC2, PC3WC3 and PC3WC4) were used to monitor the angle of the beam as it approached the targets. PC3WC2 was placed between magnets PC3V1 and PC3V2. PC3WC3 was place in front of the upstream target and PC3WC4 was placed in front of the downstream target. All three of these SWICs had a 0.5 mm wire spacing.

Another device used to monitor the proton beam was a secondary emission monitor (SEM). The SEM provided a means of monitoring the intensity of the proton beam in the Proton Center beamline. By using the SEM and the SWICs together the experiment was able to monitor the quality of the proton beam as it approached the target on a spill by spill basis.

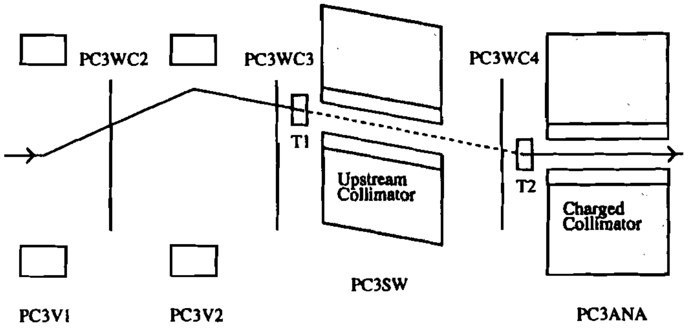

Figure 2.1: Illustration of the section of beamline used to develop the different targeting angles. T1 and T2 are the upstream and downstream targets respectively.

2.3 Collimators and Targeting

Background and systematic studies were an important part of the asymmetry measurements, and were greatly enhanced by the use of data samples from several different target and beam conditions. Polarization can effect the asymmetry measurements and is not expected to be the same under all production conditions (see for example references [8, 16, 17, 18]). E800 was designed to be able to switch between a secondary and a tertiary beam experiment, and so required two collimators and two targets. In the tertiary mode the upstream collimator served as a proton dump and a neutral beam selector and was referred to as the neutral collimator. In this mode the downstream collimator, called the charged collimator, was used to select a negative beam and as a neutral beam dump. To operate in the tertiary mode both targets had to be used and both collimators were in regions of high magnetic field. In the secondary beam mode, the idea was to bring the proton beam though the upstream collimator unchanged. To accomplish this, the defining aperture of the upstream collimator had to be wider than the proton beam. In this mode, the charged collimator would act as a proton beam dump and a negative beam selector. Since the proton beam would be passing though the upstream collimator, only the downstream target was needed and the upstream collimator was in a field free region.

The proton production scheme was the only secondary beam mode used. In Figure 2.2a the secondary beam was produced by protons incident on the downstream target at nonzero angle. Note that the production angle is defined as the angle between the incoming and outgoing particle momenta.

On the other hand, there were two modes of neutral beam production both of which were tertiary beam modes. In Spin Transfer Production, Figure 2.2b, protons hit the upstream target at a nonzero angle and the resulting polarized neutral beam was directed at the downstream target at 0 mrad thus producing the charged tertiary beam. For the Neutral Production mode, depicted in Figure 2.2c, protons hit the upstream target at 0 mrad producing an unpolarized neutral beam which then hit the downstream target at a nonzero angle to produce a charged tertiary beam.

Note that since the incident angle was also in the bend plane of the upstream magnet, the field of the magnet had to be reversed when the beam angle was reversed in order to insure that the proton beam dumped outside of the defining aperture and not too close to the vertical zero line. For Spin Transfer the field in the upstream collimator bent positive particles down when the targeting angle was negative, and up when the targeting angle was positive. By configuring the magnet this way for Spin Transfer, the proton beam was dumped well outside the defining aperture of the upstream collimator. For Neutral Production, the field direction was chosen at each angle so that the opposite situation occurred to keep the proton beam from dumping close to the vertical zero line of the charged collimator.

2.3.1 The Targets

The two targets used in the experiment were made of Beryllium to maximize the fraction of high momentum baryons produced. Both targets were approximately 0.37 interaction lengths long. The upstream target was 150.72 mm long, while the downstream target was 149.70 mm long. The center of the upstream target was 12.1 cm in front of the upstream end of the upstream collimator. This target was cylindrical in shape with a diameter of 6.55 mm. The downstream target, unlike the upstream target, was rectangular in shape with its center located 13.2 cm in front of the upstream end of the charged collimator and 62.2 cm downstream of the upstream collimator. The width of this target was 5.15 mm, while its height was 5.28 mm.

2.3.2 The Upstream Collimator

The upstream collimator, Figure 2.3 and Table 2.2, fit inside a standard Fermilab B2 dipole magnet. The field of the B2 magnet was 1.8 T and its length was 607.0 cm. A vacuum pipe 640.0 cm in length was mounted through the center of the B2 magnet, extending 16.5 cm beyond the magnet on either side. The collimator was placed inside the vacuum pipe and was made from brass and tungsten segments. The tungsten segments were placed where the proton beam was expected to dump when the incident angle was between 0. and 2. mrad. The defining aperture was 0.254 cm by 0.254 cm and had a length of 91.44 cm. It began at a z position of 396.24 cm downstream from the upstream end of the magnet. Thus, the solid angle of the upstream collimator was approximately 0.41 microsteradian.

The B2 magnet which contained the upstream collimator was mounted on two stepper motors which allowed remote vertical positioning of the magnet and thus the upstream collimator. One stepper motor was placed 55.1 cm from the upstream edge of the magnet, the other motor was placed 51.4 cm from the downstream edge thus giving

	Plan View			Elevation View		
Z (cm)	Max (cm)	Min (cm)	Width (cm)	Max (cm)	Min (cm)	Width (cm)
0.00	1.206	-1.206	2.413	1.524	-1.524	3.048
76.20	1.206	-1.206	2.413	1.524	-1.524	3.048
76.20	1.206	-1.206	2.413	1.206	-1.206	2.413
228.60	1.206	-1.206	2.413	1.206	-1.206	2.413
228.60	1.206	-1.206	2.413	1.524	-1.524	3.048
411.48	1.206	-1.206	2.413	1.524	-1.524	3.048
411.48	0.135	-0.135	0.269	0.135	-0.135	0.269
502.92	0.135	-0.135	0.269	0.135	-0.135	0.269
502.92	0.356	-0.356	0.711	0.356	-0.356	0.711
594.36	0.356	-0.356	0.711	0.356	-0.356	0.711
594.36	0.406	-0.406	0.813	0.406	-0.406	0.813
640.00	0.406	-0.406	0.813	0.406	-0.406	0.813

Placement of tungsten						
	Plan View			Elevation View		
	Z min (cm)	Z max (cm)	Length (cm)	Z min (cm)	Z max (cm)	Length (cm)
	350.52	502.92	152.40	411.48	502.92	91.44

Table 2.2: The E800 upstream collimator aperture values.

a 500.4 cm separation between the two pivot points. Whenever an angle change at the downstream target was needed, as in an angle change in the Neutral Production mode, the stepper motors were used to reposition the magnet and thus the upstream collimator. This process of vertically changing the position of the magnet typically took 20 minutes. Because the stepper motors had 74,676 counts per cm and 87,630 counts per cm for the upstream and downstream motors respectively, the vertical position of the upstream collimator could be precisely determined each time the magnet was moved. The ability to precisely determine the vertical position of the upstream collimator also enabled the experimenters to reproduce a desired collimator position as needed to better than 0.01 cm.

2.3.3 The Charged Collimator

The charged collimator, Figure 2.4 and Table 2.3, was designed to fit inside the Proton Center Hyperon Magnet. The central orbit momentum was designed to be 400 GeV at a B-field of 3.35 T, which corresponded to a central orbit radius of 39828.55 cm. The bend angle for this central orbit through the hyperon magnet was 18.37 mrad. Most data was taken at a field of 3.33 T and a smaller sample at 2.39 T corresponding to a magnet current of 2900 amps and 750 amps respectively. The collimator itself fit into the aperture of a holder which in turn fit inside the Hyperon Magnet. The gap in which the collimator fit was 7.72 cm (x view) by 2.29 cm (y view) and had a length of 731.52 cm. The collimator holder was composed of three sections, the upstream section was 335.28 cm long and the two downstream sections were 198.12 cm long. The defining channel had an upstream aperture of 0.508 cm by 0.508 cm located 274.32 cm from the upstream end of the magnet. The exit point of the defining channel was at 457.20 cm where the aperture was 0.762 cm by 0.762 cm. The solid angle entering the defining channel was 3.43 microsteradian.

A plot of field versus current for the hyperon magnet is shown in Figure 2.5. This plot clearly shows that at 2900 amps, current used in the dominant mode for data taking, the hyperon magnet is in the saturation region. In Figure 2.6 plots of the overall collimator acceptance and the channel acceptance as a function of momentum are shown. The overall collimator acceptance is defined as the number of charged particles exiting the downstream end of the collimator divided by the number of charged particles produced in the target. A plot of the overall collimator acceptance is useful in the design stage of the experiment, especially during the design of the collimator itself. The channel acceptance is defined as the number of charged particles exiting the downstream end of the collimator divided by the number of charged particles entering the defining channel. The channel acceptance demonstrates the efficiency of the collimator in transporting

	Plan View			Elevation View		
Z (cm)	Max (cm)	Min (cm)	Width (cm)	Max (cm)	Min (cm)	Width (cm)
0.00	1.267	-1.273	2.540	1.143	1.143	2.286
30.48	1.532	-1.008	2.540	1.143	-1.143	2.286
60.96	1.770	-0.770	2.540	1.143	-1.143	2.286
91.44	1.986	-0.554	2.540	1.143	-1.143	2.286
121.92	2.179	-0.361	2.540	1.143	-1.143	2.286
152.40	2.349	-0.191	2.540	1.143	-1.143	2.286
182.88	2.494	-0.046	2.540	1.143	-1.143	2.286
213.36	2.616	0.076	2.540	1.143	-1.143	2.286
243.84	2.715	0.175	2.540	1.143	-1.143	2.286
243.84	2.461	0.429	2.032	1.143	-1.143	2.286
274.32	2.540	0.508	2.032	1.143	-1.143	2.286
274.32	1.778	1.270	0.508	0.254	-0.254	0.508
304.80	1.829	1.321	0.508	0.254	-0.254	0.508
304.80	1.956	1.194	0.762	0.381	-0.381	0.762
335.28	1.986	1.224	0.762	0.381	-0.381	0.762
365.76	1.991	1.229	0.762	0.381	-0.381	0.762
396.24	1.976	1.214	0.762	0.381	-0.381	0.762
426.72	1.933	1.171	0.762	0.381	-0.381	0.762
457.20	1.872	1.110	0.762	0.381	-0.381	0.762
457.20	2.507	0.475	2.032	0.508	-0.508	1.016
487.68	2.418	0.386	2.032	0.508	-0.508	1.016
518.16	2.309	0.277	2.032	0.508	-0.508	1.016
548.64	2.174	0.142	2.032	0.508	-0.508	1.016
579.12	2.017	-0.015	2.032	0.508	-0.508	1.016
609.60	1.836	-0.196	2.032	0.508	-0.508	1.016
609.60	1.455	0.185	1.270	0.635	-0.635	1.270
640.08	1.252	-0.018	1.270	0.635	-0.635	1.270
670.56	1.024	-0.246	1.270	0.635	-0.635	1.270
701.04	0.775	-0.495	1.270	0.635	-0.635	1.270
731.52	0.500	-0.770	1.270	0.635	-0.635	1.270

Table 2.3: The E800 charged collimator aperture values.

the charged beam after exclusion of neutral particles or oppositely charged particles (positively charged particles for a negatively charge beam). The channel acceptance is more important than the overall collimator acceptance for studying the charged beam acceptance of the spectrometer. The difference between the overall collimator acceptance and the channel acceptance is the loss from producing a clean charged beam.

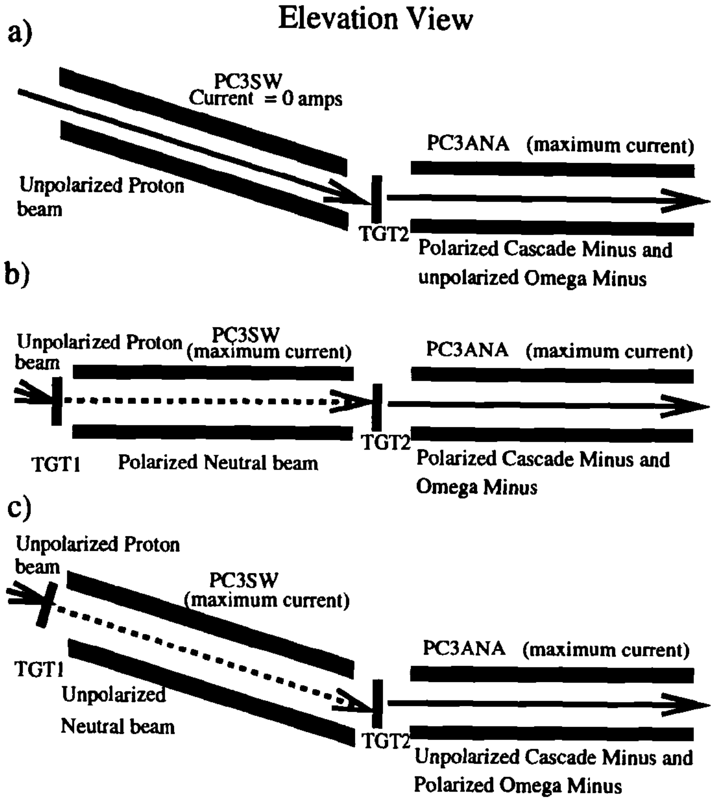

Figure 2.2: Production Modes.

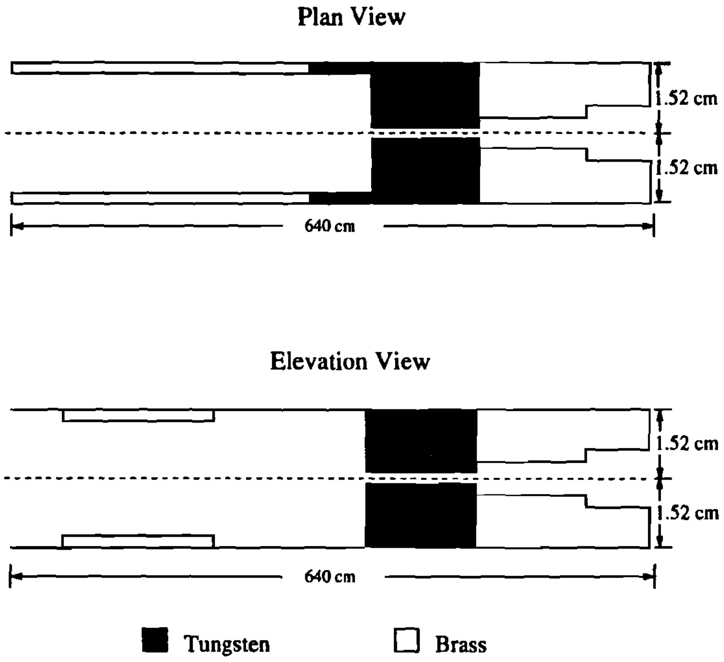

Figure 2.3: The E800 Upstream Collimator.

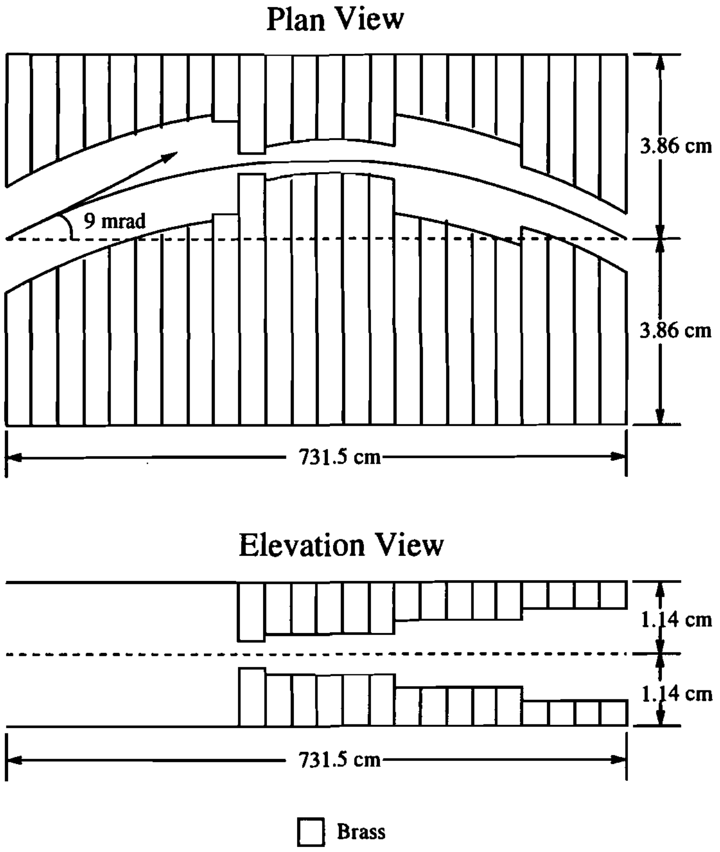

Figure 2.4: The E800 Charged Collimator. The arrow indicates the direction of the incident beam.

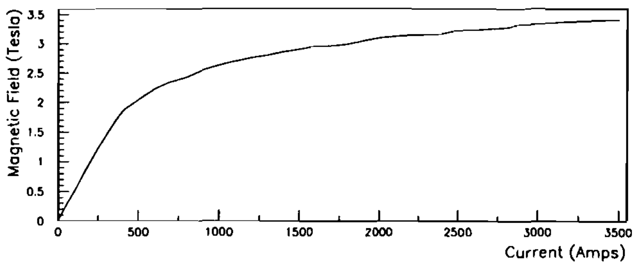

Figure 2.5: Field versus current for the hyperon magnet.

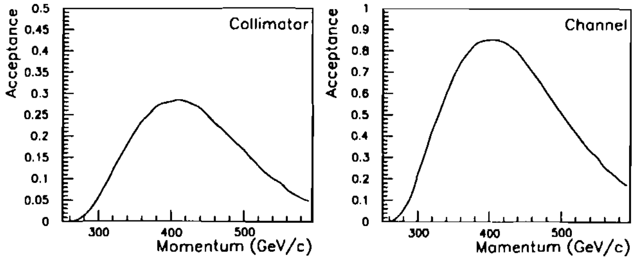

Figure 2.6: The overall collimator acceptance and the channel acceptance, left and right respectively, for the charge collimator.

2.4 The Charged Particle Spectrometer

2.4.1 The Design

The charged particle spectrometer can be described in terms of a right-handed coordinate system with the origin placed at the exit of the charged collimator. The z-axis is defined as the direction of the tangent line to the central orbit of the charged collimator at this origin, and pointing downstream. The y-axis pointed up and the x-axis was just the cross-product of the y-axis into the z-axis. The spectrometer was designed to measure the momentum vectors of the charged particles in the decay sequence of $\Omega^- \rightarrow \Lambda + K^-$, $\Lambda \rightarrow p + \pi^-$. The design also worked well for the very similar decay chain $\Xi^- \rightarrow \Lambda + \pi^-$, $\Lambda \rightarrow p + \pi^-$. This spectrometer consisted of 12 MWPCs (multi wire proportional chambers), 8 SSD planes (silicon strip detectors), 4 scintillation counters and 2 analysis magnets (see Table 2.4 and Figure 2.7). The analysis magnets (dipole magnets with their fields parallel to the vertical axis) were used to measure the momenta of the two daughter mesons and the proton. In order to reduce the multiple scattering in the air, tubes and bags filled with Helium were placed between the detectors and inside the magnet apertures.

The acceptance of the spectrometer can be defined as the number of events which satisfy the trigger divided by the number of charged particles exiting the downstream end of the charged collimator for a given decay sequence (for example $\Omega^- \rightarrow \Lambda + K^-$, $\Lambda \rightarrow p + \pi^-$). The combined spectrometer and channel acceptance is the product of the spectrometer acceptance and the channel acceptance (see section 2.3.3). The combined acceptance demonstrates the efficiency for detecting the desired topology for particles in the charged beam. Both the spectrometer acceptance and the combined spectrometer and channel acceptance as a function of momentum are shown in Figure 2.8. A comparison of the two plots shows that the channel acceptance is well matched to the spectrometer acceptance. Note that bumps on the tails of these plots are due to small statistics.

2.4.2 The Silicon Strip Detectors

After exiting the charged collimator, a particle enters the spectrometer. The first part of the spectrometer encountered was a set of eight SSD planes. The planes were grouped in pairs, the first of a pair being able to detect the particle's position in x and the second doing the same for the particle's position in y. There were four sets of these x and y planes. The planes were built by Hamamatsu and had 280 strips of 100 μm pitch and were 300μm thick. The signals were amplified first by a pre-amplifier [19] mounted close to the signal plane, and later by an amplifier which routed the signal to a latch. Because the signals from the amplifiers had to arrive in coincidence with the trigger which was formed in the electronics trailer, these signals had to be delayed otherwise they would arrive too far ahead of the trigger. This delay was achieved through the combination of long cables and adjustable electronic delays within the latches. The added delay did not affect the deadtime. The front end electronics were built by Laben and the amplifiers and latches by Nanometric Systems, Inc. Multiple crates of latches could be read by one CAMAC interface module (N-281). The Nanometric interface module provided the interface between the data aquisition system and the front end SSD latches.

2.4.3 The Multi Wire Proportional Chambers

The first three 1 mm MWPCs (C1, C2 and C3) were also instrumented with the Nanometric readout electronics. Together with the SSDs, the electronics for these chambers consisted of nine crates of latches daisy-chained together. These chambers were constructed by Fermilab and consisted of 128 wires of 1mm pitch in both the x and y views. Unlike the SSDs, it wasn't necessary to use pre-amplifiers and so the signals

Detector	Position (cm)	Width (cm)	Height (cm)	Depth (cm)	Pitch (mm)	Device type
SSD1(y)	79.22	2.8	2.8	.03	.10	SSD
SSD1(x)	74.43	2.8	2.8	.03	.10	SSD
SSD2(y)	109.97	2.8	2.8	.03	.10	SSD
SSD2(x)	100.97	2.8	2.8	.03	.10	SSD
SSD3(y)	137.80	2.8	2.8	.03	.10	SSD
SSD3(x)	129.46	2.8	2.8	.03	.10	SSD
SSD4(y)	166.29	2.8	2.8	.03	.10	SSD
SSD4(x)	158.43	2.8	2.8	.03	.10	SSD
S1	360.	6.35	3.81	.30	n/a	Scintillation
C1(x,y)	560.	12.8	12.8	n/a	1.0	MWPC
C2(x,y)	775.	12.8	12.8	n/a	1.0	MWPC
V1	800.	32.38	8.89	.32	n/a	Scintillation
V1(hole)	800.	11.43	6.35	.32	n/a	n/a
S2	800.	10.79	6.35	.30	n/a	Scintillation
C3(x,y)	987.	12.8	12.8	n/a	1.0	MWPC
V2	1020.	41.91	11.43	.32	n/a	Scintillation
V2(hole)	1020.	13.97	8.25	.32	n/a	n/a
C4(x,y)	1510.	25.6	25.6	n/a	1.0	MWPC
C5(x,y)	2008.	25.6	25.6	n/a	1.0	MWPC
C6(x,y)	2499.	51.2	25.6	n/a	2.0	MWPC
C7(u,v)	3012.	12.8	12.8	n/a	1.0	MWPC
C8(u,v)	3088.	51.2	51.2	n/a	2.0	MWPC
C9(x,y)	3697.	51.2	51.2	n/a	2.0	MWPC
C10(x,y)	4261.	63.8	25.6	n/a	2.0	MWPC
C11(x,y)	4840.	128.	38.4	n/a	2.0	MWPC
C12(x,y)	6154.	128.	38.4	n/a	2.0	MWPC

Table 2.4: The size and z position of the detectors in the spectrometer.

Detector	Voltage (kV)	Detector	Voltage (kV)	Detector	Voltage (kV)
S1	2150.	C1	2.66	C7	2.85
S2	1600.	C2	2.66	C8	2.80
V1E	1800.	C3	2.66	C9/9u	2.91/450.
V1W	1700.	C4	3.82	C10	3.02
V2E	2150.	C5	3.83	C11	3.03
V2W	2150.	C6	2.94	C12	3.15

Table 2.5: The high voltage settings for the MWPCs and the scintillators.

went directly to amplifiers and then into latches. These chambers were also unlike the other MWPCs used in this experiment. As mentioned above they were read out by the Nanometric front end electronics system. They also had high voltage foil planes made of 0.25 mils thick aluminized mylar instead of wire planes (as was true for the rest of the chambers). The nominal high voltage settings for these chambers were as listed in Table 2.5.

The high voltage setting for the rest of the MWPCs tended to be higher than those for the Fermilab MWPCs. Two of the large 1mm (C4 and C7) and all of the 2mm (C6, C8, C9, C10, C11 and C12) chambers were built with high voltage wire planes, made with wires 2 mils thick, instead of foils. C5 was the only large 1mm chamber with high voltage foil planes made of 0.25 mils thick aluminized mylar. All of the chambers had an x sense plane and a y sense plane except C7 and C8. For these two chambers the sense planes were rotated by 45° and were referred to as u and v planes. In addition to an x and a y sense plane, C9 had a third sense plane with a 45° rotation.

The front end readout electronics for these chambers were custom built. Signals from the sense wires went directly into amplifiers and then into latches. The latches in a chamber comprised a sequential chain. Starting at the downstream chamber, each chamber was daisy-chained to the next chamber upstream. In this manner, the rest of MWPCs were linked together in a readout chain. Only wires with hits were read out. To handle the reading of this chain, a custom built interface module was used [20]. This interface module provided the interface between the data acquisition system and the front end readout electronics for most of the MWPCs.

The chambers were run with a gas mixture, by volume of 94.9% Argon, 0.1% Freon and 5% Methylal. The first stage of the gas system was used to achieve the correct mixture of Argon and Freon. After passing through flowmeters, the gas from two bottles of Argon and one bottle of Argon-Freon (0.5% Freon, 99.5% Argon) was merged into one gas line. The next step was to add the Methylal to the gas. In order to have 5% Methylal added to the mixture, the gas had to be bubbled through a reservoir of Methylal near 2° C. The Methylal temperature was maintained by placing the reservoir in a refrigerator with an electronic temperature monitor and controller. After passing through the bubbler the gas was routed to a manifold and distributed to the MWPCs. Each MWPC had an exhaust gas line which was connected to an oil bubbler. The oil bubbler provided two useful functions. First, it prevented a sudden pressure change from forcing air to back flow into a chamber. Second, it provided a visual means for monitoring the gas flow to the chambers. If bubbles formed in the oil, the flow was good.

2.4.4 The Scintillation Counters

Four scintillation counters (S1,S2,V1,V2) were used in the spectrometer. Signals in S1 and S2 were viewed as indications of a potentially good track. Signals in V1 or V2, on the other hand, indicated additional tracks too far out from the beamline and were used as vetos. These events were vetoed because they contained tracks outside of the beam region and therefore could not be Ω^-s that were produced in the downstream target and decayed inside the decay volume of the spectrometer. The dimensions of the counters were as listed in Table 2.4, while the nominal high voltage settings for their photomultiplier tube bases were as shown in Table 2.5. Unlike S1 and S2, the veto counters had two sets of photomultiplier tubes and bases and so two signals. The main reason for having two signals from each veto counter was that these counters had a hole cut out of their centers. Consider a counter with a hole in the center and a tube on the west end only. This type of counter has a good probability of being more efficient at detecting particles passing through the west side of the counter than the east side. If a particle passed through the counter to the east of the hole, the light emitted would have to travel around the hole to reach the counter on the west side. By placing a second tube on the counter, this time on the east end, the east to west asymmetry is removed. All of the signals were discriminated using NIM electronics. The discriminated signals were used in the trigger as well as being latched.

2.4.5 The Analysis Magnets

Two BM109 magnets, with their fields parallel to the vertical, were used to deflect the daughter particles and allow measurement of the particles' momenta. The upstream BM109's z position was 3758.0 cm downstream of the spectrometer origin (see section 2.4.1). The downstream BM109 was 56.0 cm downstream of the upstream BM109 and each magnet was 182.0 cm in length. The apertures of each magnet were centered about the beam axis. Both magnets had an x-aperture of 61.0 cm. The upstream magnet had a y-aperture of 25.4 cm, while the downstream magnet had a y-aperture of 30.5 cm.

The magnetic field of these two magnets was examined using two different techniques. The first technique, a Fermilab field mapping system called "Ziptrack II", measured the field strength of the magnets at different points in a three dimensional lattice setup in the apertures of the magnets. The field integral could then be calculated for the magnets at different y and x positions. Also, because the magnets were ramped just before the start of each spill, tests were done to determine the effect ramping had on the field integral during the spill. Comparisons between the field integral for the ramped mode versus the constant current mode showed differences below 0.08% (less than a few hundred gauss). These small differences were deemed negligible. The total field integral of the upstream and downstream magnet combined was -4.817 Tm. Treating the two magnet system in the thin lens approximation gave a p_T kick of -1.445 GeV.

The second technique for examining the total field integral of the two magnets involved using the reconstruction program. By fitting the Ω^- and the Λ masses, the overall p_T kick of the two magnet system could be better determined. The value found from this method was -1.465. The value determined from this technique was used in the reconstruction because it provided a better measurement of the field integral, and thus the p_T kick, than the first method.

There are several reasons why the second technique provided a better measurement of the field integral. One reason is that the known masses of the Λ and the Ξ^- provide a better calibration standard than was available for the probes used in the first technique. Another reason is that the first technique sampled the field at set intervals while the second technique can be considered a continuous probe. Thus, the first technique had an added uncertainty due to fluctuations in the field between the sampling points. While this uncertainty is probably negligible in the central regions of the magnets, it has a good probability of being significant at the ends of the magnet where fringe fields can change rapidly. In addition to these two differences, the first technique samples the field along straight lines, while charged tracks curve in magnetic fields. This difference in path length should be small, but it still represents a error not present in the second technique.

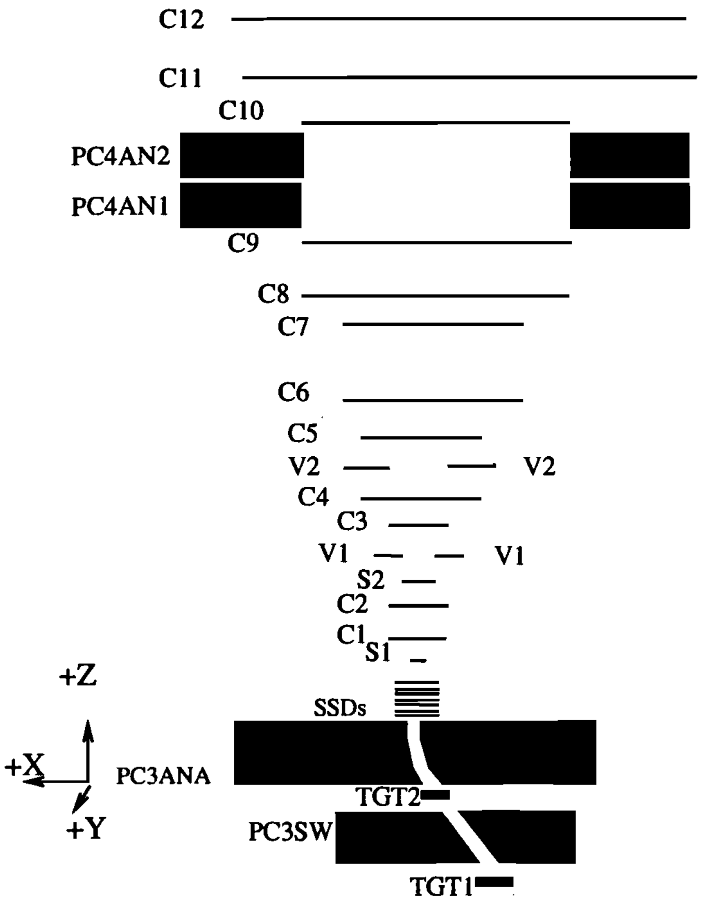

Figure 2.7: The E800 Spectrometer (Plan View). Not to scale.

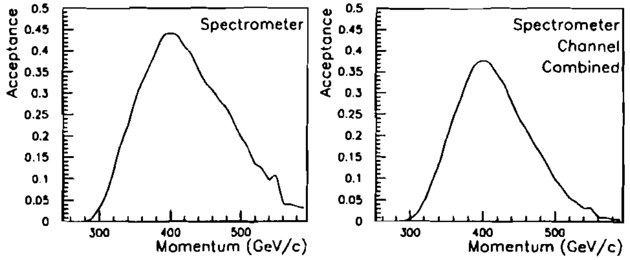

Figure 2.8: The spectrometer acceptance and the combined spectrometer and channel channel acceptance left and right respectively.

2.5 The Trigger

The trigger was designed to be as simple as possible and still provide a rate that could be handled by the readout electronics with a reasonable live time (greater than 60%). The live time can be thought of as the percentage of triggers that are read out. For example, if 30 out of 40 triggers are read out the live time is 75%. The main reason for keeping the trigger simple is that a complex trigger has a larger probability of generating a systematic problem by preferentially selecting a subset of the desired events. Therefore, a simple trigger is always better whenever feasible.

The trigger consisted of two basic parts. The first part of this trigger was very effective in selecting single track particles and consisted of four scintillation counters. To insure a charged particle entered the spectrometer roughly along the same path the beam was expected to take, the trigger required $S1 \cdot S2 \cdot \overline{V1} \cdot \overline{V2}$. Events which satisfied this trigger were primarily π^-s, but also included Σ^-, Ξ^-, Ω^-, and $\bar{p}$ events. The single particle events were very valuable in aligning the spectrometer, as well as in measuring chamber efficiencies. These benefits were the motivation behind writing the events to most of the data tapes at a prescaled rate of between 32 and 1024. To filter out the single track events, while keeping the Ξ^- and Ω^- decays, the trigger was modified to also look for the characteristic "V" topology of Λ decays. To implement this scheme, charged particles were required to pass through the π half of C11 and the proton half of C12. With these additional constraints the trigger became:

Mode	Protons on target (10^{11})	1trk (10^3)	3 trk (10^3)	3 trk read (10^3)	Live time
neutral	1.6	421.	27.6	17.9	65%

Table 2.6: The number of protons on the upstream target, single track triggers, 3 track triggers ("V" topology triggers), 3 track triggers read out, and the live time for a typical spill.

$$S1 \cdot S2 \cdot \overline{V1} \cdot \overline{V2} \cdot C11_{\pi} C12_{proton} \tag{2.1}$$

Table 2.6 shows the trigger rates for a typical spill in the neutral production mode at 1.8 mrad and a hyperon current of 2900 amps. The live time in this mode for a typical spill of 1.6×10^{11} protons on the upstream target was 65%.

2.6 The Data Acquisition System

2.6.1 Software

The software portion of the data acquisition system consisted mainly of a subset of the Fermilab Vaxonline system [21]. This package of programs proved very versatile and user friendly. The specific programs used were divided into two classes. The first class consisted of programs which made it easier to work in the software environment. The second class of programs were responsible for actually moving the data around.

Figure 2.9 shows a simplified diagram of these programs.

The first program which made the environment more friendly was Global Menu [21]. This program allowed different programs to be operated simultaneously from a single terminal screen. Basically, Global Menu allowed communication between the user and the other running programs. The second program in this class was Courier [21]. Courier was a message routing program and allowed messages about the status of the data acquisition programs to be routed over decnet to a window on another computer. This ability to send status messages over Decnet made running the system remotely a great deal easier. Another program that simplified remote running was Run Control [21]. Run Control coordinated Event Builder and Output [21] (taking the data from hardware to tape).

Event Builder, as mentioned above, was one of the programs responsible for actually moving data around. Event Builder handled the link between the hardware and the computer in the readout chain. The data was read out by Event Builder and placed in an event pool. The event pool could be considered a 4 Mbyte storage place in memory where other programs could access any or all of the data. The job performed by Output was to take data from the event pool and write it to tape. The third program in this class was Buffer Manager [21]. Buffer Manager also accessed the data in the event pool. Its job was to send the data over Decnet to an analysis program running on another computer. This allowed a sample of the events being written to tape to be analyzed, without any effect on the data logging process.

2.6.2 Hardware

On the hardware end of the data acquisition system, a Vax 3200 computer with two 8mm tape drives handled the data logging. A Jorway 411 was the interface between the computer and CAMAC. The actual data collection was accomplished by a CAMAC Smart Crate controller (SCC). The SCC would place data in a VME first-in-first-out buffer memory (FIFO) of 16 Mbytes. Finally, a specially built interface between the VME FIFO and CAMAC provided the ability to read the FIFO out over a CAMAC parallel branch highway.

2.6.3 Operational Overview

In order to eliminate any computer overhead on an event by event basis, the data acquisition system was designed to operate in two very distinct stages. The first stage could be called the data collection stage. In this stage, data was read from the spectrometer and placed in temporary storage. The second stage could be called the data logging stage. In the second stage data was moved from storage and written to tape. Figure 2.10 shows simplified flow charts for these two stages.

The data collection stage occurred during the spill. When a trigger arrived, the SCC would begin to systematically read out the spectrometer. First the large MWPCs would be read out. Next the small 1mm MWPCs and the SSDs would be read. Finally, the designated scalers, latches, and ADCs would be read. After each dataword was read by the SCC, the SCC would write it to the FIFO memory. In this manner the SCC would continue to write the datawords of an event to the FIFO until the entire event had been written. Upon completing the process of reading and writing an event, the SCC would inform the trigger electronics that it was ready for another trigger. The SCC would then wait until another trigger occurred, at which point the process would be repeated. The entire process would take approximately 300 μsec for a typical event of approximately 120 words. During a nominal spill of 23 seconds, this process was repeated for 20,000 to 30,000 triggers with a live time of about 65%. While data was being collected, the computer did not interact with the data taking electronics.

Once the spill ended, so did the data collection stage. Next the data logging stage would begin. A signal called T6 was used to announce the arrival of the end of a spill. At that time the computer was told to commence reading the CAMAC spill scalers. These scalers contained information on the trigger element hits, counter rates, and other diagnostic quantities summed over the entire spill. Next the computer began reading out the contents of the FIFO memory. Finally, all of this information had to be written to tape.

To read the scalers, T6 would be used to raise a specific CAMAC LAM, which will be referred to as LAM 7. Event Builder would see this LAM 7 and execute the necessary steps to read the scalers and place the data in the event pool. Next another specific LAM, which will be referred to as LAM 11, would be raised by a gated pulse generator. A LAM 11 would cause Event Builder to execute a different list of commands. This new list was designed to handle the reading of data out of the FIFO memory and the placing of it into the event pool. The software was originally designed to read out one event at a time with a maximum size of 4000 datawords. Because of this limitation, the system was unable to handle reading out the entire FIFO (up to 8 Mbytes) with just one LAM 11. Therefore, a scheme was devised where multiple LAM 11's were generated and 4000 datawords were read for each LAM 11. At the end of the LAM 7 list a signal was sent to open the gate of a pulse generator, and each of these pulses were used as a LAM 11 (Figure 2.11). This scheme proved to work exceedingly well.

While Event Builder was busy placing data in the event pool, Output would take the data in the pool and write it to tape. These operations continued until all of the data was written to tape. The time required to empty the FIFO into the event pool typically took on order of 30 seconds for a spill, while to finish writing to tape typically took about 15 seconds longer. Meanwhile Buffer Manager was also looking at the event pool and sending data over Decnet to an analysis program on another computer. Since the analysis program was CPU intensive, having it run on a separate computer allowed data to be analyzed without effecting the process of logging all of the data to tape.

The data itself was separated into runs. Each run consisted of approximately 500,000 events written to 8mm tape. Because the storage capacity of these tapes was so large, typically eight to ten runs were put on each tape. Under normal operating conditions the length of time for a run was about 20 minutes, while a typical run in the Spin Transfer mode took several hours.

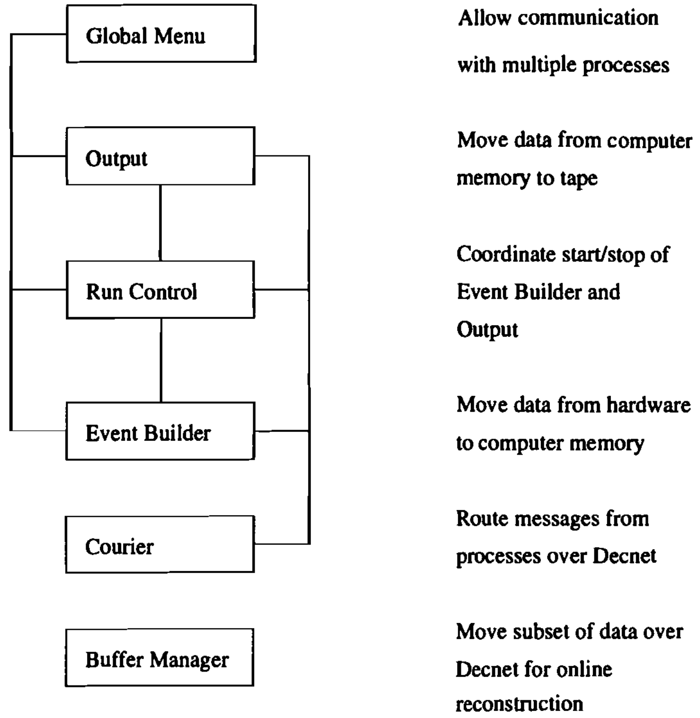

Figure 2.9: Simplified diagram of the Vaxonline programs used. The lines represent communication between the individual programs.

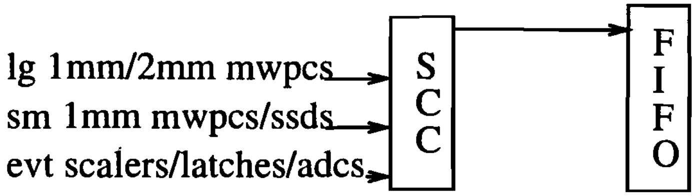

Data collection stage

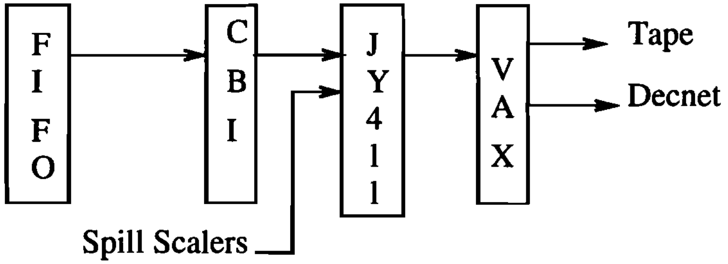

Data logging stage

Figure 2.10: Simplified flowcharts for the two data acquisition stages.

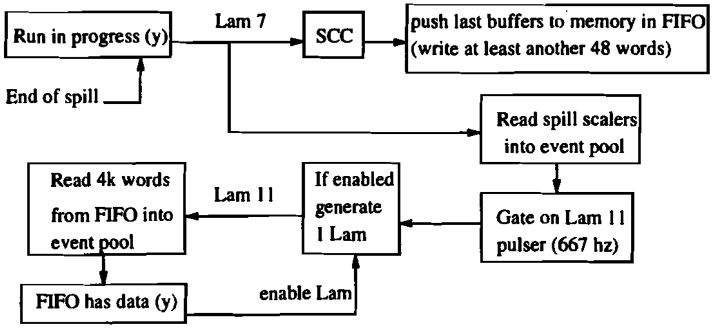

Flow chart for reading data into the event pool

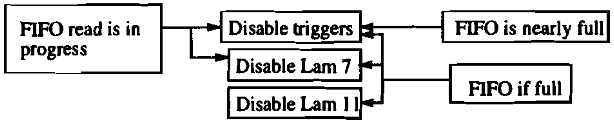

Readout veto conditions

Figure 2.11: Flowcharts for generating multiple LAM 11 signals to read out the FIFO.

Chapter 3

The Reconstruction

3.1 Introduction

The decay sequences of interest were $\Omega^- \rightarrow \Lambda K^-$ followed by $\Lambda \rightarrow p\pi^-$, and $\Xi^- \rightarrow \Lambda\pi^-$ followed by $\Lambda \rightarrow p\pi^-$. These three track topologies allowed events to be completely reconstructed using only the MWPC wire hits. In the following discussion, the Ω^- and the Ξ^- will be referred to as the parent. Also, the K^- from the Ω^- decay and the π^- from Ξ^- decay will be referred to as the primary meson. The reconstruction did not distinguish between different types of particles, except for charge, until the mass of the parent was calculated. At this point the mass was calculated twice, once assuming the primary meson was a K^- and once assuming it was a π^-. This allowed both Ω^- and Ξ^- decays to be treated essentially the same by the reconstruction program.

The analyzing magnets in the spectrometer were orientated so that charged tracks would bend in the x view only, thus one characteristic of the topology was three straight tracks in the y view. In addition, the proton had the highest momentum of the three daughter particles as well as the opposite charge of the two mesons. Therefore, another important characteristic of the topology was that the stiffest track bent in the opposite direction of the other two tracks in the x view.

Ideally, there should have been three hits in each chamber view downstream of the daughter Λ decay. There were several different factors that could alter the number of hits in a chamber view for this topology. First, less than perfect chamber efficiency caused hits to be lost. Second, a track could miss a chamber and so not register any hits in that chamber. Third, two tracks could be so close together that they hit the same wire. There were also several factors that could cause too many hits in a chamber. The first of these factors was electronic noise in the chamber. The second was that a scattered electron (δ ray) could go sideways through a chamber causing many wires to register a hit. The third was if the track passed nearly midway between two wires, both wires might record a hit. Therefore, the number of hits in each chamber view could only be used as a loose constraint for the desired three track topology.

There were roughly 1.35×10^9 triggers written to tape in this experiment including single track events for monitoring purposes. Because the trigger was simple, the percentage of good three track events written to tape was on order of 3% of all triggers. Therefore, a simple filter to remove triggers that had no possibility of being reconstructed as good three track events was used. The first pass analysis, employing simple hit counting criteria, provided this filter and reduced the number of triggers by roughly a factor of 3. The reconstruction program was designed to process as many events as possible as quickly as possible. Roughly 450 million triggers were processed. To accomplish this goal, the reconstruction first imposed additional hit counting criteria before attempting to reconstruct an event. This second set of hit counting cuts was designed to eliminate events that did not have enough information to be reconstructed well. This second round of hit counting cuts reduced the data set by roughly a factor of 2.2, leaving about 200 million triggers to be reconstructed.

Because of the size of this data set, the reconstruction program needed to be as efficient as possible. In order to accomplish this task, up to three attempts were made at reconstructing each trigger. Figure 3.1 shows a simplified diagram for the structure of the multipass reconstruction. The first attempt, or pass, was designed to be quick and efficient. This pass took on order of 0.02 seconds per trigger on a VAX 4000 workstation. If the trigger failed the first pass, it was sent to the second pass. The second pass reconstruction was roughly a factor of 4 slower than the first, but recovered a significant percentage of events. Events that failed the second pass were sent to a third pass which recovered a smaller percentage of events and took approximately the same time per event as the second pass. The percentage of events in the final sample from each pass is listed in Table 3.1.

Pass	Percent
First	68.3%
Second	18.3%
Third	13.4%

Table 3.1: The percentage of good events in the final sample from each of the reconstruction passes.

Once all three daughter tracks were reconstructed separately, they were fit to the Ω^- and Ξ^- hypotheses through the use of geometric and kinematic constraints.

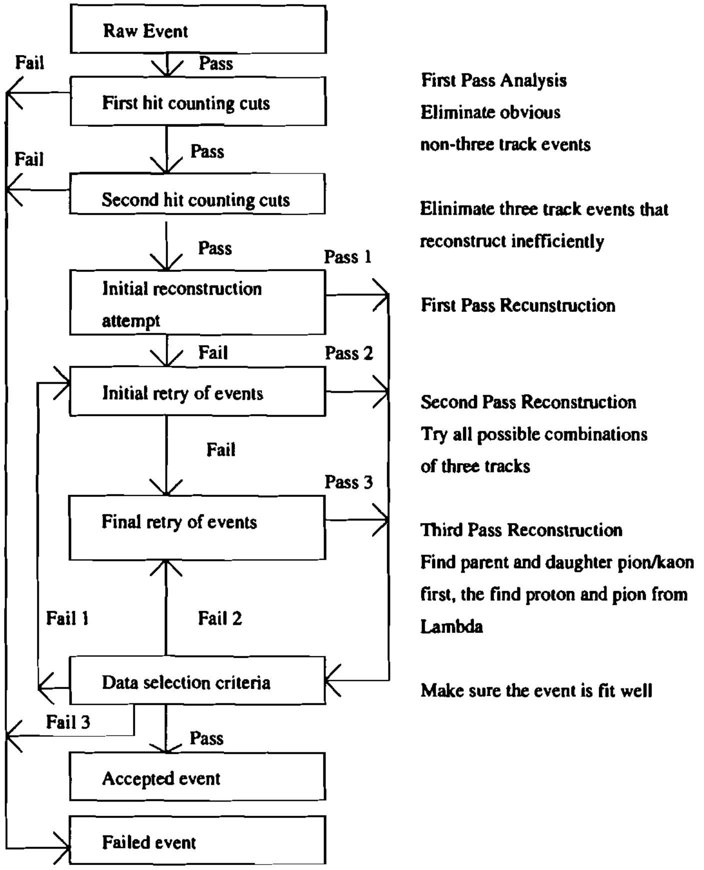

Figure 3.1: A simplified flowchart for the reconstruction. The numbers 1, 2 and 3 stand for the first, second and third pass reconstructions respectively.

Selection Criteria
At least 3 of the planes C6x, C6y, C7x, C7y, C8x, C8y have at least 2 hits
At least 2 hits in C10x,C11x,C12x
At least 4 of the planes C6y, C7y, C8y, C9y, C10y, C11y, C12y have at least 2 hits

Table 3.2: The first pass analysis selection criteria.

Production Mode	Angle (mrad)	Current (amps)	Runs	Triggers	Three Track Candidates
Neutral	-0.0	-2900	172	84187513	39097574
Neutral	0.0	-2900	170	82531343	38000350
Neutral	-1.8	-2900	757	374297889	110232099
Neutral	-1.8	-750	289	142700032	45346166
Neutral	1.8	-2900	711	346982603	102177861
Neutral	1.8	-750	308	150467562	46929723
Spin Transfer	-1.8	-2900	171	84086479	30240120
Spin Transfer	1.8	-2900	182	87777817	34212605

Table 3.3: The first pass analysis event totals.

3.2 The First Pass Analysis

The first pass analysis was designed as a filter to perform two important functions. The first function was to decode the raw data words into the chamber and wire numbers they represented. The second function was to count the number of hits in each chamber view and eliminate events with too few hits to be good three track candidates. The selection criteria used are listed in Table 3.2. Table 3.3 shows the number of candidate events before and after the first pass analysis.

Note that since a loose three track trigger was used (see section 2.5), most of the events lost due to these selection criteria were not three track events. Approximately 33% of the triggers were potential three track candidates. In addition, simple criteria

Selection Criteria
All of the planes C6y, C9y, C10y have at least 2 hits
All of the planes C6x, C9x, C10x, C11x have at least 2 hits
No more than 2 of the planes C6y, C8y, C9y, C10y, C11y, C12y, C6x, C8x, C9x, C10x, C11x, C12x have 5 or more hits

Table 3.4: The additional hit counting selection criteria.

like hit counting were not expected to bias the data.

3.3 Additional Hit Counting Requirements

Before a trigger was sent to the first pass reconstruction, additional hit counting criteria were applied. These hit counting cuts eliminated triggers that could not be properly reconstructed. Either they did not have enough hits or they had far too many hits. The criteria used are listed in Table 3.4. These requirements removed approximately 55.4% of the triggers. The remaining roughly 200 million triggers were sent to the first pass reconstruction.

3.4 The First Pass Reconstruction

The first step in this pass was to identify three tracks in the y view using five of the six 2mm chambers (C6, C9, C10, C11 and C12). Next, the tracks upstream of the analyzing magnets were found in the x view of the 2mm MWPCs. The next step was to try matching the y view tracks and the upstream x view tracks using the U plane of C9 and the U and V planes of C8. With the upstream x tracks matched to the y tracks, the next task was to find the downstream x tracks and connect them to the

upstream x tracks at the bendplane of the two analysis magnets. The bendplane of the two magnets was defined using a thin lens approximation.

The next step in the reconstruction was to take the hits for the three tracks and do a simultaneous fit in x and y to the three track topology. Here 13 parameters were solved for, including the decay vertices for the parent and the Λ as well as the slopes of the daughter tracks. In addition, the geometric chi-squared per degree of freedom was calculated χ^2_G/DF. If an event passed this preliminary fit, then hits from the remaining 1mm chambers were added to the tracks and the event was refit.

The parent and the Λ vertices can be upstream or downstream of any of the 1mm chambers. Therefore, when assigning 1mm hits to a daughter track care must be taken not to assign hits from the parent track. Since no 1mm hits were allowed to be shared by any of the tracks, the order in which the hits were assigned to the tracks was important. The 1mm hits were assigned to the primary meson track first, the π^- track from the Λ decay second, the proton track from the Λ decay third, and the parent track last. Because of the expected decay topology, the Λ decay π^- and proton tracks should not be upstream of the primary meson track. Therefore, all hits for the Λ decay proton and π^- tracks were required to not be farther upstream than the farthest upstream chamber with a hit for the primary meson. Also, any parent hit was required to be upstream of the farthest upstream chamber with a hit for the primary meson. The 1mm tracks were assigned to a track if the residual difference was 1.44 wire spacings or less.

The next step in the first pass was to perform a kinematic fit. In this fit, the momenta of the proton and π^- (from the Λ decay) were varied within uncertainties and the calculated Λ mass was constrained to its known value. The fit also calculated a kinematic chi-squared, χ^2_K. Note that both the geometric fit and the kinematic fit only used hits associated with the daughter tracks. No hits assigned to the parent track were used in either fit.

After the kinematic fit was completed, the parent track hits, along with all of the primary meson track hits were used to make a separate determination of the parent decay vertex. Choosing the best value for the decay vertex of the parent depended on several factors. First, the method required a good parent track in the SSDs and so only gave a good fit for events which decayed downstream of the SSDs. Second, it was found that if the two solutions for the parent vertex differed by more than 300.0 cm, then the solution farther upstream would statistically provide a more symmetric distribution for the difference between the the real and reconstructed values. Therefore, for this class of events the upstream solution was used. Finally, if both solutions were downstream of the SSDs and within 300.0 cm of each other, then the vertex from the fit to the parent track and the primary meson track was the better solution and was used. Using the parent vertex, the parent track was traced back to the downstream target, and the data tested to determine if the solution came form the target within expected uncertainty (see section 3.5 below).

The final fit in the first pass reconstruction was used to improve the determination of the daughter Λ decay vertex. All events that were successfully reconstructed were passed to this fitter. This vertex fitter constrained the tracks at C8 for the proton and π^- from the Λ decay and allowed their momenta, the Λ decay vertex and the Λ mass to change. This fitter improved the decay vertex of the Λ and yielded a narrow Λ mass width. After this fit was completed, all successfully fit events were written to a summary file.

3.5 Criteria for Data Selection

There were two categories of data selection criteria applied to the events. Any events failing in either category were sent to the next reconstruction pass. The first category was simply events that failed to be fit by either the geometric fitter or the kinematic fitter. All of these events had no solution and were sent to the next pass of the reconstruction.

Parameter	Lower Limit	Upper Limit
m_{Ξ^-}	1.306 GeV/c^2	1.336 GeV/c^2
m_{Ω^-}	1.657 GeV/c^2	1.687 GeV/c^2
χ^2_G/DF	N/A	4.0
χ^2_K	N/A	15.0
Y_T	-0.8 cm	0.8 cm
X_T	-0.9 cm	0.9 cm

Table 3.5: The Data Selection Criteria.

The second category was events that passed both the geometric fitter and the kinematic fitter, but didn't pass the event selection criteria. These were events that had a solution, but were not fit very well. Therefore, these events were sent to the next reconstruction pass to see if a better fit could be found. In addition to removing data from the tails of the mass, χ^2_G/DF, and χ^2_K distributions, data were also selected for refit based on the projected downstream target (target 2) position of the reconstructed parent track in both x and y (X_T and Y_T). Table 3.5 lists the data selection criteria. Since the experiment was designed to collect both Ξ^- and Ω^- events, an event needed to pass either the m_{Ξ^-} or the m_{Ω^-} mass requirements.

The data selection criteria were chosen to reject possible background or badly reconstructed events from the sample. About 7.1% of the triggers passed this first reconstruction step while 37.5% were sent on to be refit.

3.6 The Second Pass Reconstruction

The second pass reconstruction was called for any event that failed to pass either of the data selection categories. This reconstruction pass attempted to find all possible solutions for an event and pick the one with the best fit [19]. The method involved first finding all the possible y tracks using C6, C9 and C10 and grouping them in sets of three (one for the proton and one for each meson). For each set of three tracks, the proton and the π^- from the Λ decay were required to intersect upstream of C6. Now an attempt at finding tracks in the x view was made. The search for upstream x tracks used C6 and C9, while C10 and C11 were used for finding downstream x tracks. The upstream and downstream tracks were next linked together to form an overall x track for a particle if their separation at the bendplane of the analysis magnets (in a thin lens approximation) was not greater than 0.5 cm. The final step in finding a three track topology was connecting the x view tracks to the y view tracks. As in the first pass reconstruction, the rotated planes in C8 and C9 were used to accomplish this task.

There were several additional topological constraints imposed on the trial solutions. The first constraint was that no tracks crossed or shared hits in the y view between C6 and C11. The second constraint was that no tracks crossed or shared hits in the x view between C6 and C9.

All of the trial solutions for each event were next sent to a series of fitting routines. Unlike in the first pass reconstruction, the CPU time required to perform the second pass was a problem, and so these fitting routines were designed to eliminate the bad solutions as quickly as possible. Since the algebra required for doing a geometric fit to the Λ topology was exactly soluble and thus could be done quickly, the first fitter looked for a good geometric fit for the Λ topology. The chi-squared per degree of freedom was required to be 10 or less, otherwise the solution was rejected.

The second fitter looked at the geometric fit to the three track topology as described in section 3.4. Unlike in the first pass reconstruction though, the requirement on the geometric chi-squared per degree of freedom was not as strict since this was still at a preliminary stage in the second pass. Only solutions with $\chi^2_G/DF < 10$ were passed on to the third fitter, all others were eliminated.

The third fitter was the kinematic fitter described in section 3.4. Once again since this was still only a preliminary stage of the fit, a looser cut on the chi-squared was used than in the first pass reconstruction. In this case, only solutions with $\chi^2_K < 100$ were passed on to the next stage.

The next stage of the second pass reconstruction was the assignment of hits from the rest of the 2mm chambers and the 1mm chambers. The assignment of hits from the 1mm chambers was done in a different manner than those from the 2mm chambers. The Λ was required to decay upstream of the 2mm chambers, so none of the 2mm hits can belong to the parent track. The 2mm chamber hits were assigned by calculating the residual difference between the hit and the fitted tracks. If this residual difference was 2.5 wire spacings or less, the hit was assigned to the track. The 1mm hits were assigned according to the same rules used in the first pass reconstruction.

With all of the hits assigned, the next step was to perform the final fits for the solutions. First the geometric fitter was called, and then the kinematic fitter as was done in the first pass reconstruction. Next all the the solutions were checked to see if they passed the data selection criteria for mass, χ^2_G/DF, and χ^2_K listed in Table 3.5. Finally, the best solution for the parent vertex was determined and the parent track was traced back to the downstream target.

If more than one solution was still left, the remaining solutions were checked for the one with the best fit. First the smallest value for χ^2_G/DF was determined for the remaining solutions. Next any solution with $\chi^2_G/DF > ((\chi^2_G/DF)_{min} + 0.2)$ was rejected. Finally, from the set of solutions within 0.2 of $(\chi^2_G/DF)_{min}$, the one with the lowest value of χ^2_K was chosen. The idea was that the solution with the lowest value of χ^2_G/DF had the best chance of having all the hits assigned correctly. The geometric chi-squared per degree of freedom did not distinguish differences below 0.2 and the best fit to the Λ mass was used.

If the event failed to have a good solution which passed all of the data selection criteria, then the event was sent to the third pass reconstruction. Otherwise, a final fit was performed to improve the Λ decay vertex as described previously and the event was written out to a summary file as was done in the previous pass. Approximately 1.9% of the triggers passed this reconstruction stage while the remaining 35.6% were sent to be refit.

3.7 The Third Pass Reconstruction

The third pass reconstruction was called for events which failed to have a good solution after the previous passes. The order of the three passes was chosen to minimize the overall execution time of the reconstruction program. The approach to the reconstruction here differed considerably from the previous two passes. In this pass, the main idea was to use the upstream 1mm chambers and the SSDs to find the parent track. First the primary meson track was searched for under the assumption that its track originated at the parent decay vertex and thus had to intersect the parent track. Several possible solutions were found, and for each solution the remaining hits were used in a two track fitter for the Λ decay to find the proton track and the other π^- track.

Each solution with a good Λ was sent to the geometric and kinematic fitters used in the first and second pass reconstructions (see section 3.4). Next, as in the first two passes, the best solution for the parent vertex was determined and the parent track was traced back to the downstream target. Once again the data selection criteria were invoked to determine if a valid solution was found. If more than one good solution still remained, then the best solution was selected using the same method as in the second pass reconstruction. At this point, if an event failed to have a good solution which satisfied all of the data selection criteria, the event was removed from the sample. If the event did have a valid solution, a final fit was performed to improve the Λ decay vertex and the event was written out to a summary file in the same manner as the previous passes. Approximately 1.4% of the triggers passed the final reconstruction pass.

Production Mode	Angle (mrad)	Current (amps)	Ξ^- Candidates	Ω^- Candidates
Neutral	-0.0	-2900	1875620	230205
Neutral	0.0	-2900	1818638	223249
Neutral	-1.8	-2900	14881637	1873727
Neutral	-1.8	-750	5238496	726001
Neutral	1.8	-2900	14474537	1822051
Neutral	1.8	-750	5510850	765328
Spin Transfer	-1.8	-2900	1275716	161010
Spin Transfer	1.8	-2900	1201471	155917

Table 3.6: The good Ξ^- and Ω^- event totals for reconstructed real data.

Finally, the number of events in the real data that passed the data selection criteria as candidates for either a good Ξ^- or Ω^- are listed in Table 3.6. Note that most of the events are Ξ^-s. At this stage approximately 10.4% of the triggers were still candidates.

3.8 Additional Omega Minus Selection Criteria

Since the beam contains approximately 80 times the number of Ξ^-s as Ω^-s, the largest background in the Ω^- sample comes from the decay $\Xi^- \rightarrow \Lambda\pi^-$ which also reconstruct as Ω^-. The standard selection criteria do a good job of eliminating most of these background events, but fail to remove a large background of them (see Figure 3.2). There are two classes of $\Xi^- \rightarrow \Lambda\pi^-$ decays that end up as background to the $\Omega^- \rightarrow \Lambda\pi^-$ sample. The first class is composed of Ξ^- events that fit both the desired Ξ^- and Ω^- decay hypotheses very well. The second class involves Ξ^- decays inside the charged collimator which reconstruct as good Ω^- events but not as good Ξ^- events.

The first class of background events could be eliminated by making a cut on the Ξ^- mass, thus eliminating any event which reconstructs as both a good Ξ^- and a good Ω^-. This type of cut works fairly well, but it also eliminates any Ω^- events which also reconstructed as Ξ^- decays. It turns out that there is another way of removing this class of Ξ^- background that works better [7, 22]. Consider the spherical coordinate system in the Ω^- rest frame with axes parallel to the spectrometer axes. Note that the Ω^- momentum direction is mostly along the spectrometer $\hat{z}$ axis in the lab frame. Let $\cos\theta_K = \hat{K}^- \cdot \hat{z}$ and $\phi_k = \tan^{-1}(\hat{K}^- \cdot \hat{y}/\hat{K}^- \cdot \hat{x})$. It turns out that the Ξ^- background events fall in the region $\cos\theta_K \leq -.775$. Figure 3.3 clearly shows a dark band in this region. A Monte Carlo study of these events also show a dark band in the same region as is evident in Figure 3.8 (see section 3.8.1 for more detail on the Monte Carlo study of these events). Thus, a requirement of $\cos\theta_K > -.775$ was imposed.

These spherical angles also prove to be very helpful at eliminating the second class of Ξ^- background. These events have the daughter π^- track bending in the magnetic field and so do not reconstruct as good Ξ^- decays. In this case it turns out that the background events are well described by $\cos\theta_K \leq (\mid 0.008125 \times \phi_k \mid -1.8125)$, which can be seen as two darkened regions in Figure 3.4. The Monte Carlo distribution for these background events is shown in Figure 3.9 and exhibit the same dark regions. Therefore, a second angular requirement that $\cos\theta_K > (\mid 0.008125 \times \phi_k \mid -1.8125)$ was used. The number of good Ω^- candidates remaining after these two additional cuts are listed in Table 3.7. From the Monte Carlo study these cuts eliminated 5.0% of the good Ω^-s while reducing the background by over 99.9%. Figure 3.5 shows a plot of $\cos\theta_K$ versus ϕ_k after both of these cuts were imposed. The mass plots are shown in Figure 3.6 with the additional selection criteria imposed and demonstrate a dramatic reduction in the background.

At this point, it is estimated that there still remains a 3% background in the $\Omega^- \to \Lambda K^-$ sample. This additional background is primarily due to misreconstruction of the decay chain $\Omega^- \to \Xi^0 \pi^-$ followed by $\Xi^0 \to \Lambda \pi^0$.

Production Mode	Angle (mrad)	Current (amps)	Ω^- Candidates
Neutral	-0.0	-2900	14110
Neutral	0.0	-2900	13727
Neutral	-1.8	-2900	135653
Neutral	-1.8	-750	44056
Neutral	1.8	-2900	131047
Neutral	1.8	-750	46221
Spin Transfer	-1.8	-2900	14467
Spin Transfer	1.8	-2900	14527

Table 3.7: The good Ω^- event totals for reconstructed real data after angular cuts to suppress background from Ξ^- decays.

3.8.1 Monte Carlo Study of the Additional Omega Minus Selection Criteria

The additional selection criteria for the Ω^- sample were studied using the Monte Carlo. In order to study these cuts, it was necessary to have Ξ^- events that decayed inside the collimator in addition to those that decayed in the nominal decay volume (downstream of the collimator). Because the acceptance of decays inside the collimator was small, a large number of Monte Carlo events were generated to insure there were enough of these decays in the final sample of reconstructed events. Because of the low acceptance of collimator decay events, the final sample was mostly composed of decays in the nominal decay volume.

The Monte Carlo was used to generate a sample of 900,000 Ξ^- decays. Since the reconstruction program had no way of distinguishing between real data and Monte Carlo data, these Ξ^- events were reconstructed in exactly the same way as the real data. As was seen in the real data, the standard selection criteria do a good job of eliminating these background events, but fail to remove all of them. Figure 3.7 clearly shows that there are some Ξ^- events which pass the standard selection criteria for Ω^- events. These events represent a slightly declining background in the Ω^- mass range. Notice that most of these events also look like good Ξ^- events as evidenced by the fairly clean Ξ^- mass peak.

A plot of $\cos\theta_K$ versus ϕ_K for these Monte Carlo events is shown in Figure 3.8. Most of these events fall in a dark band below $\cos\theta_K = -.775$. Next a requirement that $\cos\theta_K > -.775$ was imposed. As in the case of real data, this requirement removed any Monte Carlo Ξ^- events that reconstructed as both good Ω^-s and good Ξ^-s. Figure 3.9 shows a plot of $\cos\theta_K$ versus ϕ_K for the Monte Carlo events after imposing $\cos\theta_K > -.775$. Almost all of the remaining events in Monte Carlo sample fall into two regions which can be described by $\cos\theta_K \leq (\mid 0.008125 \times \phi_k \mid -1.8125)$. Like the first angular requirement, the second angular requirement suggested by the real data is also motivated by Monte Carlo background studies. The second angular requirement was $\cos\theta_K > (\mid 0.008125 \times \phi_k \mid -1.8125)$. After these two cuts were made, it is estimated that Ξ^- decays represented a background of less than 1%.

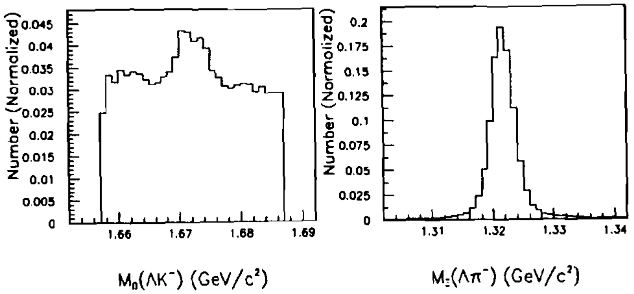

Figure 3.2: Normalized plots of Ω^- and Ξ^- masses for a subset of the Ω^- candidate events.

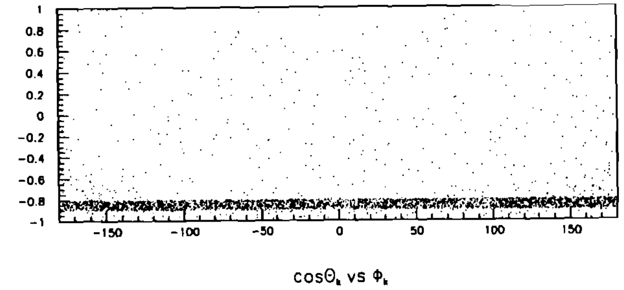

Figure 3.3: Plot of $\cos\theta_K$ versus ϕ_K for a subset of the Ω^- candidate events before any angular cuts.

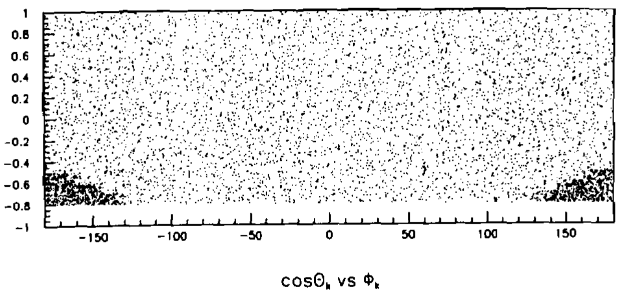

Figure 3.4: Plot of $\cos\theta_K$ versus ϕ_K for a subset of the Ω^- candidate events after $\cos\theta_K > -.775$ was imposed.

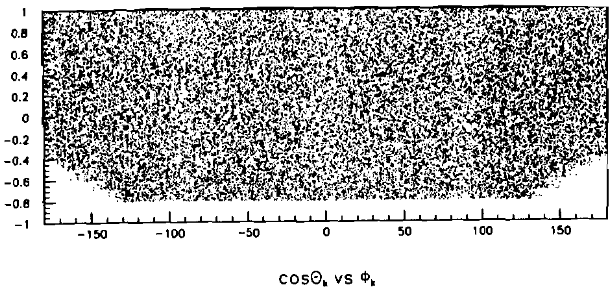

Figure 3.5: Plot of $\cos\theta_K$ versus ϕ_K for a subset of the Ω^- candidate events after $\cos\theta_K > -.775$ and $\cos\theta_K >$ (| $0.008125 \times \phi_k$ | -1.8125) were imposed.

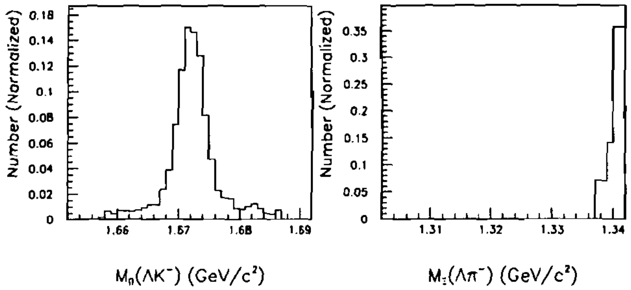

Figure 3.6: Normalized plots of Ω^- and Ξ^- masses for a subset of the Ω^- candidate events after $\cos\theta_K > -.775$ and $\cos\theta_K >$ (| $0.008125 \times \phi_k$ | -1.8125) were imposed.

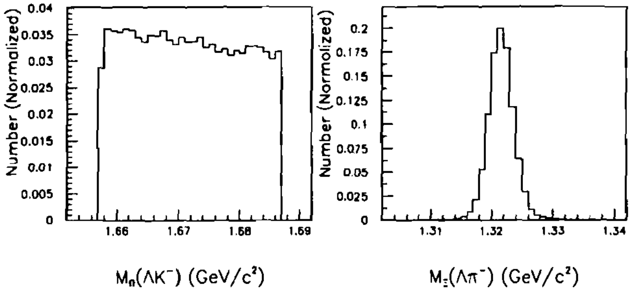

Figure 3.7: Normalized plots of Ω^- and Ξ^- masses for Monte Carlo Ξ^- events which reconstruct as Ω^- candidate events.

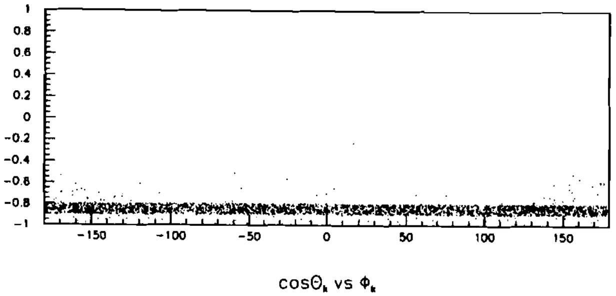

Figure 3.8: Plot of $\cos\theta_K$ versus ϕ_K for Monte Carlo Ξ^- events which reconstruct as Ω^- candidate events before any angular cuts.

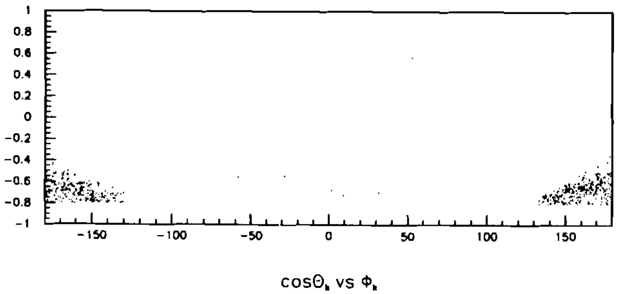

Figure 3.9: Plot of $\cos\theta_K$ versus ϕ_K for Monte Carlo Ξ^- events which reconstruct as Ω^- candidate events after $\cos\theta_K > -.775$ was imposed.

3.9 The Monte Carlo

A Monte Carlo program generated events which simulated the real data in most aspects. This program proved to be a valuable tool for designing the experiment. The program also provided the ability to carefully study the reconstruction program, which is an important part of any measurement where systematic effects may be significant. Along with an improved understanding of the reconstruction program, the Monte Carlo also provided a means for better understanding the data. The basic structure of the Monte Carlo program was simple. First events were generated in the downstream target. Then they were projected through the experiment until they decayed. Next their decays were generated and the daughter particles were projected through the spectrometer. Finally, the events were checked to see if they satisfied the trigger requirements of the experiment.

The event generation was started in the downstream target. The events were generated in this target with a gaussian distribution in x and y. The gaussian shape was chosen since it best represented the expected shaped of the neutral beam incident on the target. The next step was to pass the event through a curved collimator in a magnetic field.

The lifetimes listed in the Review of Particle Properties [23] were used to generated the decays of the Ω^-, Ξ^- and the Λ particles. There were no boundary requirements placed on the decay positions of these particles. All of these tracks were projected through the spectrometer unless they decayed somewhere in the spectrometer. While projecting these tracks through the spectrometer, the Monte Carlo also generated multiple scattering effects. Because of coulomb multiple scattering, a track could experience a change in direction at each piece of material in its path. A list of the spectrometer material in the beam path was compiled as a function of length and type of material. The scattering angle (θ_{scat}) was generated as a gaussian distribution with a width

θ_0 [23].

$$\theta_0 = \frac{13.6MeV}{\beta cP} z\sqrt{x/X_0}[1 + 0.038\ln(x/X_0)] \tag{3.1}$$

In the above equation, βc, P and z are the velocity, momentum and and charge number of the incident particle. The ratio of x/X_0 is the thickness of the scattering material measured in units of radiation lengths. The entire spectrometer contained less than 0.1 radiation lengths of material giving typical multiple scattering angles for the entire spectrometer of 8×10^{-3} mrad.

The direction of each daughter track was also changed by the analyzing magnets. The charged daughter particles were bent in the x direction in the two analyzing magnets. There was evidence in the real data that the fields in these magnets were nonuniform at the 1.5% to 2% level. Note that this is also the level of disagreement between the two methods of measuring the field in the analyzing magnets (see section 2.4.5). To approximate this effect in the Monte Carlo data, a field map was used which was symmetric in x and y about the center of each magnet aperture. For values of x and y at the entrance of the magnet, the y component of the field (B_y) in each magnet was:

$$B_y = B_0\left[1.0 + A(|x| - 4.0) + B(|x| - 4.0)^2 + C(|y| - 4.0) + D(|y| - 4.0)^2\right] \tag{3.2}$$

$$\left\{ \begin{array}{cc} \left(\begin{array}{c} A = 5.454\times10^{-3}\,cm^{-1} \\ B = -3.637\times10^{-4}\,cm^{-2} \end{array} \right) & \text{if } |x| \geq 4.0 \\ A = B = 0.0\,cm^{-1} & \text{otherwise} \end{array} \right\}$$

$$\left\{ \begin{array}{cc} \left(\begin{array}{c} C = 3.286\times10^{-3}\,cm^{-1} \\ D = -2.857\times10^{-4}\,cm^{-2} \end{array} \right) & \text{if } |y| \geq 4.0 \\ C = D = 0.0\,cm^{-1} & \text{otherwise} \end{array} \right\}$$

where B_0 was the full field integral for the magnet (2.666 Tm and 2.244 Tm for the first and second magnets respectively).

For each particle, B_y was calculated based on the particle's entrance position to the first magnet and used to trace the particle through that magnet. Next, the particle was projected to the entrance of the second magnet. B_y was calculated based on the particle's entrance position to the second magnet, and the particle was traced through the magnet.

With the charged particles projected through the spectrometer, their calculated x and y positions at each chamber were used to assign the wire hits. The wire pitch of the chamber multiplied by the difference between the chamber center, determined from alignment studies of the real data, and the x or y position of a track at the chamber were used to calculate each wire hit. There were several factors that could effect the number of hits in a chamber for each event. The first of these was the multiple hit probability. If a track passes within 0.1 mm of the midpoint between two wires, then both wires may register a hit. Another effect which can cause an increase in the number of wire hits was random noise, which manifested itself as wires recording hits that were not correlated to any of the tracks. The number of wire hits seen could also be decreased because of inefficiencies. In Table 3.8 the efficiencies used in the Monte Carlo are listed. These efficiencies were determined from one tape of data, and were representative of the approximate efficiencies for the entire data sample. Another possible loss of wire hits were dead wires, which were wires that never registered any hits. The dead wires were easy to see in the chamber distributions for real data and thus could be easily included in the Monte Carlo.

The final check before writing out the events was to see if the event passed the trigger requirement of a hit in the pion side of C11 and the proton side of C12. Events which made it past the trigger were written out to a file with the same format as the real

Detector	Efficiency	Detector	Efficiency
SSD1(y)	0.62	SSD1(x)	0.83
SSD2(y)	0.83	SSD2(x)	0.81
SSD3(y)	0.85	SSD3(x)	0.82
SSD4(y)	0.82	SSD4(x)	0.85
C1(y)	0.93	C1(x)	0.93
C2(y)	0.94	C2(x)	0.92
C3(y)	0.94	C3(x)	0.995
C4(y)	0.73	C4(x)	0.74
C5(y)	0.94	C5(x)	0.93
C6(y)	0.99	C6(x)	0.98
C7(y)	0.98	C7(x)	0.95
C8(u)	0.98	C8(v)	0.96
C9(y)	0.96	C9(x)	0.95
C10(y)	0.99	C10(x)	0.98
C11(y)	0.98	C11(x)	0.96
C12(y)	0.97	C12(x)	0.96

Table 3.8: The chamber efficiencies used in the Monte Carlo.

data. Thus, the reconstruction program did not distinguish between a file containing real or Monte Carlo data since they both had the same format.

3.10 The Performance

The two most important criteria for measuring the performance of the reconstruction program were how accurately the events were reconstructed, and how uniformly it accepted events. To answer the first question, it is best to examine the accuracy of the program for distributions directly related to the measurement of the Ω^- polarization and α decay asymmetry. In this case, the distributions for $\cos\theta_x$, $\cos\theta_y$, $\cos\theta_z$, and $\cos\theta_a$ are sufficient. θ_x is the angle between the $\hat{x}$ axis and the decay proton in the rest frame of the Λ. Similarly, θ_y and θ_z are the angles between the decay proton and the $\hat{y}$ and $\hat{z}$ axes respectively. Finally, θ_a is defined as the angle between the decay proton and the $\hat{\Lambda}$ axis in the rest frame of the Λ. The importance of these distributions will be explained in more detail in chapter 4.

In Figures 3.10, 3.11, 3.12, and 3.13 the difference between the Monte Carlo and reconstructed $\cos\theta$ are plotted on log plots. The Monte Carlo used had noise, inefficiencies and multiple scattering as described in section 3.9. The plots show that the program does extremely well at reconstructing these four cosines correctly. The bin size used in the analysis is 0.1 (20 bins ranging from -1.0 to 1.0), so a useful measure of the accuracy of the reconstruction can be seen in what percentage of the reconstructed events are within 0.1 of the Monte Carlo value for a given $\cos\theta$. In the case of $\cos\theta_x$ and $\cos\theta_y$, approximately 99.9% of the events are within 0.1 of the Monte Carlo value. For $\cos\theta_z$ approximately 99.8% satisfy this criteria. Finally, $\cos\theta_a$ is accurate to the 0.1 level 99.7% of the time. The full width at half maximum for all four of the comparison plots is 0.04, but it should be noted that the bin size for these plots is 0.02 and so the actual full widths may be smaller.

The second question can be answered by a look at a comparison of the $\cos\theta$ distributions for reconstructed Monte Carlo events and real events. Since not all Monte Carlo events will be accepted, the reconstructed Monte Carlo distributions need to be normalized to the number of real events. In Figures 3.14, 3.15, 3.16, and 3.17 the difference between the reconstructed Monte Carlo and the real data $\cos\theta$ distributions are plotted. Unlike the previous set of plots where comparisons were made on an event by event basis, these plots are comparisons between distributions containing a large number of events. These comparisons of normalized reconstructed Monte Carlo to real data for $\cos\theta_x$, $\cos\theta_y$, $\cos\theta_z$, and $\cos\theta_a$ show that the Monte Carlo follows the general trends as the data for acceptance as a function of $\cos\theta$. Note that the Monte Carlo was generated with the previous world average for α_{Ω^-}.

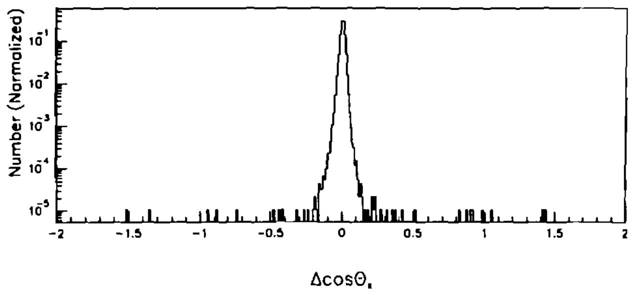

Figure 3.10: Normalized plot of the Ω^- Monte Carlo $\cos\theta_x$ minus the reconstructed Monte Carlo $\cos\theta_x$.

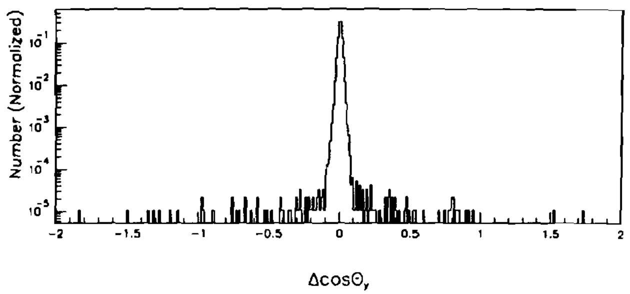

Figure 3.11: Normalized plot of the Ω^- Monte Carlo $\cos\theta_y$ minus the reconstructed Monte Carlo $\cos\theta_y$.

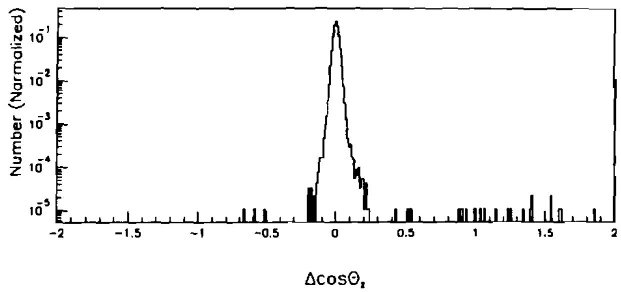

Figure 3.12: Normalized plot of the Ω^- Monte Carlo $\cos\theta_z$ minus the reconstructed Monte Carlo $\cos\theta_z$.

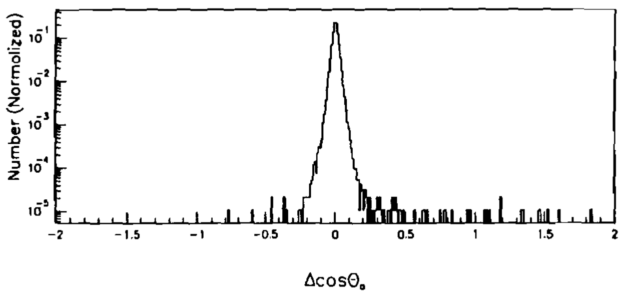

Figure 3.13: Normalized plot of the Ω^- Monte Carlo $\cos\theta_a$ minus the reconstructed Monte Carlo $\cos\theta_a$.

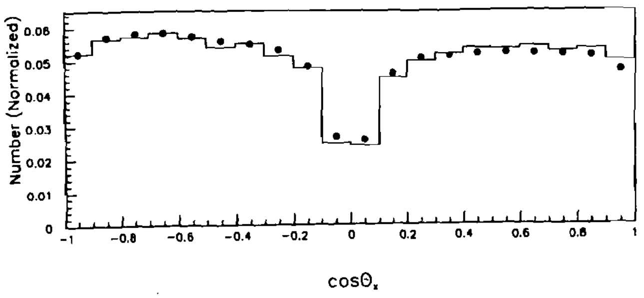

Figure 3.14: Comparison of the normalized reconstructed Monte Carlo $\cos\theta_x$ distribution to the real data $\cos\theta_x$ distribution for Ω^- events.

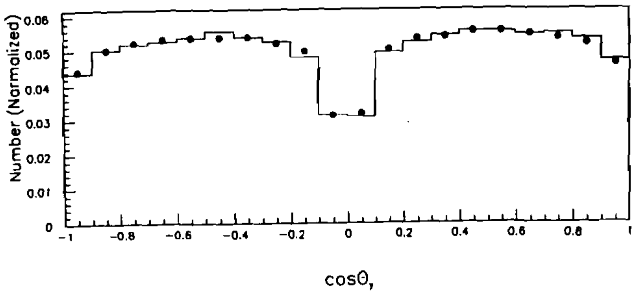

Figure 3.15: Comparison of the normalized reconstructed Monte Carlo $\cos\theta_y$ distribution to the real data $\cos\theta_y$ distribution for Ω^- events.

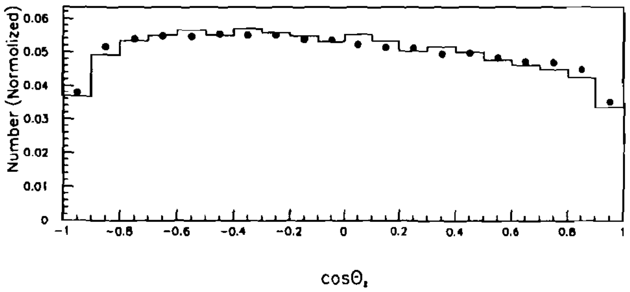

Figure 3.16: Comparison of the normalized reconstructed Monte Carlo $\cos\theta_z$ distribution to the real data $\cos\theta_z$ distribution for Ω^- events.

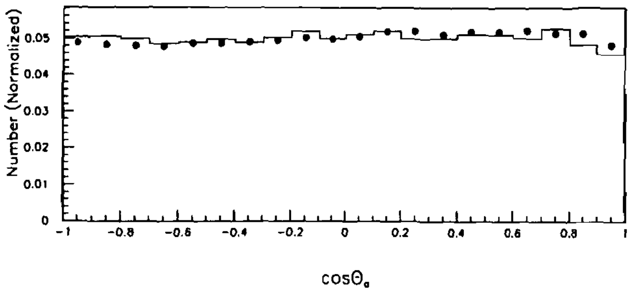

Figure 3.17: Comparison of the normalized reconstructed Monte Carlo $\cos\theta_a$ distribution to the real data $\cos\theta_a$ distribution for Ω^- events.

3.11 Comparison of Reconstructed Monte Carlo to Real Data

The Monte Carlo was used as a tool for understanding the reconstruction, but was not used as part of the analysis. For this purpose, the Monte Carlo did a good job of reproducing most of the effects seen in the real data. The plots for χ^2_G/DF and χ^2_K are shown in Figures 3.18 and 3.22. Notice that these distributions show a sharp discontinuity at 4.0 and 15.0 respectively. The reason these sharp edges appear is that these are the upper limits allowed for these values in the reconstruction. In the case of masses (m_{Ω^-} and m_{Ξ^-}) and the target positions (X_T and Y_T) shown in Figures 3.19, 3.20, 3.23, 3.24, there are both upper and lower limits set in the reconstruction for these values and that is why each of these plots has a discontinuity at both ends. The agreement between Monte Carlo and real data is very good but not perfect for these plots. The Ω^- mass for the data has longer tails than the Monte Carlo (not seen for the Ξ^-) which we attribute to the background which was not included in the Monte Carlo. In Figure 3.21 the decay vertices for the Ξ^- and its daughter Λ are given, while Figure 3.25 shows the decay verticies for the Ω^- and its daughter Λ. The spikes in these plots are artifacts of the reconstruction which tends to place vertices at the z position of an MWPC.

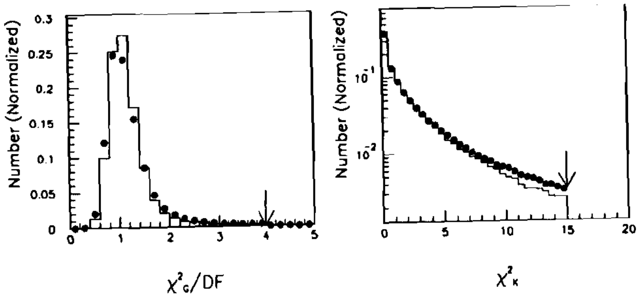

Figure 3.18: Comparison of the normalized χ^2_G/DF and χ^2_K distributions for Monte Carlo (solid line) and real data (circles) for Ξ^- events.

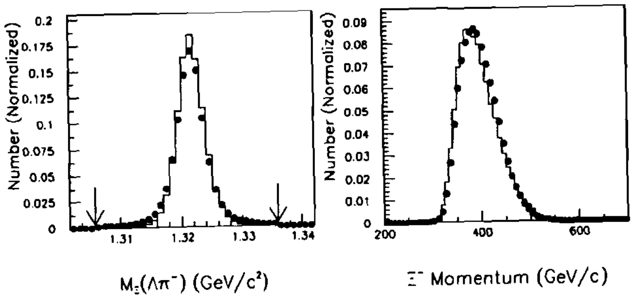

Figure 3.19: Comparison of the normalized m_{Ξ^-} mass and momentum distributions for Monte Carlo (solid line) and real data (circles) for Ξ^- events.

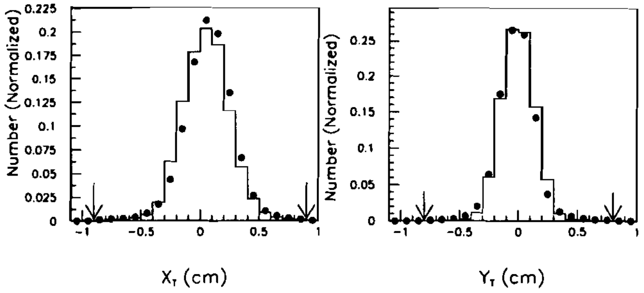

Figure 3.20: Comparison of the normalized x and y positions of Ξ^- events at the downstream target, X_T and Y_T, for Monte Carlo (solid line) and real data (circles).

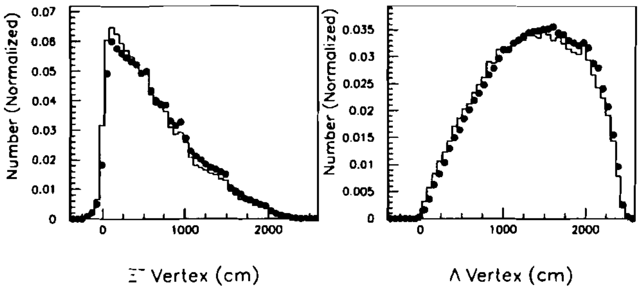

Figure 3.21: Comparison of the normalized Ξ^- and daughter Λ decay vertex distributions for Monte Carlo (solid line) and real data (circles).

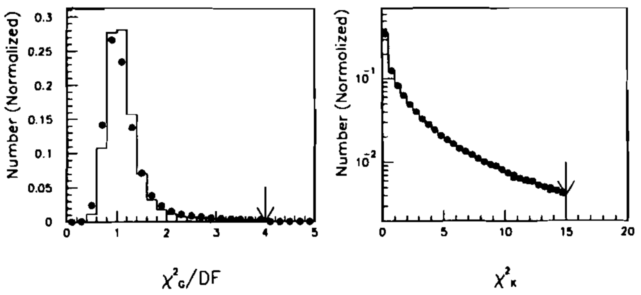

Figure 3.22: Comparison of the normalized χ^2_G/DF and χ^2_K distributions for Monte Carlo (solid line) and real data (circles) for Ω^- events.

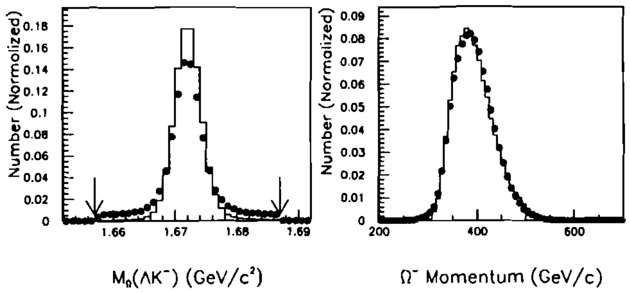

Figure 3.23: Comparison of the normalized m_{Ω^-} mass and momentum distributions for Monte Carlo (solid line) and real data (circles) for Ω^- events.

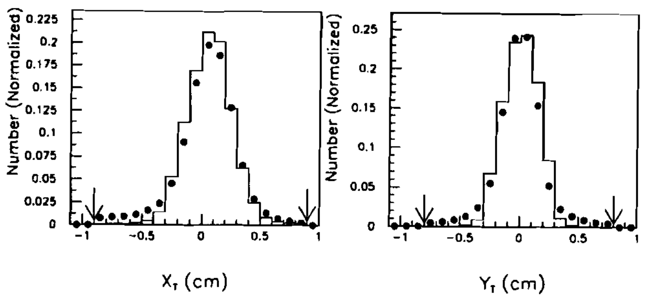

Figure 3.24: Comparison of the normalized x and y positions of Ω^- events at the downstream target, X_T and Y_T, for Monte Carlo (solid line) and real data (circles).

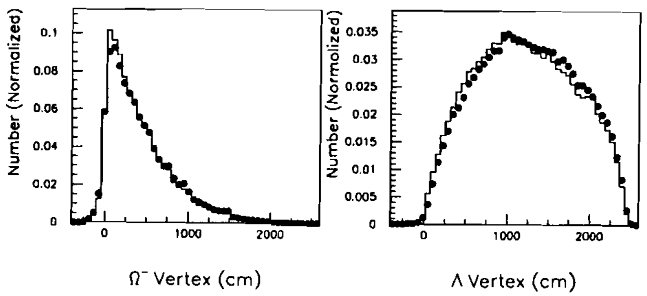

Figure 3.25: Comparison of the normalized Ω^- and daughter Λ decay vertex distributions for Monte Carlo (solid line) and real data (circles).

Chapter 4

The Analysis

4.1 Introduction

Measurements of the decay asymmetry parameters α, β, and γ involve the angular decay distribution projected onto the helicity frame axes (see Figures 4.1, 4.2, and 4.3 respectively). The helicity axes change on an event by event basis. In order to properly define the helicity axes it is necessary to know the direction of the parent baryon polarization. If this polarization direction is not explicitly known, then it can be measured by projecting the angular distribution onto a set of axes which are the same for all events. Usually, the set of axes used to measure polarization are defined parallel to the spectrometer axes.

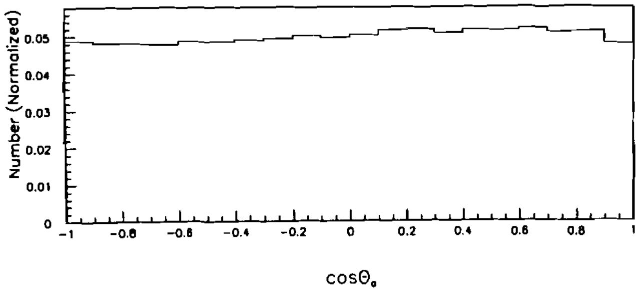

Figure 4.1: Normalized $\cos\theta_a$ distribution used in the measurement of $\alpha_\Lambda\alpha_{\Omega^-}$ for Ω^- events.

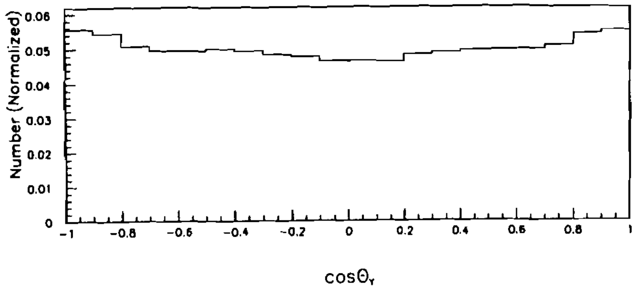

Figure 4.2: Normalized $\cos\theta_Y$ distribution used in the measurement of $\alpha_\Lambda\beta_{\Omega}-A_P$ for Ω^- events.

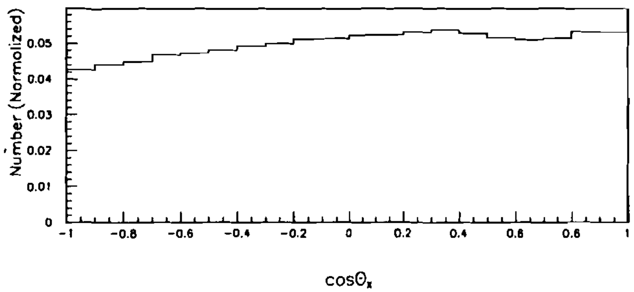

Figure 4.3: Normalized $\cos\theta_X$ distribution used in the measurement of $\alpha_\Lambda\gamma_{\Omega}-A_P$ for Ω^- events.

4.2 The Hybrid Monte Carlo

The acceptance of the combination of the spectrometer and the reconstruction program was not uniform for $\cos\theta_n$ from $-1.$ to $1.$ Any small dependence of the acceptance on $\cos\theta_n$ could alter the values of the asymmetry measurements since these were linearly dependent on $\cos\theta_n$. One way of accounting for the nonuniform acceptance was to compare the distributions for reconstructed real data to those from a large sample of reconstructed Monte Carlo events. There was one big drawback to this method. This drawback was the fact that the asymmetry measurements would become potentially sensitive to how well the Monte Carlo data simulated the real data.

Another way of correcting for nonuniform acceptance was a Hybrid Monte Carlo technique [24]. This was the method chosen to do the analysis. In this method a set of Monte Carlo events were generated for each real event, and these Monte Carlo events had many of the same parameters as the real event they were associated with.

For example, if the asymmetry angle being probed was one in the Λ rest frame and associated with the Λ decay, then the Hybrid Monte Carlo events had the same values for the momenta and decay vertices for the parent and the Λ as the real events. They also had the same value for the primary meson momenta, but different values for the momenta of the proton and pion.

The reason why certain parameters were shared by the Hybrid events and the real events had to do with the goal of the Hybrid Monte Carlo technique. The goal of this technique was to account for any nonuniform acceptance as a function of $\cos\theta_n$. To do this, the value for $\cos\theta_n$ for each Hybrid Monte Carlo event was randomly generated from a flat distribution. Since this angle described the direction of the daughter particles in the parent rest frame, the momenta of these daughter particles were in a different direction for the Hybrid events. Therefore, the daughter particle momenta when boosted into the lab frame differed from those for the real event. Any other parameters dependent on the momenta of the daughter particle were also altered. All of the other parameters remained the same as those for the real event.

Each real event was required to pass selection criteria to account for the apertures of the spectrometer including the trigger boundaries. There were also criteria based on reconstruction studies that required tracks to be well separated and fit at certain key chambers, taking into account the loss of hits due to dead or hot wires. These wire hits and separation criteria were based on Monte Carlo studies of the reconstruction and were designed to minimize effects due to the resolution of the spectrometer and reconstruction. By requiring events to fall in a region of uniform reconstruction efficiency, effects due to resolution were minimized. If a real event passed these selection criteria, then the generation of the Hybrid events began. Fake events were generated until either 30 of them passed the same selection criteria as the real events, or until a maximum number of attempts were tried. If the maximum of 300 attempts was exceeded without 30 Hybrid events passing all the selection criteria, the real event was removed from the sample. This situation occurred approximately 2.4% of the time. Thus, the resulting fake event sample experienced the same acceptance as the real data.

The full range $\cos\theta_n$, from $-1.$ to $1.$, was divided into 20 bins of width 0.1 each. All of the events were summed into these 20 bins, and these sums were kept separately for the real and Hybrid events. Even though the Hybrid events were generated from a flat distribution in $\cos\theta_n$, they were were not independent of the real events. Since the distribution for the real events was affected by their asymmetry, the Hybrid events were not independent of this asymmetry. To account for this coupling to the asymmetry of the real events, each Hybrid event had to be given a weighting factor. Each Hybrid event j with a $\cos\theta_{nij}$, associated with a real event i with $\cos\theta_{ni}$, was weighted by W_{ij}:

$$W_{ij} = \frac{1 + \alpha\vec{P}\cdot\hat{n}\cos\theta_{nij}}{1 + \alpha\vec{P}\cdot\hat{n}\cos\theta_{ni}} \tag{4.1}$$

where the asymmetry (α) and polarization ($\vec{P}$) were for the parent particle. The number of fake events in each bin was given by

$$n_f(k) = \sum_{ij} W_{ij} \tag{4.2}$$

for all fake events with $\cos\theta_{nij}$ in bin k. Let $n_r(k)$ be equal to the number of real events with $\cos\theta_{ni}$ in bin k, N_r and N_f be the total number of real and fake events respectively. With these definitions, the $\chi^2(k)$ for each bin was written as

$$\chi^2(k) = \frac{(n_r - n_f N_r/N_f)^2}{n_r} \tag{4.3}$$

with the total χ^2 equal to the sum over k of $\chi^2(k)$. A power series expansion for W_{ij}, and thus the χ^2, in terms $\alpha\vec{P}$, or any parameter in $\alpha\vec{P}$, can be performed. The χ^2 can be minimized by varying the expansion parameter. The best value for the parameter was determined to be the one which gave the lowest χ^2. The error on the parameter was found by varying the parameter about the point of minimum χ^2 until the χ^2 increased by 1.

4.3 The Preliminary Fit of $\alpha_\Lambda \alpha_{\Omega^-}$

The preliminary fit of $\alpha_\Lambda \alpha_{\Omega^-}$ assumed that the Hybrid Monte Carlo program correctly accounted for all sources of nonuniform acceptance. This fit also assumed that the polarization of the Ω^- sample was zero. In order to make a measurement of $\alpha_\Lambda \alpha_{\Omega^-}$ directly, it was necessary to look at the angular distribution of the daughter proton from the decay of the daughter Λ in the Λ rest frame. In the Λ rest frame, it was useful to define the unit vector $\hat{\Lambda} = -\hat{\Omega}^-$ (the opposite of the momentum direction of the parent Ω^-). With this definition, $\hat{\Lambda}$ in the Λ rest frame had the same spacial orientation as $\hat{\Lambda}$ in the Ω^- rest frame. In the Λ rest frame, $\alpha_\Lambda \alpha_{\Omega^-}$ was measured by analyzing the angular distribution of the daughter proton ($\hat{p}$) about this new axis $\hat{\Lambda}$ [7]. The angle of interest was equal to the dot product of the proton momentum direction and $\hat{\Lambda}$ ($\cos\theta_n = \hat{p}\cdot\hat{\Lambda}$). Using this definition of $\cos\theta_n$, the angular distribution of the daughter proton in this coordinate system was:

$$I(\theta_n) = \frac{1}{2}(1 + \alpha_\Lambda \alpha_\Xi \cos\theta_n) \tag{4.4}$$

and the slope of the angular distribution was equal to $\alpha_\Lambda \alpha_{\Omega^-}$.

The preliminary fit to $\alpha_\Lambda \alpha_{\Omega^-}$ used the Hybrid weight factor W_{ij}:

$$W_{ij} = \frac{1 + \alpha_\Lambda \alpha_{\Omega^-} \cos\theta_{nij}}{1 + \alpha_\Lambda \alpha_{\Omega^-} \cos\theta_{ni}} \tag{4.5}$$

The Taylor series expansion of W_{ij} was

$$\begin{aligned} W_{ij} &= 1 - (\cos\theta_{ni} - \cos\theta_{nij})(\alpha_\Lambda \alpha_{\Omega^-}) \\ &\quad + \cos\theta_{ni}(\cos\theta_{ni} - \cos\theta_{nij})(\alpha_\Lambda \alpha_{\Omega^-})^2 \\ &\quad - \cos\theta_{ni}^2(\cos\theta_{ni} - \cos\theta_{nij})(\alpha_\Lambda \alpha_{\Omega^-})^3 \ldots \end{aligned} \tag{4.6}$$

where only the first four terms were kept to perform the χ^2 minimization as a function of $\alpha_\Lambda \alpha_{\Omega^-}$.

4.4 The Fit of $\frac{\alpha_\Lambda}{2(j+1)}[1 + (2J+1)\gamma_{\Omega^-}]P_{\Omega^-}$

To make a measurement of $\frac{\alpha_\Lambda}{2(j+1)}[1 + (2J+1)\gamma_{\Omega^-}]P_{\Omega^-}$ it was once again necessary to look at the angular distribution of the daughter proton from the decay of the daughter Λ in the Λ rest frame. This time however, the $\hat{n}$ axis was chosen to be parallel to one of the lab axes $\hat{x}$, $\hat{y}$, or $\hat{z}$. This analysis was repeated for each of the three orthogonal axes.

Once again, the Hybrid Monte Carlo technique was used to fit the asymmetry. The Hybrid weight factor used for this part of the analysis was:

$$W_{ij} = \frac{1 + \frac{\alpha_\Lambda}{2(j+1)}[1 + (2J+1)\gamma_{\Omega^-}]P_{\Omega^-} \cos\theta_{nij}}{1 + \frac{\alpha_\Lambda}{2(j+1)}[1 + (2J+1)\gamma_{\Omega^-}]P_{\Omega^-} \cos\theta_{ni}} \tag{4.7}$$

The Taylor series expansion in $\frac{\alpha_\Lambda}{2(j+1)}[1 + (2J+1)\gamma_{\Omega^-}]P_{\Omega^-}$ for this form of W_{ij} was:

$$\begin{aligned} W_{ij} &= 1 - (\cos\theta_{ni} - \cos\theta_{nij})(\frac{\alpha_\Lambda}{2(j+1)}[1 + (2J+1)\gamma_{\Omega^-}]P_{\Omega^-}) \\ &\quad + \cos\theta_{ni}(\cos\theta_{ni} - \cos\theta_{nij})(\frac{\alpha_\Lambda}{2(j+1)}[1 + (2J+1)\gamma_{\Omega^-}]P_{\Omega^-})^2 \\ &\quad - \cos\theta_{ni}^2(\cos\theta_{ni} - \cos\theta_{nij})(\frac{\alpha_\Lambda}{2(j+1)}[1 + (2J+1)\gamma_{\Omega^-}]P_{\Omega^-})^3 \ldots \end{aligned} \tag{4.8}$$

Once again only the first four terms were kept to do the χ^2 minimization. However, this time the χ^2 was minimized as a function of $\frac{\alpha_\Lambda}{2(j+1)}[1 + (2J+1)\gamma_{\Omega^-}]P_{\Omega^-}$.

4.4.1 Bias Cancelation in the Polarization Fit

The measurement of the asymmetry $\frac{\alpha_\Lambda}{2(j+1)}[1 + (2J+1)\gamma_{\Omega^-}]P_{\Omega^-}$ assumed that all reconstruction and spectrometer acceptances were accounted for. If there were any unknown acceptance problems, then the measurement would be the sum of a real polarization signal and a fake signal generated by the unknown acceptance problems. Since this fake signal, or bias, was an artifact of the reconstruction program and the spectrometer, it should not experience a sign change if the production angle was reversed. A real polarization signal, on the other hand, would have a sign change if the production angle was reversed. Because of this, the polarization and bias could be separated [25, 8, 16, 17, 26]. Let A_+ be the measured asymmetry at a positive production angle, and A_- be the asymmetry for a negative production angle. In this scheme, the asymmetries could be written as:

$$\begin{aligned} A_{n+} &= B_n + \frac{\alpha_\Lambda}{2(j+1)}[1+(2J+1)\gamma_{\Omega^-}]P_{\Omega^-} \\ A_{n-} &= B_n - \frac{\alpha_\Lambda}{2(j+1)}[1+(2J+1)\gamma_{\Omega^-}]P_{\Omega^-} \end{aligned} \tag{4.9}$$

where B_n is the bias term. With these definitions, the polarization could be found by taking the difference between the two asymmetries. These definitions could also be used to find the bias by summing the two asymmetries.

$$\begin{aligned} \frac{\alpha_\Lambda}{2(j+1)}[1+(2J+1)\gamma_{\Omega^-}]P_{\Omega^-} &= \frac{A_{n+} - A_{n-}}{2} \\ B_n &= \frac{A_{n+} + A_{n-}}{2} \end{aligned} \tag{4.10}$$

4.5 The Second Stage Fit of $\alpha_\Lambda\alpha_{\Omega^-}$

The preliminary fit to $\alpha_\Lambda\alpha_{\Omega^-}$ assumed that the polarization of the Ω^-s was zero. Also, any bias seen in the polarization measurement could effect the $\alpha_\Lambda\alpha_{\Omega^-}$ asymmetry. From equations 4.9, it can be seen that the asymmetry term measured could be written as the sum of a real asymmetry and a bias term.

$$\alpha\vec{P}_{meas}\cdot\hat{n} = \alpha\vec{P}_{real}\cdot\hat{n} + \vec{B}\cdot\hat{n} \tag{4.11}$$

Therefore, for the second stage fit of $\alpha_\Lambda\alpha_{\Omega^-}$ it was important to account for any nonzero biases. The weight factor for this fit was:

$$W_{ij} = \frac{1+(\alpha_\Lambda\alpha_{\Omega^-} + \vec{B}_\Lambda\cdot\hat{\Lambda})\cos\theta_{nij}}{1+(\alpha_\Lambda\alpha_{\Omega^-} + \vec{B}_\Lambda\cdot\hat{\Lambda})\cos\theta_{ni}} \tag{4.12}$$

The Taylor series expansion for this weight function in $\alpha_\Lambda\alpha_{\Omega^-}$ was found to be:

$$\begin{aligned} W_{ij} &= \frac{1+\vec{B}_\Lambda\cdot\hat{\Lambda}\cos\theta_{nij}}{1+\vec{B}_\Lambda\cdot\hat{\Lambda}\cos\theta_{ni}} - \left[\frac{\cos\theta_{ni}-\cos\theta_{nij}}{(1+\vec{B}_\Lambda\cdot\hat{\Lambda}\cos\theta_{ni})^2}\right](\alpha_\Lambda\alpha_{\Omega^-}) \\ &+ \left[\frac{\cos\theta_{ni}(\cos\theta_{ni}-\cos\theta_{nij})}{(1+\vec{B}_\Lambda\cdot\hat{\Lambda}\cos\theta_{ni})^3}\right](\alpha_\Lambda\alpha_{\Omega^-})^2 \\ &- \left[\frac{\cos\theta_{ni}^2(\cos\theta_{ni}-\cos\theta_{nij})}{(1+\vec{B}_\Lambda\cdot\hat{\Lambda}\cos\theta_{ni})^4}\right](\alpha_\Lambda\alpha_{\Omega^-})^3\ldots \end{aligned} \tag{4.13}$$

As before, the first four terms of this expansion were kept and the Hybrid Monte Carlo technique was performed to measure the asymmetry with the bias correction included.

4.6 The Fit of the β and γ projections

The projections necessary for measuring the β/γ ratio required that the parent polarization be known so that the helicity axes could be defined for both the spin-$\frac{1}{2}$ and spin-$\frac{3}{2}$ cases. Also, apart from some minor constant differences, and the t_{30} tensor polarization term, the projections for the two spin cases are basically the same. In addition, $(P_\Omega - \frac{5}{16}\sqrt{\frac{7}{5}}t_{30})$ will behave in a similar way to the polarization term in the spin-$\frac{1}{2}$ case. Therefore, for this analysis the two spin cases can be treated the same. Let A_P be defined as:

$$A_P = \left\{ \begin{array}{cc} \frac{\pi}{4}P_\Xi & \text{, if } J = \frac{1}{2} \\ \frac{3\pi}{10}(P_\Omega - \frac{5}{16}\sqrt{\frac{7}{5}}t_{30}) & \text{, if } J = \frac{3}{2} \end{array} \right\}$$

In the Λ rest frame, $\alpha_\Lambda\beta A_P$ and $\alpha_\Lambda\gamma A_P$ were measured by analyzing the angular distribution of the daughter proton ($\hat{p}$) about the helicity axes $\hat{Y}$ and $\hat{X}$ (defined in section 1.2.1) respectively. The angle of interest was equal to the dot product of the proton momentum direction and the appropriate helicity axis ($\cos\theta_Y = \hat{p}\cdot\hat{Y}$ for β and $\cos\theta_X = \hat{p}\cdot\hat{X}$ for γ). Using these definitions of $\cos\theta$, the angular distribution projections of the daughter proton in this coordinate system were:

$$\begin{aligned} I(\theta_Y) &= \frac{1}{2}(1+\alpha_\Lambda\beta A_P\cos\theta_Y) \\ I(\theta_X) &= \frac{1}{2}(1-\alpha_\Lambda\gamma A_P\cos\theta_X) \end{aligned} \tag{4.14}$$

and the slopes of these angular distributions were $\alpha_\Lambda \beta A_P$ and $-\alpha_\Lambda \gamma A_P$ respectively.

The $\alpha_\Lambda \beta A_P$ fit used the Hybrid weight factor W_{ij}:

$$W_{ij} = \frac{1 + \alpha_\Lambda \beta A_P \cos\theta_{ij}}{1 + \alpha_\Lambda \beta A_P \cos\theta_i} \tag{4.15}$$

The hybrid weighting factor W_{ij} can be expanded in a Taylor series:

$$\begin{aligned} W_{ij} &= 1 - (\cos\theta_i - \cos\theta_{ij})(\alpha_\Lambda \beta A_P) \\ &\quad + \cos\theta_i(\cos\theta_i - \cos\theta_{ij})(\alpha_\Lambda \beta A_P)^2 \\ &\quad - \cos\theta_i^2(\cos\theta_i - \cos\theta_{ij})(\alpha_\Lambda \beta A_P)^3 \ldots \end{aligned} \tag{4.16}$$

once again only the first four terms were kept for the χ^2 minimization as a function of $\alpha_\Lambda \beta A_P$. The same procedure was performed for the $\alpha_\Lambda \gamma A_P$ fit. The hybrid weighting factor for this asymmetry had the same form as in the β asymmetry measurement, and can be deduced from equation 4.16 by replacing all occurrences of β by γ.

As in the polarization case, the asymmetries here could be a combination of bias and signal. The asymmetries are:

$$\begin{aligned} A_{Y+} &= B_Y + \alpha_\Lambda \beta A_P \\ A_{Y-} &= B_Y - \alpha_\Lambda \beta A_P \\ A_{X+} &= B_X - \alpha_\Lambda \gamma A_P \\ A_{X-} &= B_X + \alpha_\Lambda \gamma A_P \end{aligned} \tag{4.17}$$

Notice the sign difference between the β and γ equations. This sign difference arises because the hybrid weighting factor for the γ projection did not include the minus sign shown in equation 4.14. These definitions can be used to find the signals and the biases in the same manner as was done for the polarization. The results are:

$$\begin{aligned} \alpha_\Lambda \beta A_P &= \frac{A_{Y+} - A_{Y-}}{2} \\ B_Y &= \frac{A_{Y+} + A_{Y-}}{2} \end{aligned}$$

$$\begin{aligned} -\alpha_\Lambda \gamma A_P &= \frac{A_{X+} - A_{X-}}{2} \\ B_X &= \frac{A_{X+} + A_{X-}}{2} \end{aligned} \tag{4.18}$$

The two asymmetry signals measured are $\alpha_\Lambda \beta A_P$ and $-\alpha_\Lambda \gamma A_P$, and so the ratio of these two signals gives $-\beta/\gamma$.

Chapter 5

Results and Systematic Uncertainty Studies

5.1 Results

The data listed in Table 3.7 was analyzed as described in the previous chapter for $\alpha_\Lambda \alpha_{\Omega^-}$ and ϕ_{Ω^-}. The value of α_{Ω^-} was then determined using the world average value for α_Λ listed in Table 1.1. The data was divided up into sets according to the various run conditions and analyzed separately to better study the systematics. Each of these various sets are listed in Table 5.1 along with a short reference name.

All four data sets were used to measure the $\alpha_\Lambda \alpha_{\Omega^-}$ asymmetry. In order to do a full analysis of the $\alpha_\Lambda \alpha_{\Omega^-}$ asymmetry it was necessary to first measure the biases for all four data sets. Once the biases were determined, they were used to perform the final fit of the asymmetry. There were several potential sources of systematic uncertainties in the measurement (see section 5.2). A study of these potential systematic uncertainties indicated no evidence of a significant systematic error. The result for this measurement was

Name	Description			Events
	Production Mode	Angle (mrad)	Current (amps)	
N2900	Neutral	±1.8	-2900	166300
N750	Neutral	±1.8	-750	50000
X2900	Spin Transfer	±1.8	-2900	18300
Z2900	Neutral	±0.0	-2900	17400

Table 5.1: The names and descriptions of the data sets analyzed.

$$\alpha_\Lambda \alpha_{\Omega^-} = 0.0126 \pm 0.0042$$
$$\alpha_{\Omega^-} = 0.0196 \pm 0.0066$$

In order to measure the $\beta_\Omega/\gamma_\Omega$ angle ϕ_{Ω^-}, it is necessary to have a polarized sample of Ω^- particles. While it is not as important for this measurement to know the magnitude of the polarization, it is necessary to have an accurate determination of its direction. The polarization of the Ω^- is linearly proportional to the polarization of its daughter Λ baryon (see equation 1.16). The relationship between these two polarizations is not independent of γ_{Ω^-}. Since the magnitude of γ_{Ω^-} is close to 1.,

$$P_{\Omega^-} \cong P_\Lambda \quad , \text{ if } \gamma_{\Omega^-} \cong 1.$$
$$P_{\Omega^-} \cong -\tfrac{5}{3} P_\Lambda \quad , \text{ if } \gamma_{\Omega^-} \cong -1.$$

This sign flip will cause both asymmetries to flip signs, and thus has no effect on the ratio. Therefore, it is not necessary to know the sign of γ_{Ω^-} to perform the measurement of ϕ_{Ω^-}. It will be assumed in the following analysis that γ_{Ω^-} is positive as predicted by theory.

The goal of the experiment was to measure the magnetic moment of the Ω^- by measuring the precession of the polarization in a magnetic field. Because of the precession of the polarization, a good determination of the x and z components of the polarization was required (parity conservation in the strong interaction requires that the y component be zero). Only the N2900 data set had enough statistics due to the small polarization, on order of 4% to 6% [27, 28], to measure both the x and z components accurately. Both the N750 data set and the X2900 data set had polarization signals less than 3 sigma from zero (2.5 and 2.6 sigma respectively) and so it was unclear if it was really polarized based on these signals alone. Since this measurement involves the ratio of two signals which are defined only for the case of nonzero polarization, it is important to have a clear indication of polarization in the data used. Additional evidence that these sets were probably polarized came from studies of the Ω^- magnetic moment measurement [27]. Therefore, the N2900 data set (which showed a polarization signal 5.8 sigma from zero) along with the N750 and X2900 data sets were used in the final determination of ϕ_{Ω^-}. The N750 and the X2900 data sets also proved useful in studying the systematics involved for this measurement (see section 5.3). The measurement showed no signs of a significant systematic error. The angle for the ratio of $\beta_\Omega/\gamma_\Omega$ was measured to be

$$\phi_{\Omega^-} = -3.4° \pm 10.3°$$

5.2 Systematic Studies for the Measurement of $\alpha_\Lambda\alpha_{\Omega^-}$

All four of the data sets were used in the measurement of $\alpha_\Lambda\alpha_{\Omega^-}$. The data were used to study this asymmetry as a function of momentum, Hybrid Monte Carlo seed value, uncertainty in the bias values, run type, time, and selection criteria.

For this asymmetry measurement it was desired to have an unpolarized Ω^- data sample to eliminate any possible systematic errors due to polarization. A polarization signal could effect the signal in a similar manner as the biases (see section 5.2.3). Since the polarization of a sample reverses sign when the production angle is reversed, an unpolarized Ω^- sample can be obtained by mixing equal amounts of opposite production angle data together. Also, data taken at a production angle of zero has to be unpolarized in order to satisfy parity in the strong interaction. Therefore, roughly equal samples of data taken at opposite production angles were added to the sample of data taken at a production angle of zero and analyzed for this asymmetry measurement. The residual polarization in the total sample was estimated to be a factor of 0.017 times the polarization of the polarized sample. Since the polarized sample had a polarization of roughly 0.05, the residual polarization was calculated to be 0.0008. The estimated maximum effect this level of a signal would have on the asymmetry was less than 0.0001 and thus deemed negligible.

There were a couple of potential sources of systematic error in this measurement. The maximum contributions to the overall systematic error are listed in Table 5.2. The differences in the signal due to selection criteria and bias were 0.31 sigma and 0.17 sigma respectively. These differences were considered consistent with statistical uncertainties and thus were not deemed to represent a systematic error. The error estimated from the seed value study was at a smaller level, but indicated a real limit to the accuracy of the measurement technique. The error can be reduced by trying many more seed values, although the limit is already negligible compared to the overall statistical error. A close study of the time dependence indicated changes in signal were consistent with statistical fluctuations. No evidence of a systematic error was found for this measurement.

5.2.1 Momentum Study for the Measurement of $\alpha_\Lambda\alpha_{\Omega^-}$

The largest data set was the N2900 sample. Because of the higher statistics the data set could be divided into 4 bins as a function of Ω^- momentum. Any sign of a dependence on momentum would be an indication of a systematic problem. The measured value of

Study	Estimated Maximum Systematic Error
Momentum	0.0000
Seed Value	0.0002
Bias Uncertainty	0.0007
Run Type	0.0000
Criteria	0.0013
Time	0.0019

Table 5.2: The estimated maximum contributions to the total systematic error for the measurement of $\alpha_\Lambda \alpha_{\Omega^-}$.

Momentum (GeV/c)	Before Bias Correction		After Bias Correction	
	$\alpha_\Lambda \alpha_{\Omega^-}$	χ^2	$\alpha_\Lambda \alpha_{\Omega^-}$	χ^2
348.	-0.0017 ± 0.0102	19	0.0004 ± 0.0103	19
380.	0.0107 ± 0.0095	21	0.0130 ± 0.0095	21
403.	0.0183 ± 0.0100	14	0.0228 ± 0.0100	14
439.	-0.0011 ± 0.0095	21	0.0068 ± 0.0095	21

Table 5.3: Measured asymmetry $\alpha_\Lambda \alpha_{\Omega^-}$ before and after bias correction for the N2900 data set as a function of momentum. There were 19 degrees of freedom in the fit.

$\alpha_\Lambda \alpha_{\Omega^-}$ as a function of momentum for both before and after the bias correction analysis is listed in Table 5.3 and plotted in Figure 5.1. The chi-squared per degree of freedom for a fit to a single value was 0.90 for the four bias corrected values in Table 5.3. A least squares fit to a line was also tried. The slope from this fit was 0.0027 ± 0.0043, consistent with zero to better than 0.63 sigma. The chi-squared per degree of freedom for the line fit was 1.23. No systematic error due to momentum was found.

Momentum (GeV/c)	Bias x	Bias y	Bias z
348.	-0.0073 ± 0.0092	0.0166 ± 0.0097	0.0202 ± 0.0115
380.	0.0133 ± 0.0084	0.0372 ± 0.0094	0.0370 ± 0.0101
403.	0.0009 ± 0.0090	-0.0028 ± 0.0099	0.0560 ± 0.0104
439.	0.0148 ± 0.0086	0.0119 ± 0.0090	0.0730 ± 0.0100

Table 5.4: The biases used in the momentum study of $\alpha_\Lambda \alpha_{\Omega^-}$ for the N2900 data set.

5.2.2 Seed Value Dependence Study for the Measurement of $\alpha_\Lambda \alpha_{\Omega^-}$

The analysis was rerun 10 times using different seed values for the Hybrid Monte Carlo event generation. The average value of these 10 analyses was calculated, and the systematic error was determined to be 0.0002. This error was estimated by

$$\frac{\sigma_n}{\sqrt{nseed}} \tag{5.1}$$

where nseed is the number of different seed values tried, and σ_n is the sigma for the distribution of differences from the average for the seed values. The average value was 0.0126 ± 0.0042. The 10 runs are listed in Table 5.5 for both before and after bias correction. The after bias correction results are shown in Figure 5.2.

5.2.3 Bias Uncertainty Study for the Measurement of $\alpha_\Lambda \alpha_{\Omega^-}$

The biases were measured quantities which had significant uncertainties in them. In order to estimate the systematic error due to the uncertainties in the biases, each of the biases were alternately changed by 1.0 sigma. The difference in the measured asymmetry for each of these changes is listed in Table 5.6. No change was observed when the y biases were altered. The asymmetry showed a slight change when the x biases were altered, and a larger change for the z biases. The maximum error due to uncertainties in the biases was estimated to be 0.0007. No significant systematic error was found.

	Before Bias Correction		After Bias Correction	
Run	$\alpha_\Lambda \alpha_{\Omega^-}$	χ^2	$\alpha_\Lambda \alpha_{\Omega^-}$	χ^2
1	0.0099 ± 0.0041	11	0.0129 ± 0.0042	11
2	0.0105 ± 0.0041	15	0.0134 ± 0.0042	16
3	0.0090 ± 0.0041	15	0.0120 ± 0.0041	15
4	0.0103 ± 0.0042	12	0.0132 ± 0.0042	12
5	0.0092 ± 0.0049	13	0.0121 ± 0.0042	13
6	0.0091 ± 0.0041	10	0.0121 ± 0.0042	10
7	0.0089 ± 0.0041	14	0.0118 ± 0.0041	14
8	0.0107 ± 0.0041	13	0.0136 ± 0.0042	13
9	0.0097 ± 0.0041	14	0.0126 ± 0.0042	14
10	0.0095 ± 0.0041	14	0.0125 ± 0.0041	14

Table 5.5: Measured asymmetry $\alpha_\Lambda \alpha_{\Omega^-}$ before and after bias correction for different seed values in the Hybrid Monte Carlo analysis. There were 19 degrees of freedom in the fit.

Bias	$\Delta \alpha_\Lambda \alpha_{\Omega^-}$
$B_x = B_x + \sigma_{B_x}$	-0.0001
$B_x = B_x - \sigma_{B_x}$	0.0001
$B_y = B_y + \sigma_{B_y}$	0.0000
$B_y = B_y - \sigma_{B_y}$	0.0000
$B_z = B_z + \sigma_{B_z}$	0.0005
$B_z = B_z - \sigma_{B_z}$	-0.0006

Table 5.6: The change in $\alpha_\Lambda \alpha_{\Omega^-}$ as the biases are altered within uncertainties for the entire data set. B_n is the n-axis bias

---

Set	Momentum (GeV/c)	Events	Before Bias Correction		After Bias Correction	
			$\alpha_\Lambda \alpha_{\Omega^-}$	χ^2	$\alpha_\Lambda \alpha_{\Omega^-}$	χ^2
N2900	394.	166294	0.0074 ± 0.0049	16	0.0113 ± 0.0049	16
N750	304.	49984	0.0183 ± 0.0099	23	0.0179 ± 0.0099	23
X2900	393.	18264	0.0203 ± 0.0149	12	0.0231 ± 0.0149	12
Z2900	398.	17427	0.0023 ± 0.0152	11	0.0053 ± 0.0152	11

Table 5.7: Measured asymmetry $\alpha_\Lambda \alpha_{\Omega^-}$ before and after bias correction for the four data sets. There were 19 degrees of freedom in the fit.

Set	Bias x	Bias y	Bias z
N2900	0.0049 ± 0.0044	0.0161 ± 0.0074	0.0488 ± 0.0053
N750	-0.0068 ± 0.0083	0.0291 ± 0.0094	-0.0034 ± 0.0109
X2900	0.0098 ± 0.0132	-0.0062 ± 0.0143	0.0417 ± 0.0154
Z2900	-0.0029 ± 0.0136	-0.0043 ± 0.0147	0.0423 ± 0.0162

Table 5.8: The biases used in the fit for the asymmetry $\alpha_\Lambda \alpha_{\Omega^-}$ for the run type study.

5.2.4 Run Type Study for the Measurement of $\alpha_\Lambda \alpha_{\Omega^-}$

The four data sets were analyzed separately as an additional systematic check for the $\alpha_\Lambda \alpha_{\Omega^-}$ asymmetry measurement. Table 5.7 lists the asymmetry before and after bias correction for the four data sets. The biases used for each data set are listed in Table 5.8. No significant dependence was observed. Figure 5.3 shows the asymmetry as a function of run type.

5.2.5 Selection Criteria Study for the Measurement of $\alpha_\Lambda \alpha_{\Omega^-}$

The measurement was studied by varying some of the selection criteria. One of these tests was to tighten the Ω^- mass requirements. The default upper and lower mass limits were 1.657 GeV/c^2 and 1.687 GeV/c^2 respectively. The tighter limits used were 1.6645 GeV/c^2 and 1.6795 GeV/c^2. The tighter limits reduced the estimated background from

3.0% to 1.5% and thus provided a good indication of systematics due to background events. Analysis with the tighter mass limits yielded a value of 0.0120 ± 0.0043 and indicated a maximum systematic error of 0.0006. Even doubling this error would give agreement to within 0.3 sigma. Thus, it was determined that background events were not a significant problem.

An additional test was performed using tighter chi-squared requirements. In this test $\chi^2_G \leq 3.0$ and $\chi^2_K \leq 10.$ were required. The asymmetry was found to be 0.0113 ± 0.0043 for the tighter chi-squared criteria. The estimated potential systematic error was 0.0013. The maximum contribution to the systematic error was estimated to be 0.0013. This test showed agreement at the 0.3 sigma level. No evidence of a significant dependence on the selection criteria was found.

5.2.6 Time Dependence Study for the Measurement of $\alpha_\Lambda\alpha_{\Omega^-}$

The N2900 data sample was also studied as a function of time. The other 3 data sets were too small to study as a function of time, but could be considered as individual points in a time dependence study. The N2900 data set was divided into 3 subsets based on when the data was taken. Subset 1 indicates earliest N2900 data taken and subset 3 was the last N2900 data taken. The measured values of $\alpha_\Lambda\alpha_{\Omega^-}$ for the 3 subsets are listed in Table 5.9, while the biases used are in Table 5.10. There is a possible time dependent signal for the N2900 data set (see Figure 5.4). The two early subsets are in very good agreement, but the first subset differs from the last by 2.7 sigma. The chi-squared per degree of freedom for a fit of these three subsets was 2.50.

The overall data sample does not show this large of a time dependence and there does not appear to be any trend in the values as a function of time. The X2900 sample was taken between the first and second subset. The N750 was taken after the third subset and the Z2900 was the last data set collected. The asymmetry as a function of time for the whole data sample is shown in Figure 5.5.

Subset	Before Bias Correction		After Bias Correction	
	$\alpha_\Lambda\alpha_{\Omega^-}$	χ^2	$\alpha_\Lambda\alpha_{\Omega^-}$	χ^2
1	-0.0036 ± 0.0089	29	-0.0002 ± 0.0089	29
2	-0.0015 ± 0.0090	15	0.0032 ± 0.0090	15
3	0.0204 ± 0.0078	17	0.0238 ± 0.0078	17

Table 5.9: Measured asymmetry $\alpha_\Lambda\alpha_{\Omega^-}$ before and after bias correction for the N2900 data set as a function of time. There were 19 degrees of freedom in the fit.

To better study the possibility of a time dependent systematic problem, a large sample of Ξ^- events were analyzed for the asymmetry $\alpha_\Lambda\alpha_{\Xi^-}$. The decay mode $\Xi^- \rightarrow \Lambda\pi^-$, the dominant decay mode, has the same topology as the decay $\Omega^- \rightarrow \Lambda K^-$. Therefore, a time dependence problem should show up in the measurement of $\alpha_\Lambda\alpha_{\Xi^-}$ if it exists in the measurement of $\alpha_\Lambda\alpha_{\Omega^-}$. The asymmetry result for 1,300,000 Ξ^-s taken during the same time period as subset 2 of the Ω^-s, was compared to the result for 1,200,000 Ξ^-s taken during the time period of subset 3. These two results agreed to within 1 sigma (0.0019), and yielded a chi-squared of 0.52 for a fit to a single value. No time dependence was found in the $\alpha_\Lambda\alpha_{\Xi^-}$ measurement down to a level of 0.0019. Other diagnostics of the data such as momentum distributions and vertex distributions exhibited no differences in the two time frames. We concluded that the behavior of $\alpha_\Lambda\alpha_{\Omega^-}$ was consistent with a statistical fluctuation and do not ascribe any systematic error to it. The maximum contribution to the systematic error for the measurement of $\alpha_\Lambda\alpha_{\Omega^-}$ was estimated to be 0.0019, much smaller than the statistical error. No evidence was found to indicate any time dependence existed, which indicated that the signal experienced a statistical fluctuation.

Subset	Bias x	Bias y	Bias z
1	0.0044 ± 0.0080	-0.0010 ± 0.0087	0.0426 ± 0.0096
2	0.0039 ± 0.0081	0.0223 ± 0.0088	0.0620 ± 0.0097
3	0.0075 ± 0.0070	0.0195 ± 0.0075	0.0430 ± 0.0083

Table 5.10: The biases used in the time study of $\alpha_\Lambda\alpha_{\Omega^-}$ for the N2900 data set.

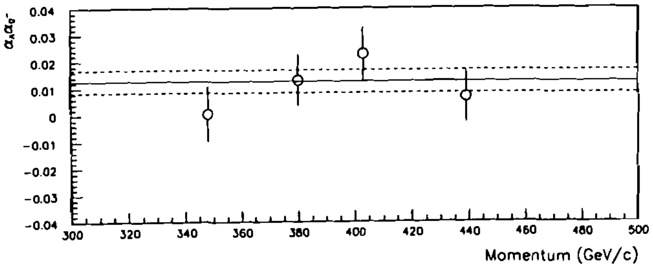

Figure 5.1: The asymmetry $\alpha_\Lambda\alpha_{\Omega^-}$ after bias correction for the N2900 data set as a function of momentum. The solid line and dashed lines represent the measurement and its errors respectively.

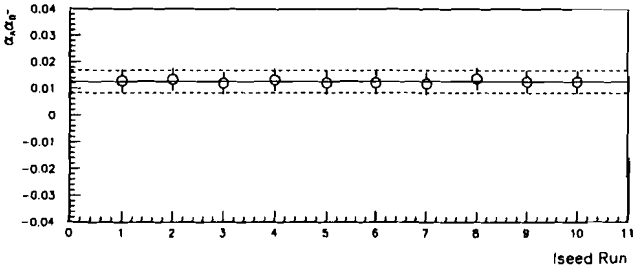

Figure 5.2: The asymmetry $\alpha_\Lambda\alpha_{\Omega^-}$ after bias correction for the different Hybrid seed values. The solid line and dashed lines represent the measurement and its errors respectively.

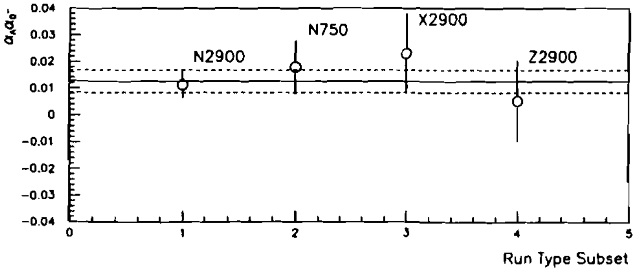

Figure 5.3: The asymmetry $\alpha_\Lambda\alpha_{\Omega^-}$ after bias correction as a function of run type. The solid line and dashed lines represent the measurement and its errors respectively.

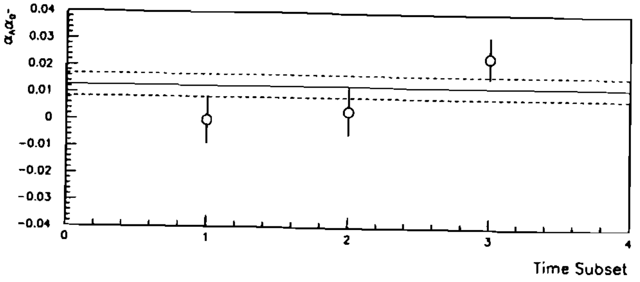

Figure 5.4: The asymmetry $\alpha_\Lambda\alpha_{\Omega^-}$ after bias correction for the 3 subsets of the N2900 data set as a function of time. The solid line and dashed lines represent the measurement and its errors respectively.

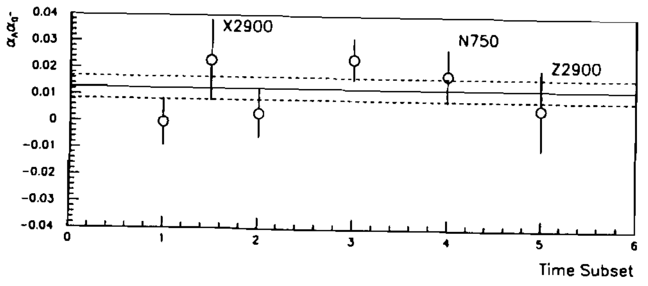

Figure 5.5: The asymmetry $\alpha_\Lambda\alpha_{\Omega^-}$ after bias correction for the 3 subsets of the N2900 data set, the N750 data set, the X2900 data set and the Z2900 data set as a function of time. The solid line and dashed lines represent the measurement and its errors respectively.

Set	$\alpha_\Lambda P_{\Lambda x}$	$\alpha_\Lambda P_{\Lambda y}$	$\alpha_\Lambda P_{\Lambda z}$
N2900	0.0184 ± 0.0044	0.0074 ± 0.0048	0.0210 ± 0.0053
N750	0.0179 ± 0.0083	0.0067 ± 0.00934	0.0171 ± 0.0109
X2900	-0.0236 ± 0.0132	0.0079 ± 0.0143	-0.0339 ± 0.0159

Table 5.11: The average polarization components for P_Λ

5.3 Systematic Studies for the Measurement of ϕ_{Ω^-}

The only one of the data sets with enough statistics to perform a good measurement of ϕ_{Ω^-} was the N2900 set. The N750 and the X2900 sets did not have enough statistics to allow an independent determination of the polarization direction, or a clear indication that the sets were polarized. There was, however, enough evidence to indicate that the N750 and the X2900 samples probably were polarized and so they were included in the final result. It should be noted that including these two sets had only a small effect on the overall answer. The x, y, and z components of the polarization were determined using the bias cancelation method which also yielded the biases used in the $\alpha_\Lambda\alpha_{\Omega^-}$ analysis. The polarization signals for these three data sets are listed in Table 5.11 [27, 28]. Note that the y component for all three sets is expected to be zero because of parity conservation in the strong interaction. The measured values for the y polarization are consistent with this prediction. Therefore, it will be assumed that there is no polarization along $\hat{y}$ for this analysis.

The final determination of the polarization was made using the fact that the polarization precessed in a magnetic field. This method used the Ω^- magnetic moment as a constraint and thus was more accurate than using the values from Table 5.11 (see section 5.3.1).

The N2900 data set was used to study this asymmetry as a function of momentum and Hybrid Monte Carlo seed value. The N750 and the X2900 data sets were used

Study	Estimated Maximum Systematic Error
Momentum	0.0°
Seed Value	0.9°
Run Type	0.0°
Criteria	1.7°
Polarization Direction	2.2°

Table 5.12: The estimated contributions to the total systematic error for the measurement of ϕ_{Ω^-}.

to study any possible run condition dependence using an external constraint on the polarization direction for these samples. The potential contributions of the various studies to the overall systematic error are listed in Table 5.12. The seed value error was estimated to be very small compared to the statistical error and therefore can be considered negligible. No evidence for any momentum or run type dependence was found. No significant systematic error due to the selection criteria was found. The largest potential systematic error was due to the determination of the polarization direction. The polarization direction was varied within errors and the results agreed to within 0.17 sigma. The measurement showed no evidence of a significant systematic error.

5.3.1 Determination of the polarization direction for the Measurement of ϕ_{Ω^-}

The N750 and the X2900 data sets did not have enough statistics to allow an accurate determination of the polarization direction. The error involved in determining the polarization direction for these two sets can be removed by using the measured value of the Ω^- magnetic moment to unfold the polarization direction under the assumption that the polarization precessed through the magnetic field. It was also assumed that the initial direction of the polarization was perpendicular to the production plane as required by parity conservation in the strong interaction. The precession angle can be written as [8, 29]

Set	μ_{Ω^-} (n.m.)	Field Integral (Tm)	$\hat{P}_x$	$\hat{P}_s$
N2900	-2.01	-24.36	0.662	0.749
N750	-2.01	-17.48	0.821	0.571
X2900	-2.01	-24.36	-0.662	-0.749

Table 5.13: The Ω^- magnetic moment, field integrals and the polarization direction components calculated from them.

$$\phi_{precession} = \frac{e}{\beta m_\Omega c^2}\left[\frac{\mu_\Omega}{2J}\frac{m_\Omega}{m_p} + 1\right] BDL \tag{5.2}$$

where BDL is the field integral. The precession angle is linearly dependent on the product of the magnetic moment and the field integral. Therefore, using the known values of the field integral for these sets, the polarization direction error is related to the error in the magnetic moment. The field integrals, Ω^- magnetic moment (μ_{Ω^-}) [27], and the calculated components of the polarization direction are listed in Table 5.13. Note that the polarization for the X2900 set had the opposite sign of the polarization in the N2900 set. The N2900 data sample dominated the measurement of the magnetic moment, and so the error in the polarization direction for the N750 and the X2900 sets is the same as that of the N2900 set.

5.3.2 Momentum Study for the Measurement of ϕ_{Ω^-}

The N2900 set was divided up as a function of momentum into four bins to search for a possible momentum dependence. The polarization direction did not have to be measured as a function of momentum because a precession of the polarization in the magnetic field is independent of momentum when measured with respect to the momentum

Momentum (GeV/c)	Events	$\alpha_\Lambda\beta_{\Omega^-}A_P$	Bias	χ^2 p n
349.	42452	-0.0083 ± 0.0096	0.0021 ± 0.0096	20 20
380.	42484	0.0085 ± 0.0095	0.0095 ± 0.0095	12 14
403.	37322	0.0102 ± 0.0101	-0.0176 ± 0.0101	18 18
442.	44360	-0.0028 ± 0.0095	-0.0008 ± 0.0095	20 27

Momentum (GeV/c)	Events	$\alpha_\Lambda\gamma_{\Omega^-}A_P$	Bias	χ^2 p n
349.	42581	-0.0324 ± 0.0114	-0.0146 ± 0.0114	18 28
380.	42400	-0.0236 ± 0.0097	-0.0310 ± 0.0097	19 25
403.	37199	-0.0304 ± 0.0101	-0.0430 ± 0.0101	15 19
442.	44186	-0.0097 ± 0.0099	-0.0423 ± 0.0099	20 20

Table 5.14: Measured asymmetries $\alpha_\Lambda\beta_{\Omega^-}A_P$ and $\alpha_\Lambda\gamma_{\Omega^-}A_P$ using bias cancelation for the N2900 data set as a function of momentum. There were 19 degrees of freedom in the fit.

direction [30, 19]. Therefore, the direction determined for the polarization measured for the entire N2900 data set was used for each momentum bin (see Table 5.13).

The required independence of momentum for the polarization direction made this study possible. In Table 5.14 the asymmetries measured for $\alpha_\Lambda\beta_{\Omega^-}A_P$ and $\alpha_\Lambda\gamma_{\Omega^-}A_P$ using the bias cancelation technique are listed. The measured value of ϕ_{Ω^-} for each of the momentum bins is listed in Table 5.15. Plots of the asymmetries and the angle ϕ_{Ω^-} are shown in Figures 5.6–5.8. The four measurements are consistent with zero. As an additional check, a chi-squared fit was performed using the four measurements and yielded a chi-squared per degree of freedom of 0.70 (2.11 for 3 degrees of freedom). No evidence of a momentum dependence was found.

5.3.3 Seed Value Dependence Study for the Measurement of ϕ_{Ω^-}

As was done for the measurement of $\alpha_\Lambda\alpha_{\Omega^-}$, the analysis was rerun 10 times using different seed values for the Hybrid Monte Carlo event generation (see Figures 5.9–5.11). Table 5.13 lists the components of the direction of the Ω^- polarization used in this study. The average value for ϕ_{Ω^-} was calculated in two different ways. In the first method the average of the ϕ_{Ω^-} values in Table 5.17 was calculated. The second method required that the averages for the two asymmetries be calculated for the values in Table 5.16. These average asymmetries were then used to calculate a new average for ϕ_{Ω^-}. The second method was more logical since the angle was calculated using these measured asymmetries. The averages for the two asymmetries were

Momentum (GeV/c)	ϕ_{Ω^-}
349.	-14.4° ± 19.5°
380.	19.8° ± 22.2°
403.	18.5° ± 18.0°
442.	-16.1° ± 56.2°

Table 5.15: Measured ratio ϕ_{Ω^-} for the N2900 sample as a function of Ω^- momentum.

$$\alpha_\Lambda\beta_{\Omega^-}A_P = 0.0001 \pm 0.0048$$

$$\alpha_\Lambda\gamma_{\Omega^-}A_P = -0.0236 \pm 0.0052$$

and yielded a value of 0.3° ± 12.6° for ϕ_{Ω^-} (note that this value was calculated from the two averages before they were rounded off). The error was estimated in the same way as in the $\alpha_\Lambda\alpha_{\Omega^-}$ measurement using equation 5.1. This test showed that a systematic limit of 0.9° existed in the measurement. The two methods agreed to within 0.02° and so did not contribute to the systematic error.

5.3.4 Run Type Study for the Measurement of ϕ_{Ω^-}

The N750 and the X2900 data sets were not large enough to make a good measurement of the necessary asymmetries. However, these two sets were useful in studying the systematics of the measurement. The calculated components of the polarization direction are listed in Table 5.13. The asymmetries and ϕ_{Ω^-} for the three data sets using this

Run	$\alpha_\Lambda\beta_{\Omega^-}A_P$	Bias	χ^2
			p n
1	0.0013 ± 0.0048	-0.0009 ± 0.0048	7 20
2	-0.0003 ± 0.0048	-0.0012 ± 0.0048	6 22
3	0.0017 ± 0.0048	-0.0007 ± 0.0048	9 23
4	0.0006 ± 0.0048	-0.0016 ± 0.0048	7 24
5	-0.0003 ± 0.0048	-0.0015 ± 0.0048	7 25
6	-0.0004 ± 0.0048	-0.0006 ± 0.0048	7 24
7	-0.0013 ± 0.0048	-0.0014 ± 0.0048	6 21
8	-0.0003 ± 0.0048	-0.0024 ± 0.0048	7 24
9	-0.0005 ± 0.0048	0.0012 ± 0.0048	6 20
10	0.0007 ± 0.0048	0.0002 ± 0.0048	8 21

Run	$\alpha_\Lambda\gamma_{\Omega^-}A_P$	Bias	χ^2
			p n
1	-0.0236 ± 0.0052	-0.0357 ± 0.0052	16 25
2	-0.0247 ± 0.0052	-0.0334 ± 0.0052	16 22
3	-0.0231 ± 0.0052	-0.0338 ± 0.0052	14 28
4	-0.0233 ± 0.0052	-0.0350 ± 0.0052	18 23
5	-0.0241 ± 0.0052	-0.0344 ± 0.0052	15 22
6	-0.0237 ± 0.0052	-0.0345 ± 0.0052	14 24
7	-0.0232 ± 0.0052	-0.0339 ± 0.0052	17 27
8	-0.0225 ± 0.0052	-0.0354 ± 0.0052	15 24
9	-0.0249 ± 0.0052	-0.0346 ± 0.0052	18 26
10	-0.0231 ± 0.0052	-0.0339 ± 0.0052	14 24

Table 5.16: The N2900 data set asymmetries $\alpha_\Lambda\beta_{\Omega^-}A_P$ and $\alpha_\Lambda\gamma_{\Omega^-}A_P$ for different seed values in the Hybrid Monte Carlo analysis. There were 19 degrees of freedom in the fit.

Run	ϕ_{Ω^-}
1	3.2° ± 12.6°
2	-0.7° ± 12.1°
3	4.2° ± 12.9°
4	1.5° ± 12.8°
5	-0.7° ± 12.4°
6	-1.0° ± 12.6°
7	-3.2° ± 12.8°
8	-0.7° ± 13.2°
9	-1.2° ± 12.0°
10	1.7° ± 12.9°

Table 5.17: Measured ratio ϕ_{Ω^-} for the N2900 sample for different seed values in the Hybrid Monte Carlo analysis.

technique are listed in Tables 5.18 and 5.19 respectively. Figures 5.12–5.14 show plots of the asymmetries and the angle for the different run types. The angles measured this way are consistent among the three data sets and so no systematic error was found.

5.3.5 Selection Criteria Study for the Measurement of ϕ_{Ω^-}

Once again, some of the selection criteria were varied to look for a dependence on the selection criteria. The main test involved tightening the Ω^- mass requirements (see section 5.2.5), and showed agreement to within 1.7°. This indicated that background events did not create a significant problem for the measurement. As in section 5.2.5, the chi-squared requirements were also varied. The signal agreed to within 0.8° for the tighter chi-squared requirements. The maximum systematic error from these tests was estimated to be 1.7°, much smaller than the statistical error. Therefore, no significant systematic error was indicated by these tests.

Set	Momentum (GeV/c)	Events	$\alpha_\Lambda \beta_{\Omega^-} A_P$	Bias	χ^2 p n
N2900	394.	166300	0.0001 ± 0.0048	-0.0009 ± 0.0048	7 22
N750	304.	50000	-0.0078 ± 0.0102	-0.0122 ± 0.0102	22 9
X2900	393.	18300	-0.0006 ± 0.0152	0.0163 ± 0.0152	10 29

Set	Momentum (GeV/c)	Events	$\alpha_\Lambda \gamma_{\Omega^-} A_P$	Bias	χ^2 p n
N2900	394.	166300	-0.0236 ± 0.0052	-0.0345 ± 0.0052	16 24
N750	304.	50000	-0.0247 ± 0.0105	0.0056 ± 0.0105	30 16
X2900	393.	18300	-0.0323 ± 0.0159	0.0447 ± 0.0159	10 12

Table 5.18: Measured asymmetries $\alpha_\Lambda \beta_{\Omega^-} A_P$ and $\alpha_\Lambda \gamma_{\Omega^-} A_P$ using bias cancelation for the N750 and the X2900 data sets. There were 19 degrees of freedom in the fit.

Set	ϕ_{Ω^-}
N2900	0.3° ± 12.6°
N750	-17.6° ± 23.2°
X2900	-1.1° ± 28.2°

Table 5.19: Measured ratio ϕ_{Ω^-} for the N2900 sample for the N750 and the X2900 data sets.

5.3.6 Study of Polarization Direction Uncertainty for ϕ_{Ω^-}

There were two different tests done to see how stable the measurement was when the polarization vector was allowed to vary within one sigma. The first method was to use the direction determined by the polarization asymmetry measurements without constraining the Ω^- magnetic moment. The analysis was repeated for different seed values and yielded an average value of -1.4° ± 12.5°. This corresponds to a difference in signal of 1.7° which is small compared to the overall statistical error.

The second method was to run the analysis several times with the polarization direction determined by altering the Ω^- magnetic moment by ±1 sigma. This study indicated a potential systematic limit of 2.2°. This study showed agreement at the 0.17 sigma level and so did not indicate a significant systematic error.

5.3.7 Study of the Measurement of ϕ_{Ξ^-}

An additional test was performed using a subset of the Ξ^- spin transfer data which showed a large polarization of over 12%. The combination of both large statistics and large polarization allowed for a fairly good determination of the polarization direction of the Ξ^- particles. An analysis of the polarization using the bias cancelation technique showed $| \alpha_\Lambda \gamma_{\Xi^-} P_{\Xi^-} | = 0.07425 \pm 0.00417$ (where P_{Ξ^-} is the Cascade Minus polarization). Using this value and the fact that

$$\alpha_\Lambda \gamma_{\Xi^-} A_P = -\frac{\pi}{4} \alpha_\Lambda \gamma_{\Xi^-} P_{\Xi^-}$$

the asymmetry is predicted to have a value of -0.0583. The measured value of -0.0589 ± 0.0044 (see Table 5.20) agrees with the prediction to within 0.14 sigma. This test demonstrated that the correct axes to make the ϕ measurement could be determined. Determination of this axis required that the other two helicity axes be determined first.

Momentum (GeV/c)	Events	$\alpha_\Lambda\beta_{\Xi}$-$A_P$	Bias	χ^2 p n
396.	195536	-0.0074 ± 0.0046	-0.0048 ± 0.0046	29 46

Momentum (GeV/c)	Events	$\alpha_\Lambda\gamma_{\Xi}$-$A_P$	Bias	χ^2 p n
396.	196336	-0.0589 ± 0.0044	-0.0101 ± 0.0044	25 34

Table 5.20: Measured asymmetries $\alpha_\Lambda\beta_{\Xi}$-$A_P$ and $\alpha_\Lambda\gamma_{\Xi}$-$A_P$ using bias cancelation. There were 19 degrees of freedom in the fit.

Using the two asymmetries from Table 5.20 yields

$$\phi_{\Xi^-} = -7.2^\circ \pm 4.2^\circ$$

which is close to zero as expected. The world average was 4° ± 4° [23]. Both of these values are consistent with zero. Although the two are 2.7 sigma apart, the world average represents 9 measurements. A fit of this measurement with the 9 previous ones yields a value of -2.2° ± 3.1° with a chi-squared per degree of freedom of 1.19 (there were 9 degrees of freedom).

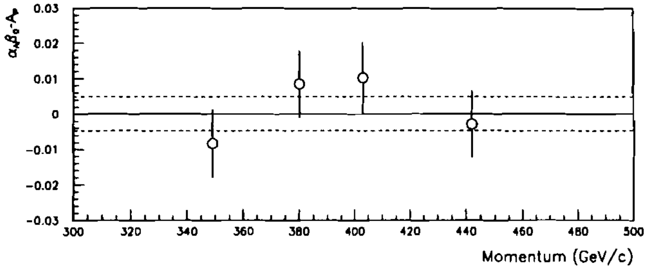

Figure 5.6: The asymmetry $\alpha_\Lambda\beta_\Omega$-$A_P$ after bias cancelation for the N2900 data set as a function of momentum. The solid line and dashed lines represent the measurement and its errors respectively.

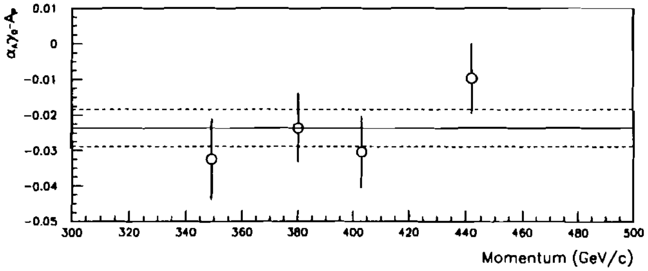

Figure 5.7: The asymmetry $\alpha_\Lambda\gamma_\Omega$-$A_P$ after bias cancelation for the N2900 data set as a function of momentum. The solid line and dashed lines represent the measurement and its errors respectively.

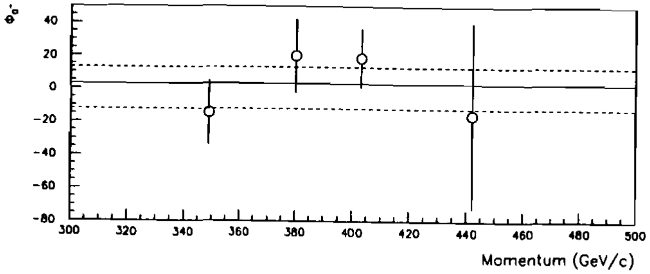

Figure 5.8: The angle ϕ_{Ω^-} for the N2900 data set as a function of momentum. The solid line and dashed lines represent the measurement and its errors respectively.

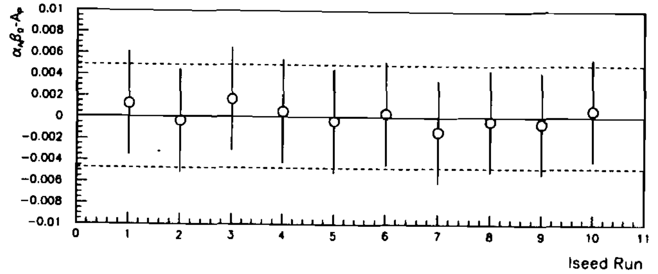

Figure 5.9: The asymmetry $\alpha_\Lambda\beta_{\Omega^-}$-$A_P$ after bias cancelation for the different Hybrid seed values. The solid line and dashed lines represent the measurement and its errors respectively.

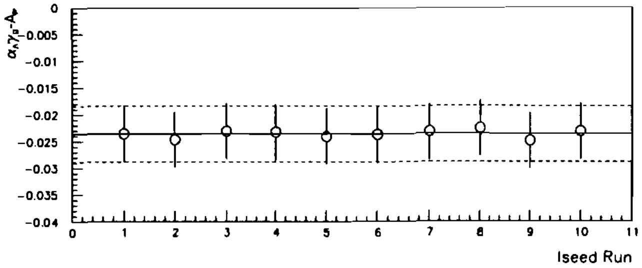

Figure 5.10: The asymmetry $\alpha_\Lambda\gamma_{\Omega^-}$-$A_P$ after bias cancelation for the different Hybrid seed values. The solid line and dashed lines represent the measurement and its errors respectively.

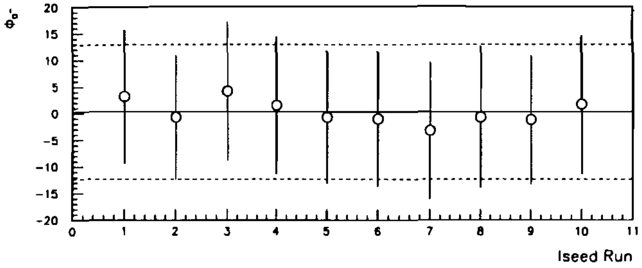

Figure 5.11: The asymmetry ϕ_{Ω^-} after bias cancelation for the different Hybrid seed values. The solid line and dashed lines represent the measurement and its errors respectively.

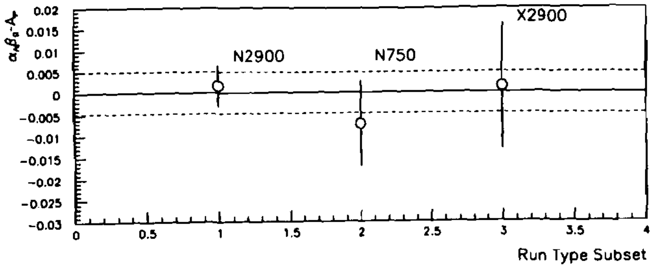

Figure 5.12: The asymmetry $\alpha_\Lambda\beta_{\Omega^-}A_P$ after bias cancelation as a function of run type. The solid line and dashed lines represent the measurement and its errors respectively.

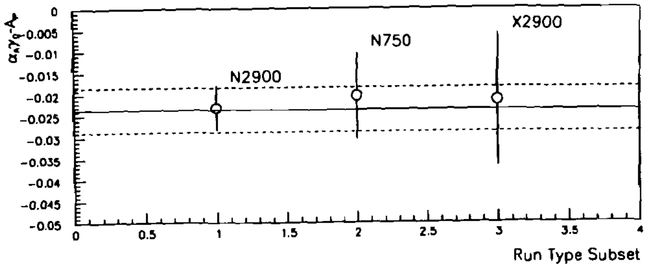

Figure 5.13: The asymmetry $\alpha_\Lambda\gamma_{\Omega^-}A_P$ after bias cancelation as a function of run type. The solid line and dashed lines represent the measurement and its errors respectively.

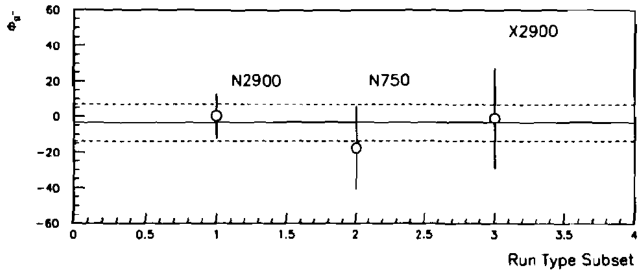

Figure 5.14: The angle ϕ_{Ω^-} as a function of run type. The solid line and dashed lines represent the measurement and its errors respectively.

5.4 Study of Measuring the Sign of γ_{Ω^-}

The sign of γ_{Ω^-} can be measured using the angular distribution defined in equation 1.18. The resulting equation is

$$t_{30} = \frac{16}{5}\sqrt{\frac{5}{7}}\left[\frac{5\,|\,\alpha_\Lambda P_\Lambda\,|}{\alpha_\Lambda\,|\,1+4\gamma_{\Omega^-}\,|} + \frac{(\alpha_\Lambda\gamma_{\Omega^-}A_P)\,10}{\alpha_\Lambda\gamma_{\Omega^-}\;\;3\pi}\right] \tag{5.3}$$

The main problem is that unlike in the spin-$\frac{1}{2}$ case (see equation 1.13), there is the additional term t_{30} (a tensor polarization term) that adds an extra parameter to the equation. Since both α_{Ω^-} and ϕ_{Ω^-} have been measured, the magnitude of γ_{Ω^-} can be determined because of the normalization condition satisfied by the three asymmetry parameters. Using this magnitude a measurement of t_{30} can be made for both signs of γ_{Ω^-} to see if one of the cases can be ruled out. Note that the measured quantities used as input are α_Λ, $\alpha_\Lambda P_\Lambda$, $\alpha_\Lambda\beta_{\Omega^-}A_P$, $\alpha_\Lambda\gamma_{\Omega^-}A_P$, and $\alpha_\Lambda\alpha_{\Omega^-}$ (see section 4.6 for a definition of A_P). The values required for this test are listed in Tables 5.21-5.23. The Ω^-

Input Values	
α_Λ	0.642 ± 0.013
$\alpha_\Lambda P_\Lambda$	0.0279 ± 0.0049
$\alpha_\Lambda \alpha_{\Omega^-}$	0.0126 ± 0.0042
$\alpha_\Lambda \beta_{\Omega^-} A_P$	0.0001 ± 0.0048
$\alpha_\Lambda \gamma_{\Omega^-} A_P$	-0.0236 ± 0.0052

Table 5.21: The input values used in calculating t_{30} for the N2900 sample.

polarization, P_{Ω^-} was related to the measured Λ polarization, P_Λ, using equation 1.16. The γ_{Ω^-} term in equation 5.3 can be rewritten as

$$\gamma_{\Omega^-} = \sqrt{\frac{1 - ((\alpha_\Lambda \alpha_{\Omega^-})/\alpha_\Lambda)^2}{1 + ((\alpha_\Lambda \beta_{\Omega^-} A_P)/(\alpha_\Lambda \gamma_{\Omega^-} A_P))^2}} \tag{5.4}$$

which is important for the proper propagation of errors.

This technique requires that theory can place some limits on the value of t_{30} and that there is enough polarization and statistics. Using the Thomas Precession Model of DeGrand and Miettinen [31] the prediction for t_{30} is zero in the neutral production mode [22]. The value of t_{30} measured under both cases is listed in Table 5.24 for the three samples. The combined result was

$$t_{30} = 0.008 \pm 0.022 \quad , \text{ if } \gamma_{\Omega^-} \cong 1.$$

$$t_{30} = 0.090 \pm 0.033 \quad , \text{ if } \gamma_{\Omega^-} \cong -1.$$

Both of these values are consistent with zero and each other. Therefore, the sign of γ_{Ω^-} could not be determined in this experiment, although the positive sign is favored.

Input Values	
α_Λ	0.642 ± 0.013
$\alpha_\Lambda P_\Lambda$	0.0234 ± 0.0090
$\alpha_\Lambda \alpha_{\Omega^-}$	0.0126 ± 0.0042
$\alpha_\Lambda \beta_{\Omega^-} A_P$	-0.0078 ± 0.0102
$\alpha_\Lambda \gamma_{\Omega^-} A_P$	-0.0247 ± 0.0105

Table 5.22: The input values used in calculating t_{30} for the N750 sample.

Input Values	
α_Λ	0.642 ± 0.013
$\alpha_\Lambda P_\Lambda$	0.0407 ± 0.0147
$\alpha_\Lambda \alpha_{\Omega^-}$	0.0126 ± 0.0042
$\alpha_\Lambda \beta_{\Omega^-} A_P$	-0.0006 ± 0.0152
$\alpha_\Lambda \gamma_{\Omega^-} A_P$	-0.0323 ± 0.0159

Table 5.23: The input values used in calculating t_{30} for the X2900 sample. Note that a positive value for $\alpha_\Lambda P_\Lambda$ is listed since the β and γ measurements were made in a coordinate system which assumed a positive polarization.

Set	γ_{Ω^-}	t_{30}
N2900	≅ 1.	0.012 ± 0.026
N2900	≅ -1.	0.090 ± 0.038
N750	≅ 1.	-0.013 ± 0.050
N750	≅ -1.	0.059 ± 0.091
X2900	≅ 1.	0.027 ± 0.077
X2900	≅ -1.	0.141 ± 0.113

Table 5.24: The value of t_{30} under both sign hypotheses for the N2900, N750 and X2900 samples.

Chapter 6

Conclusions

Measurements of the weak decay parameters provide an important probe of our understanding of quark decay processes. The Ω^- hyperon provides a good opportunity to probe quark decay processes in a spin-$\frac{3}{2}$ system. The $\Omega^- \rightarrow \Lambda K^-$ decay is assumed to have two amplitudes, a parity conserving amplitude and a parity violating amplitude (B and C respectively). Theory predicts that the C amplitude is kinematically suppressed with respect to the B amplitude by a factor of approximately 0.08. The decay is also expected to satisfy time reversal invariance.

The asymmetry parameter α_{Ω^-} for the decay $\Omega^- \rightarrow \Lambda K^-$ has been measured to be

$$\alpha_\Lambda \alpha_{\Omega^-} = 0.0126 \pm 0.0042$$
$$\alpha_{\Omega^-} = 0.0196 \pm 0.0066$$

The new measurement is roughly a factor of 3.9 more precise than the previous world average of -0.026 ± 0.026 [23]. This new measurement is consistent with a small or zero value for α_{Ω^-} as predicted by theory.

The ratio of $\beta_{\Omega^-}/\gamma_{\Omega^-}$, which is usually referred to as the angle

$$\phi_{\Omega^-} = \tan^{-1}(\beta_{\Omega^-}/\gamma_{\Omega^-}),$$

is an important test of time reversal invariance. Neglecting final state interactions, time reversal invariance predicts ϕ_{Ω^-} is zero. If final state interactions are included, at most a small nonzero value would be allowed. A large value for this ratio would be an indication of time reversal violation. This measurement gives

$$\phi_{\Omega^-} = -3.4^\circ \pm 10.3^\circ$$

which is consistent with zero and time reversal invariance.

The sign of γ_{Ω^-} indicates which decay amplitude is dominant. If γ_{Ω^-} is positive, the B amplitude is larger than the C amplitude. If γ_{Ω^-} is negative, the C amplitude is dominant. The sign of γ_{Ω^-} can be determined by measuring the value of the tensor polarization t_{30} under the assumption of each sign of γ_{Ω^-}. Using the angular distribution defined in equation 1.18 this measurement gave

$$t_{30} = 0.008 \pm 0.022 \quad , \text{ if } \gamma_{\Omega^-} \cong 1.$$
$$t_{30} = 0.090 \pm 0.033 \quad , \text{ if } \gamma_{\Omega^-} \cong -1.$$

The theoretical prediction is that $t_{30} = 0$. While the former is slightly more consistent with zero, the later cannot be completely ruled out. The measurement favors the positive sign for γ_{Ω^-} which is consistent with theory.

Using these measurements, the B and C amplitudes can be determined if two assumptions are made. The first assumption is that time reversal invariance holds. The second assumption is that γ_{Ω^-} is positive. Both assumptions are consistent with the measurements of this experiment, and the B and C amplitudes are found to be

$$B = 5.60 \times 10^{-7} \pm 0.05 \times 10^{-7}$$
$$C = 0.58 \times 10^{-7} \pm 0.24 \times 10^{-7}$$
$$C/B = 0.10 \pm 0.04$$

The ratio of these two amplitudes is in good agreement with the kinematic suppression factor of 0.08. The measured ratio of amplitudes also agrees well with the previous world average of 0.14 ± 0.14. The individual amplitudes also agree well with the previous world averages of $5.60 \times 10^{-7} \pm 0.05 \times 10^{-7}$ and $0.78 \times 10^{-7} \pm 0.78 \times 10^{-7}$ for the B and C amplitudes respectively. This measurement represents more than a factor of 3 improvement over the world averages for the C amplitude and the ratio C/B.

Referring back to Tables 1.1, 1.2, 1.3 it can be seen that these measurements of the Ω^- weak decay parameters makes the Ω^- decay as well measured as the other hyperons. It is now a challenge for theory.

Appendix A

Derivations of the Vector Polarization and Angular Distributions

A.1 Introduction

An analysis of the weak decay angular distributions will be presented, which is equally valid for anti-hyperons as well as hyperons, following a formalism introduced by Byers and Fenster [32]. Their formalism has been used by K. B. Luk to derive formulas for measuring the vector polarization and the α parameter for a spin-J fermion [33]. The analysis below will closely parallel the work of K. B. Luk and will also be extended to derive formulas for determining β and γ for a spin-$\frac{3}{2}$ fermion. The formalism will also be used to treat the more familiar case of a $J = \frac{1}{2}$ fermion for completeness.

There are two sets of coordinate axes that are important in the analysis of the angular distributions of weak decays. Both systems are defined in the rest frame of the parent particle. The S frame is an event independent coordinate system with axes parallel to the lab axes. The S' system is an event dependent coordinate helicity frame (see section 1.2.1). The three helicity axes are defined as:

$$\hat{\Lambda}, \quad \hat{Y} = \frac{\hat{P} \times \hat{\Lambda}}{|\hat{P} \times \hat{\Lambda}|}, \quad \hat{X} = \frac{\hat{Y} \times \hat{\Lambda}}{|\hat{Y} \times \hat{\Lambda}|}. \tag{A.1}$$

The helicity axes can be expanded in two different bases which prove useful in the analysis to follow. The first basis is the spherical coordinate system. Here the helicity axes can be written as:

$$\begin{aligned}
\hat{\Lambda} &= (\sin\theta_\Lambda \cos\phi_\Lambda, \sin\theta_\Lambda \sin\phi_\Lambda, \cos\theta_\Lambda) \\
\hat{X} &= (\cos\theta_\Lambda \cos\phi_\Lambda, \cos\theta_\Lambda \sin\phi_\Lambda, -\sin\theta_\Lambda) \\
\hat{Y} &= (-\sin\phi_\Lambda, \cos\phi_\Lambda, 0).
\end{aligned}$$

The second basis is composed of spherical harmonics and rotation matrices. The first basis is useful in visualizing the coordinate system since it is the more familiar one. The second basis helps to simplify the algebra involved in the calculations. In terms of this second basis, the helicity frame axes are:

$$\begin{aligned}
\hat{X} &= (\frac{1}{2}(D^{1*}_{11} - D^{1*}_{-11} + D^{1}_{11} - D^{1}_{-11}), \frac{i}{2}(D^{1}_{11} - D^{1*}_{11} + D^{1}_{-11} - D^{1*}_{-11}), -\sqrt{2}D^{1}_{01}) \\
\hat{Y} &= (\frac{i}{2}(D^{1*}_{11} - D^{1}_{11} + D^{1}_{-11} - D^{1*}_{-11}), \frac{1}{2}(D^{1}_{11} + D^{1*}_{11} + D^{1}_{-11} + D^{1*}_{-11}), 0) \\
\hat{\Lambda} &= (\frac{1}{2}\sqrt{\frac{8\pi}{3}}(Y_{1-1} - Y_{11}), \frac{i}{2}\sqrt{\frac{8\pi}{3}}(Y_{1-1} + Y_{11}), \sqrt{\frac{4\pi}{3}}Y_{10}).
\end{aligned}$$

A.2 The Transition Matrix Elements

The derivation of the weak decay joint angular distribution, from which the polarization and angular distribution projections can be derived, begins with the transition matrix element. The transition matrix element for a weak decay from a spin-J state to a spin-$\frac{1}{2}$ state can be written as

$$\begin{aligned}
T_{\lambda m} &= \langle P\theta\phi; \frac{1}{2}\lambda \mid T \mid Jm\rangle \\
&= \langle P00; \frac{1}{2}\lambda \mid R^\dagger(\phi,\theta,0)T \mid Jm\rangle.
\end{aligned}$$

where T is the transition operator and $R^\dagger$ is the rotation operator. The completeness relation can be placed between the transition operator and the rotation operator, and noting that the Wigner Rotation Matrices ($D^J_{mm'}$) have the property that $\langle Jm' \mid R^\dagger \mid Jm\rangle = D^{J*}_{mm'}(\phi,\theta,0)$, the expression for the transition matrix element reduces to

$$T_{\lambda m} = \sum_{m'} \langle \frac{1}{2}\lambda \mid T \mid Jm'\rangle D^{J*}_{mm'}(\phi,\theta,0).$$

The final system can also be written in the helicity coordinate system, a helicity coordinate system which has the $\hat{z}$ axis along the opposite direction of the parent baryon in the daughter baryon's rest frame and thus implies $\theta = 0$, as

$$\begin{aligned}
T \mid Jm'\rangle = \sum_{L=J-\frac{1}{2}}^{J+\frac{1}{2}} \sum_{\lambda'=-\frac{1}{2}}^{\frac{1}{2}} A_L \langle \frac{1}{2}L\lambda', m'-\lambda' \mid Jm'\rangle \\
Y_{L,m'-\lambda'}(0,0) \mid \frac{1}{2}\lambda'\rangle.
\end{aligned}$$

The next step is to calculate $T_{\lambda m'}$. Since $Y_{Lm}(0,0) = \sqrt{\frac{2L+1}{4\pi}}\delta_{m,0}$ and $\langle \frac{1}{2}\lambda \mid \frac{1}{2}\lambda'\rangle = \delta_{\lambda,\lambda'}$, the transition matrix element $T_{\lambda m'}$ becomes

$$T_{\lambda m'} = \sum_{L=J-\frac{1}{2}}^{J+\frac{1}{2}} A_L \langle \frac{1}{2}L\lambda, 0 \mid Jm'\rangle \sqrt{\frac{2L+1}{4\pi}}\delta_{\lambda,m'}.$$

With the help of an expression for the Clebsch–Gordon coefficient in the previous equation (see section A.11), $T_{\lambda m'}$ can be written as

$$\begin{aligned}
T_{\lambda m'} &= \sum_{L=J-\frac{1}{2}}^{J+\frac{1}{2}} A_L \sqrt{\frac{2L+1}{4\pi}}\delta_{\lambda,m'}[\sqrt{\frac{L+1}{2L+1}}\delta_{J,L+\frac{1}{2}} + \sqrt{\frac{L}{2L+1}}\delta_{J,L-\frac{1}{2}}(\delta_{\lambda,\frac{1}{2}} - \delta_{\lambda,-\frac{1}{2}})] \\
&= \frac{1}{\sqrt{2}}\sqrt{\frac{2J+1}{4\pi}}\delta_{m',\lambda}[A_{J-\frac{1}{2}} + A_{J+\frac{1}{2}}(\delta_{\lambda,\frac{1}{2}} - \delta_{\lambda,-\frac{1}{2}})].
\end{aligned}$$

Therefore, by substituting $T_{\lambda m'}$ into the expression for $T_{\lambda m}$, the transition matrix element is found to be

$$T_{\lambda m} = \frac{1}{\sqrt{2}}\sqrt{\frac{2J+1}{4\pi}}[A_{J-\frac{1}{2}} + A_{J+\frac{1}{2}}(\delta_{\lambda,\frac{1}{2}} - \delta_{\lambda,-\frac{1}{2}})]D^{J*}_{m\lambda}(\phi,\theta,0) \tag{A.2}$$

and since $D^J_{m'm}(R^{-1}) = D^{J*}_{mm'}(R)$, it follows that

$$T^{\dagger}_{m'\lambda'} = \frac{1}{\sqrt{2}}\sqrt{\frac{2J+1}{4\pi}}[A_{J-\frac{1}{2}} + A_{J+\frac{1}{2}}(\delta_{\lambda',\frac{1}{2}} - \delta_{\lambda',-\frac{1}{2}})]^{*}D^J_{m'\lambda'}(\phi,\theta,0). \tag{A.3}$$

A.3 Decay from a Statistical Mixture of States

The density matrix for a system of identical particles

$$\rho = \sum_i \omega_i \mid \alpha^i\rangle\langle\alpha^i \mid$$

can be written in terms of a new basis $\mid Jm\rangle$ with the amplitudes a^i_m equal to the product of the basis kets, $\langle Jm \mid \alpha^i\rangle$, as

$$\rho = \sum_{imm'} \omega_i a^i_m a^{i*}_{m'} \mid Jm\rangle\langle Jm' \mid .$$

One is free to choose the basis in which to expand the density matrix. Here a basis described by Byers and Fenster [32] will be used following along a path similar to the one used by K. B. Luk [33] and H. T. Diehl [22]. The technique involves an expansion done in terms of the spherical tensor operators Q_{Lm}.

$$\rho = \sum_{L=0}^{2J}\sum_{m=-L}^{L} q^{*}_{Lm}Q_{Lm} \tag{A.4}$$

The spherical tensor operators are define as

$$Q_{Lm} = \sum_{mm'}(Q_{Lm})_{mm'} \mid Jm\rangle\langle Jm' \mid \tag{A.5}$$

$$q^{*}_{Lm} = tr(\rho Q^{\dagger}_{Lm}) \tag{A.6}$$

and it should be noted that tensor operators have the m–selection rule [34]

$$\langle Jm' \mid Q_{Lm} \mid Jm''\rangle = 0 \quad if \quad (m' \neq m + m'').$$

Using the Wigner–Eckhart Theorem, and assuming $\langle J\|Q_L\|J\rangle = \sqrt{2L+1}$,

$$\begin{aligned}\langle Jm' \mid Q_{Lm} \mid Jm''\rangle &= \frac{1}{\sqrt{2J+1}}\langle JL; m''m \mid Jm'\rangle\langle J\|Q_{Lm}\|J\rangle\\ &= \sqrt{\frac{2L+1}{2J+1}}\langle JL; m''m \mid Jm'\rangle,\end{aligned}$$

and using an expression relating the Clebsch-Gordon coefficient above to another one, the spherical tensor operator becomes

$$Q_{Lm} = \sum_{m'm''}(-1)^{J-m''}\langle JJm' - m'' \mid LM\rangle \mid Jm'\rangle\langle Jm'' \mid . \tag{A.7}$$

Next the density matrix must be transformed into the helicity frame. This can be accomplished by noting that the density matrix transforms as

$$\rho'(\theta,\phi) = T(\theta,\phi)\rho T^{\dagger}(\theta,\phi).$$

Since the density matrix elements are $\langle\mid\rho'\mid\rangle$, the transformed density matrix elements after expanding in states mm' are

$$\rho'_{\lambda\lambda'} = \sum_{m'm''} T_{\lambda m'}\rho_{m'm''}T^{\dagger}_{m''\lambda'} \tag{A.8}$$

$$\rho'_{m'm''} = \sum_{L=0}^{2J}\sum_{m=-L}^{L}\sum_{ln} q^{*}_{Lm}(-1)^{J-n}\langle JJl - n \mid Lm\rangle\langle Jm' \mid Jl\rangle\langle Jn \mid Jm''\rangle,$$

and so

$$\rho'_{m'm''} = \sum_{L=0}^{2J}\sum_{m=-L}^{L} q^{*}_{Lm}(-1)^{J-m''}\langle JJm' - m'' \mid Lm\rangle. \tag{A.9}$$

Combining the expressions for $\rho'_{m'm''}$, $T_{\lambda m'}$, and $T^{\dagger}_{m''\lambda'}$ the density matrix element in the helicity frame becomes

$$\rho'_{\lambda\lambda'} = \frac{2J+1}{8\pi}[A_{J-\frac{1}{2}} + A_{J+\frac{1}{2}}(\delta_{\lambda\frac{1}{2}} - \delta_{\lambda-\frac{1}{2}})][A_{J-\frac{1}{2}} + A_{J+\frac{1}{2}}(\delta_{\lambda'\frac{1}{2}} - \delta_{\lambda'-\frac{1}{2}})]^{*}$$
$$\sum_{L=0}^{2J}\sum_{m=-L}^{L}\sum_{m'm''} D^J_{m''\lambda'}(\phi,\theta,0)D^{J*}_{m'\lambda}(\phi,\theta,0)q^{*}_{Lm}(-1)^{J-m''}\langle JJm' - m'' \mid Lm\rangle. \tag{A.10}$$

Note that for a decay to a particle of spin-J there are $(2J+1)^2-1$ independent elements. The extra constraint that reduces the number of independent elements from $(2J+1)^2$ is $tr(\rho') = I$.

The product of the Wigner rotation matrices can be reduced by noting that the Clebsch-Gordon coefficients are real, and expanding the product in terms of the Clebsch-Gordon series [35]

$$\begin{aligned}\sum_{mm'}(-1)^{J-m'}D^{J*}_{m\lambda}D^{J}_{m'\lambda'} &= \sum_{L'lnmm'}(-1)^{J-m'}(-1)^{m'-\lambda'}D^{L'*}_{ln} \\ &\quad \langle L'l \mid JJm-l\rangle\langle JJm-l \mid Lm\rangle\langle JJ\lambda-\lambda' \mid L'n\rangle \\ &= \sum_{L'ln}(-1)^{J-\lambda'}D^{L'*}_{ln}\delta_{L'L}\delta_{ml}\langle JJ\lambda-\lambda' \mid L'n\rangle \\ &= \sum_{n}(-1)^{J-\lambda'}D^{L*}_{mn}\langle JJ\lambda-\lambda' \mid Ln\rangle.\end{aligned}$$

The Clebsch-Gordon coefficient in the previous equation is zero unless $n = \lambda - \lambda'$, therefore

$$\sum_{mm'}(-1)^{J-m'}D^{J*}_{m\lambda}D^{J}_{m'\lambda'} = (-1)^{J-\lambda'}D^{J*}_{m,\lambda-\lambda'}\langle JJ\lambda-\lambda' \mid L\lambda-\lambda'\rangle.$$

Substituting this equation into the density matrix element gives

$$\begin{aligned}\rho'_{\lambda\lambda'} = \frac{2J+1}{8\pi}&[A_{J-\frac{1}{2}} + A_{J+\frac{1}{2}}(\delta_{\lambda,\frac{1}{2}} - \delta_{\lambda,-\frac{1}{2}})][A_{J-\frac{1}{2}} + A_{J+\frac{1}{2}}(\delta_{\lambda',\frac{1}{2}} - \delta_{\lambda',-\frac{1}{2}})]^* \\ &\sum_{L=0}^{2J}\sum_{m=-L}^{L} q^*_{Lm}(-1)^{J-\lambda'}D^{J*}_{m,\lambda-\lambda'}\langle JJ\lambda-\lambda' \mid L\lambda-\lambda'\rangle. \quad \text{(A.11)}\end{aligned}$$

A.4 The Angular Distribution of the Daughter Baryon

The angular distribution of the daughter baryon can be found by taking the trace of the density matrix ρ'. Before taking the trace of the density matrix it is worthwhile to make a few definitions which simplify the algebra involved. First the weak decay asymmetry parameters are defined as

$$\alpha = 2Re(A^*_{J-\frac{1}{2}}A_{J+\frac{1}{2}})$$

$$\beta = 2Im(A^*_{J-\frac{1}{2}}A_{J+\frac{1}{2}})$$

$$\gamma = (\mid A_{J-\frac{1}{2}} \mid)^2 - (\mid A_{J+\frac{1}{2}} \mid)^2,$$

where the chosen normalization condition is

$$(\mid A_{J-\frac{1}{2}} \mid)^2 + (\mid A_{J+\frac{1}{2}} \mid)^2 = 1.$$

The normalization condition above was only chosen to simplify the algebra and does not effect the results of the calculations. Other useful quantities are the normalization constants n^J_{L0} and the spherical tensor terms t_{Lm}.

$$n^J_{L0} = (-1)^{J-\frac{1}{2}}\sqrt{\frac{2J+1}{4\pi}}\langle JJ\frac{1}{2} - \frac{1}{2} \mid L0\rangle$$

$$t_{Lm} = \sqrt{\frac{2J+1}{2L+1}}q_{Lm}$$

The angular distribution of the daughter baryon is $\sum_\lambda \rho'_{\lambda\lambda}(\theta,\phi)$, thus

$$\begin{aligned}I(\theta,\phi) = \frac{2J+1}{8\pi}&[A_{J-\frac{1}{2}} + A_{J+\frac{1}{2}}(\delta_{\lambda,\frac{1}{2}} - \delta_{\lambda,-\frac{1}{2}})][A_{J-\frac{1}{2}} + A_{J+\frac{1}{2}}(\delta_{\lambda,\frac{1}{2}} - \delta_{\lambda,-\frac{1}{2}})]^* \\ &\sum_{L=0}^{2J}\sum_{m=-L}^{L} q^*_{Lm}(-1)^{J-\lambda}D^{J*}_{m,0}\langle JJ\lambda-\lambda \mid L0\rangle.\end{aligned}$$

Using the relation

$$(-1)^{J-\lambda}\langle JJ\lambda-\lambda \mid L0\rangle = (-1)^{L-J-\lambda}\langle JJ-\lambda\lambda \mid L0\rangle,$$

and upon regrouping terms the angular distribution becomes

$$\begin{aligned}I(\theta,\phi) = \frac{2J+1}{8\pi}\sum_{L=0}^{2J}\sum_{m=-L}^{L} q^*_{Lm}&\sqrt{\frac{4\pi}{2L+1}}Y_{Lm}\langle JJ\frac{1}{2} - \frac{1}{2} \mid L0\rangle \\ &[(-1)^{J-\frac{1}{2}}[A_{J-\frac{1}{2}} + A_{J+\frac{1}{2}}][A_{J-\frac{1}{2}} + A_{J+\frac{1}{2}}]^* \\ &+ (-1)^{L-J+\frac{1}{2}}[A_{J-\frac{1}{2}} - A_{J+\frac{1}{2}}][A_{J-\frac{1}{2}} - A_{J+\frac{1}{2}}]^*].\end{aligned}$$

The angular distribution can be further reduced by substituting in the previously defined normalization constants and spherical tensors. After making these substitutions, the angular distribution becomes

$$I(\theta,\phi) = \sum_{L=0,even}^{2J} \sum_{m=-L}^{L} t^{*}_{Lm} n^{J}_{L0} Y_{Lm} + \alpha \sum_{L=0,odd}^{2J} \sum_{m=-L}^{L} t^{*}_{Lm} n^{J}_{L0} Y_{Lm}.$$

For the sake of clarity, the angular distribution can be rewritten as the sum of two functions of θ and ϕ.

$$I(\theta,\phi) = A(\theta,\phi) + \alpha B(\theta,\phi) \tag{A.12}$$

$$A(\theta,\phi) = \sum_{L=0,even}^{2J} \sum_{m=-L}^{L} t^{*}_{Lm} n^{J}_{L0} Y_{Lm} \tag{A.13}$$

$$B(\theta,\phi) = \sum_{L=0,odd}^{2J} \sum_{m=-L}^{L} t^{*}_{Lm} n^{J}_{L0} Y_{Lm} \tag{A.14}$$

A.5 Daughter Baryon Polarization

For a spin-$\frac{1}{2}$ particle, the density matrix can be written as a 2x2 matrix and thus has 3 independent elements.

$$\rho = \begin{pmatrix} a & b \\ c & d \end{pmatrix} = \frac{1}{2} I(\theta,\phi)(\vec{1} + \vec{\sigma}\cdot\vec{P})$$

The term $I\vec{P}_{\Lambda}\cdot\hat{\Lambda} = \rho'_{\frac{1}{2}\frac{1}{2}} - \rho'_{-\frac{1}{2}-\frac{1}{2}}$ can be determined in the same manner as the angular distribution term.

$$\begin{aligned} I\vec{P}_{\Lambda}\cdot\hat{\Lambda} = \frac{2J+1}{8\pi} \sum_{L=0}^{2J} \sum_{m=-L}^{L} q^{*}_{Lm} \sqrt{\frac{4\pi}{2L+1}} Y_{Lm} \langle JJ\frac{1}{2} - \frac{1}{2} \mid L0\rangle \\ [(-1)^{J-\frac{1}{2}}[A_{J-\frac{1}{2}} + A_{J+\frac{1}{2}}][A_{J-\frac{1}{2}} + A_{J+\frac{1}{2}}]^{*} \\ (-1)^{L-J-\frac{1}{2}}[A_{J-\frac{1}{2}} - A_{J+\frac{1}{2}}][A_{J-\frac{1}{2}} - A_{J+\frac{1}{2}}]^{*}] \end{aligned}$$

Once again by substituting in the definitions for the normalization constants and the spherical tensors, the above equation becomes

$$I\vec{P}_{\Lambda}\cdot\hat{\Lambda} = \alpha \sum_{L=0,even}^{2J} \sum_{m=-L}^{L} t^{*}_{Lm} n^{J}_{L0} Y_{Lm} + \sum_{L=0,odd}^{2J} \sum_{m=-L}^{L} t^{*}_{Lm} n^{J}_{L0} Y_{Lm}.$$

Notice that the two summation terms are the same as those found in the angular distribution formula, and that the only difference is the term which is multiplied by α.

$$I\vec{P}_{\Lambda}\cdot\hat{\Lambda} = \alpha A(\theta,\phi) + B(\theta,\phi) \tag{A.15}$$

The off–diagonal matrix elements are useful in determining the transverse components of the polarization. For example, $\rho'_{\frac{1}{2}-\frac{1}{2}} = \frac{1}{2} I(P_X - iP_Y)$ can be shown to be

$$\begin{aligned} \rho'_{\frac{1}{2},-\frac{1}{2}} = \frac{2J+1}{8\pi}[A_{J-\frac{1}{2}} + A_{J+\frac{1}{2}}][A_{J-\frac{1}{2}} - A_{J+\frac{1}{2}}]^{*} \\ \sum_{L=0}^{2J} \sum_{m=-L}^{L} q^{*}_{Lm} (-1)^{J+\frac{1}{2}} \langle JJ\frac{1}{2}\frac{1}{2} \mid L1\rangle D^{L*}_{m1}(\phi,\theta,0). \end{aligned}$$

Using another closely related normalization constant,

$$n^{J}_{L1} = (-1)^{J-\frac{1}{2}} \sqrt{\frac{2J+1}{4\pi}} \langle JJ\frac{1}{2}\frac{1}{2} \mid L1\rangle = \frac{2J+1}{\sqrt{L(L+1)}} n^{J}_{L0} \delta_{L,odd}$$

in the previous equation for $\rho'_{\frac{1}{2},-\frac{1}{2}}$, it follows that

$$\begin{aligned} \rho'_{\frac{1}{2},-\frac{1}{2}} = -(2J+1)[A_{J-\frac{1}{2}} + A_{J+\frac{1}{2}}][A_{J-\frac{1}{2}} - A_{J+\frac{1}{2}}]^{*} \\ \sum_{L=0}^{2J} \sum_{m=-L}^{L} \sqrt{\frac{2L+1}{4\pi L(L+1)}} t^{*}_{Lm} n^{J}_{L0} D^{L*}_{m1}(\phi,\theta,0). \end{aligned}$$

Now the definitions for the weak decay asymmetry parameters become useful. By substituting these definitions into the above equation, the density matrix element $\rho'_{\frac{1}{2},-\frac{1}{2}}$ becomes

$$\rho'_{\frac{1}{2},-\frac{1}{2}} = -\frac{1}{2}(2J+1)(\gamma + i\beta) \sum_{L=0}^{2J} \sum_{m=-L}^{L} \sqrt{\frac{2L+1}{4\pi L(L+1)}} t^{*}_{Lm} n^{J}_{L0} D^{L*}_{m1}(\phi,\theta,0).$$

The above density matrix element, along with its complex conjugate imply

$$I\vec{P_\Lambda}\cdot(\hat{X}-i\hat{Y}) = -(2J+1)(\gamma+i\beta)\sum_{L=0}^{2J}\sum_{m=-L}^{L}\sqrt{\frac{2L+1}{4\pi L(L+1)}}\, t^{*}_{Lm}n^{J}_{L0}D^{L*}_{m1}(\phi,\theta,0) \tag{A.16}$$

$$I\vec{P_\Lambda}\cdot(\hat{X}+i\hat{Y}) = (2J+1)(i\beta-\gamma)\sum_{L=0}^{2J}\sum_{m=-L}^{L}\sqrt{\frac{2L+1}{4\pi L(L+1)}}\, t_{Lm}n^{J}_{L0}D^{L}_{m1}(\phi,\theta,0). \tag{A.17}$$

A.6 The Joint Angular Distribution

Consider the case of a baryon decaying to a Λ baryon and a meson, where the Λ then decays into a P and a π^-. The joint angular distribution is then the product of the angular distribution of the daughter Λ from the original baryon, times the angular distribution of the P from the Λ decay. It is easy to see that the angular distribution of the P from the Λ decay is

$$I(\theta_p,\phi_p) = \frac{1}{4\pi}(1+\alpha_\Lambda\vec{P_\Lambda}\cdot\hat{p}).$$

Thus the joint angular distribution is

$$I(\theta_\Lambda,\phi_\Lambda,\theta_p,\phi_p) = \frac{1}{4\pi}(I_\Lambda+\alpha_\Lambda I_\Lambda\vec{P_\Lambda}\cdot\hat{p}).$$

The joint angular distribution can be expanded in terms of dot products with the helicity frame axis vectors,

$$I = \frac{1}{4\pi}(I_\Lambda+\alpha_\Lambda\vec{P_\Lambda}\cdot\hat{\Lambda}\hat{\Lambda}\cdot\hat{p}+\alpha_\Lambda\vec{P_\Lambda}\cdot\hat{X}\hat{X}\cdot\hat{p}+\alpha_\Lambda\vec{P_\Lambda}\cdot\hat{Y}\hat{Y}\cdot\hat{p}). \tag{A.18}$$

A.7 The Vector Polarization

The vector polarization can be determined by integrating over the solid angle $d\Omega_\Lambda$ in the S frame, where the S frame is a coordinate system with axes parallel to the lab axes but defined in the parent baryon's rest frame. The first term in the integration is

$$\frac{1}{4\pi}\int_0^{2\pi}\int_{-1}^{1}I_\Lambda d\Omega_\Lambda = \frac{1}{4\pi}\int_0^{2\pi}\int_{-1}^{1}(A+\alpha B)d\Omega_\Lambda.$$

Because of the orthogonality condition of the spherical harmonics when integrated over the solid angle, this term reduces to

$$\frac{1}{4\pi}\int_0^{2\pi}\int_{-1}^{1}I_\Lambda d\Omega_\Lambda = \frac{1}{4\pi}\sqrt{4\pi}n^{J}_{00}t_{00} = \frac{1}{4\pi}. \tag{A.19}$$

The second term, which involves the dot-product $\vec{P_\Lambda}\cdot\hat{\Lambda}$, is more complicated than the first term since the integration is being done in the S frame. The $\hat{\Lambda}$ axis must be written in terms of its components in the S frame. Expanding the dot-product $\hat{\Lambda}\cdot\hat{p}$ into the components $\Lambda_x p_x+\Lambda_y p_y+\Lambda_z p_z$, and using the orthogonality property of the Y_{Lm}'s, it is seen that

$$\frac{\alpha_\Lambda}{4\pi}\int_0^{2\pi}\int_{-1}^{1}I_\Lambda\vec{P_\Lambda}\cdot\hat{\Lambda}\hat{\Lambda}\cdot\hat{p}d\Omega_\Lambda = \frac{\alpha_\Lambda}{4\pi}\int_0^{2\pi}\int_{-1}^{1}(\alpha A+B)\hat{\Lambda}\cdot\hat{p}d\Omega_\Lambda$$
$$= \frac{\alpha_\Lambda}{4\pi}\sqrt{\frac{8\pi}{3}}\sum_{m=-1}^{1}n^{J}_{10}t_{1m}[\frac{1}{\sqrt{2}}(\delta_{m-1}-\delta_{m1})p_x+\frac{i}{\sqrt{2}}(\delta_{m-1}+\delta_{m1})p_y+\delta_{m0}p_z].$$

Summing over m, and substituting in an expression for n^{J}_{10}, the second term reduces to

$$\frac{\alpha_\Lambda}{4\pi}\frac{1}{2\sqrt{J(J+1)}}[\frac{1}{\sqrt{2}}(t_{1-1}-t_{11})p_x+\frac{i}{\sqrt{2}}(t_{m-1}+t_{11})p_y+t_{10}p_z]$$

or

$$\frac{\alpha_\Lambda}{4\pi}\frac{1}{2(J+1)}[\vec{P}\cdot\hat{p_x}+\vec{P}\cdot\hat{p_y}+\vec{P}\cdot\hat{p_z}] = \frac{\alpha_\Lambda}{4\pi}\frac{1}{2(J+1)}\vec{P}\cdot\hat{p}. \tag{A.20}$$

The third and fourth terms are not as simple as the second term. First expressions for $I_\Lambda P_x$ and $I_\Lambda P_y$ must be found. To do this, recall that the spherical tensors have the property $t^{*}_{Lm} = (-1)^{-m}t_{L-m}$. Therefore $I_\Lambda(P_x-iP_y)$ can be rewritten as

$$I\vec{P_\Lambda}\cdot(\hat{X}-i\hat{Y}) = -(2J+1)(\gamma+i\beta)\sum_{L=0}^{2J}\sum_{m=-L}^{L}\sqrt{\frac{2L+1}{4\pi L(L+1)}}\,(-1)^{-m}t_{L-m}n^{J}_{L0}D^{L*}_{m1}(\phi,\theta,0).$$

The two integrations to perform are

$$\frac{\alpha_\Lambda}{4\pi}\int_0^{2\pi}\int_{-1}^{1} I_\Lambda \vec{P_\Lambda}\cdot\hat{X}\hat{X}\cdot\hat{p}d\Omega_\Lambda = \frac{\alpha_\Lambda}{8\pi}\int_0^{2\pi}\int_{-1}^{1}\sum_{L=0odd}^{2J}\sum_{m=-L}^{L}$$
$$(2J+1)\sqrt{\frac{2L+1}{4\pi L(L+1)}}n^J_{Lo}[(-\gamma+i\beta)t_{Lm}D^L_{m1}$$
$$+(\gamma+i\beta)(-1)^{1-m}t_{L-m}D^{L*}_{m1}]\hat{X}\cdot\hat{p}d\Omega_\Lambda$$

and

$$\frac{\alpha_\Lambda}{4\pi}\int_0^{2\pi}\int_{-1}^{1} I_\Lambda \vec{P_\Lambda}\cdot\hat{Y}\hat{Y}\cdot\hat{p}d\Omega_\Lambda = \frac{i\alpha_\Lambda}{8\pi}\int_0^{2\pi}\int_{-1}^{1}\sum_{L=0odd}^{2J}\sum_{m=-L}^{L}$$
$$(2J+1)\sqrt{\frac{2L+1}{4\pi L(L+1)}}n^J_{Lo}[-(-\gamma+i\beta)t_{Lm}D^L_{m1}$$
$$+(\gamma+i\beta)(-1)^{1-m}t_{L-m}D^{L*}_{m1}]\hat{Y}\cdot\hat{p}d\Omega_\Lambda$$

Expanding the dot-products and performing the integrals over the solid angle give (see section A.10)

$$\frac{\alpha_\Lambda}{4\pi}\int_0^{2\pi}\int_{-1}^{1}(I_\Lambda\vec{P_\Lambda}\cdot\hat{X}\hat{X}\cdot\hat{p}+I_\Lambda\vec{P_\Lambda}\cdot\hat{Y}\hat{Y}\cdot\hat{p})d\Omega_\Lambda =$$
$$\frac{\alpha_\Lambda}{8\pi}\sqrt{\frac{2\pi}{3}}\sum_{m=-1}^{1}(2J+1)n^J_{L0}$$
$$[(-\gamma+i\beta)t_{Lm}[(\delta_{m1}-\delta_{m-1})p_x-(\delta_{m1}+\delta_{m-1})p_y-\sqrt{2}\delta_{m0}p_z]$$
$$+(\gamma+i\beta)(-1)^{1-m}t_{L-m}[(\delta_{m1}-\delta_{m-1})p_x+(\delta_{m1}+\delta_{m-1})p_y-\sqrt{2}\delta_{m0}p_z]].$$

After summing over m and substituting in for n^J_{10},

$$\frac{\alpha_\Lambda}{4\pi}\int_0^{2\pi}\int_{-1}^{1}(I_\Lambda\vec{P_\Lambda}\cdot\hat{X}\hat{X}\cdot\hat{p}+I_\Lambda\vec{P_\Lambda}\cdot\hat{Y}\hat{Y}\cdot\hat{p})d\Omega_\Lambda =$$
$$\frac{\alpha_\Lambda}{8\pi}\frac{1}{\sqrt{J(J+1)}}(2J+1)\gamma[\frac{1}{\sqrt{2}}(t_{1-1}-t_{11})p_x+\frac{i}{\sqrt{2}}(t_{11}+t_{1-1})p_y-t_{10}p_z]$$

$$=\frac{\alpha_\Lambda}{4\pi}\frac{1}{2(J+1)}(2J+1)\gamma[\vec{P}\cdot\hat{p_x}+\vec{P}\cdot\hat{p_y}+\vec{P}\cdot\hat{p_z}]. \tag{A.21}$$

Adding the terms together shows that the angular distribution of the proton from the decay chain in the daughter baryon's rest frame, which has axes parallel to the S frame, is

$$I(\theta_p,\phi_p)=\frac{1}{4\pi}(1+\frac{\alpha_\Lambda}{2(J+1)}[1+(2J+1)\gamma]\vec{P}\cdot\hat{p}). \tag{A.22}$$

Recalling that the angular distribution of P from Λ decay is $I=\frac{1}{4\pi}(1+\alpha_\Lambda\vec{P_\Lambda}\cdot\hat{p})$, the daughter Λ polarization is seen to be related to the parent baryon's polarization

$$\vec{P_\Lambda}=\frac{1}{2(J+1)}[1+(2J+1)\gamma]\vec{P}. \tag{A.23}$$

A.8 Λ Polarization from Ξ^- Decay

The polarization of the daughter baryons from the weak decay of spin $\frac{1}{2}$ baryons is just the ensemble average of the Pauli spin matrix for the system. The density matrix can be written as

$$\rho'=\begin{pmatrix} a & b \\ c & d \end{pmatrix}$$

where

$$tr(\rho'\sigma_X)=b+c \quad tr(\rho'\sigma_Y)=i(b-c)$$
$$tr(\rho'\sigma_\Lambda)=a-d \qquad tr(\rho')=I_\Lambda$$

Polarization can be thought of as the expectation value of the spin of an ensemble of particles, and so the polarization can be written as

$$[\vec{\sigma}]=\frac{tr(\rho'\vec{\sigma})}{tr(\rho')}=\frac{(b+c)\hat{X}+i(b-c)\hat{Y}+(a-d)\hat{\Lambda}}{(a+d)}. \tag{A.24}$$

Recall that is was previously shown that $a+b=A+\alpha B$ and $a-d=\alpha A+B$. Notice that $b=\frac{1}{2}I\vec{P_\Lambda}\cdot(\hat{X}-i\hat{Y})$ and that $c=\frac{1}{2}I\vec{P_\Lambda}\cdot(\hat{X}+i\hat{Y})$, which means

$$b=-\frac{1}{2}(i\beta+\gamma)(2J+1)\sum_{L=0,odd}^{2J}\sum_{m=-L}^{L}\sqrt{\frac{2L+1}{4\pi L(L+1)}}t^*_{Lm}n^J_{L0}D^{L*}_{m1}$$

$$c = \frac{1}{2}(i\beta - \gamma)(2J+1) \sum_{L=0,odd}^{2J} \sum_{m=-L}^{L} \sqrt{\frac{2L+1}{4\pi L(L+1)}} t_{Lm}\, n^J_{L0}\, D^L_{m1}.$$

Before continuing, it is important to note that $t^*_{Lm} = (-1)^{-m} t_{L-m}$ and that it has been shown $D^{L*}_{m1} = (-1)^{m-1} D^L_{-m-1}$, which together imply $t^*_{Lm} D^{L*}_{m1} = -t_{L-m} D^L_{-m-1}$. By summing symmetrically over m from $-L$ to L, the dummy index m can then be replaced by $-m$ to show that

$$\sum_{m=-L}^{L} t^*_{Lm} D^{L*}_{m1} = - \sum_{m=-L}^{L} t_{Lm} D^L_{m-1}.$$

The above relation can be used to show that

$$b = \frac{1}{2}(i\beta + \gamma)(2J+1) \sum_{L=0,odd}^{2J} \sum_{m=-L}^{L} \sqrt{\frac{2L+1}{4\pi L(L+1)}} t_{Lm}\, n^J_{L0}\, D^L_{m-1},$$

and also

$$(b+c) = \frac{1}{2}(2J+1) \sum_{L=0,odd}^{2J} \sum_{m=-L}^{L} \sqrt{\frac{2L+1}{4\pi L(L+1)}} t_{Lm}\, n^J_{L0}$$
$$[i\beta(D^L_{m-1} + D^L_{m1}) + \gamma(D^L_{m-1} - D^L_{m1})]$$

$$i(b-c) = \frac{1}{2}(2J+1) \sum_{L=0,odd}^{2J} \sum_{m=-L}^{L} \sqrt{\frac{2L+1}{4\pi L(L+1)}} t_{Lm}\, n^J_{L0}$$
$$[-\beta(D^L_{m-1} - D^L_{m1}) + i\gamma(D^L_{m-1} + D^L_{m1})].$$

Notice that in the equation for $i(b-c)$ can be obtained by inspection from the equation for $(b+c)$ by replacing γ by $-\beta$ and β by γ. There are several useful relations that help simplify the above equations and it is instructive to list them here. First, for the case of $J = \frac{1}{2}$ the term $\frac{1}{2}(2J+1)\sqrt{\frac{2L+1}{4\pi L(L+1)}} n^J_{L0}$, since it appears in a $\sum^{2J}_{L=0,odd}$, reduces to $\sqrt{\frac{3}{4\pi}}\sqrt{\frac{1}{2}} n^{\frac{1}{2}}_{10}$ or $\frac{1}{4\pi}\sqrt{\frac{3}{2}}$. There are several useful relations involving dot–products with the helicity frame axes.

$$(\vec{P} \times \hat{\Lambda}\,) \cdot \hat{Y} \;=\; \vec{P}_z \sin\theta - \vec{P}_y \cos\theta \sin\phi - \vec{P}_x \cos\theta\cos\phi$$
$$(\vec{P} \times \hat{\Lambda}\,) \cdot \hat{X} \;=\; \vec{P}_y \cos\phi - \vec{P}_x \sin\phi$$

$$[\hat{\Lambda}\; \times (\vec{P} \times \hat{\Lambda}\,)] \cdot \hat{X} \;=\; \vec{P}_y \cos\theta \sin\phi + \vec{P}_x \cos\theta \cos\phi - \vec{P}_z \sin\theta$$
$$[\hat{\Lambda}\; \times (\vec{P} \times \hat{\Lambda}\,)] \cdot \hat{Y} \;=\; -\vec{P}_x \sin\phi + \vec{P}_y \cos\phi.$$

Another useful relation is

$$D^L_{m-1} \pm D^L_{m1} = e^{-im\phi}(d^L_{m-1} \pm d^L_{m1}).$$

Now simplifying the terms for $J = \frac{1}{2}$

$$I_\Lambda = (a+d) = n^{\frac{1}{2}}_{00} t^*_{00} Y_{00} + \alpha_\Xi n^{\frac{1}{2}}_{10}[t^*_{1-1} Y_{1-1} + t^*_{10} Y_{10} + t^*_{11} Y_{11}]$$

$$= \frac{1}{4\pi}(1 + \alpha_\Xi[\sqrt{\frac{3}{2}}(t_{1-1} - t_{11}) \sin\theta\cos\phi$$
$$+ i\sqrt{\frac{3}{2}}(t_{1-1} + t_{11}) \sin\theta \sin\phi + \sqrt{3} t_{10} \cos\theta]).$$

If the definitions for the coordinate axes are substituted into this equation, the angular distribution becomes

$$I_\Lambda = \frac{1}{4\pi}(1 + \alpha_\Xi \vec{P}_\Xi \cdot \hat{\Lambda}). \tag{A.25}$$

Also by comparison

$$(a-d) = \frac{1}{4\pi}(\alpha_\Xi + \vec{P}_\Xi \cdot \hat{\Lambda}\,) \tag{A.26}$$

Now for the terms $(b+c)$ and $i(b-c)$. The term $(b+c)$ can be reduced as follows

$$(b+c) = \frac{1}{4\pi}\sqrt{\frac{3}{2}}(t_{10}[i\beta(d^1_{0-1} + d^1_{01}) + \gamma(d^1_{0-1} - d^1_{01})] + t_{1-1}[i\beta e^{i\phi}(d^1_{-1-1} + d^1_{-11})$$
$$+ \gamma e^{i\phi}(d^1_{-1-1} - d^1_{-11})] + t_{11}[i\beta e^{-i\phi}(d^1_{1-1} + d^1_{11}) + \gamma e^{-i\phi}(d^1_{1-1} - d^1_{11})])$$

and after replacing the rotation matrices

$$(b+c) = \frac{1}{4\pi}\sqrt{\frac{3}{2}}(-\sqrt{2} t_{10} \gamma \sin\theta + i\beta \cos\phi[t_{1-1} + t_{11}] - \beta \sin\phi[t_{1-1} - t_{11}]$$
$$+ \gamma \cos\theta\cos\phi[t_{1-1} - t_{11}] + i\gamma \cos\theta \cos\phi[t_{1-1} + t_{11}]).$$

Finally, the spherical tensors can be replaced by polarization components to give

$$(b+c) = \frac{1}{4\pi}(-P_z\gamma\sin\theta + P_y\beta\cos\phi - P_x\beta\sin\phi + P_x\gamma\cos\theta\cos\phi + P_y\gamma\cos\theta\sin\phi).$$

By letting γ go to $-\beta$ and β to γ above

$$i(b-c) = \frac{1}{4\pi}(P_z\beta\sin\theta + P_y\gamma\cos\phi - P_x\gamma\sin\phi - P_x\beta\cos\theta\cos\phi - P_y\beta\cos\theta\sin\phi).$$

Both of these relations can be rewritten in terms of dot-products with the helicity frame axes.

$$(b+c) = \frac{1}{4\pi}(\gamma[\hat{\Lambda} \times (\vec{P}\times\hat{\Lambda})]\cdot\hat{X} + \beta[\vec{P}\times\hat{\Lambda}]\cdot\hat{X})$$

$$i(b-c) = \frac{1}{4\pi}(\gamma[\hat{\Lambda} \times (\vec{P}\times\hat{\Lambda})]\cdot\hat{Y} + \beta[\vec{P}\times\hat{\Lambda}]\cdot\hat{Y})$$

Thus the Λ polarization from the decay of an ensemble of Ξ^- particles is

$$\vec{P}_\Lambda = \frac{1}{1+\alpha_\Xi\vec{P}_\Xi\cdot\hat{\Lambda}}[(\alpha_\Xi + \vec{P}_\Xi\cdot\hat{\Lambda})\hat{\Lambda} + \beta_\Xi(\vec{P}_\Xi x\hat{\Lambda}) + \gamma_\Xi[\hat{\Lambda}\, x(\vec{P}_\Xi x\hat{\Lambda})]]. \quad \text{(A.27)}$$

The above equation is quit general and can be applied to any decay of a spin-$\frac{1}{2}$ baryon to a spin-$\frac{1}{2}$ baryon and a spin-0 meson by substituting the parent baryon for the Ξ^- and the daughter baryon for the Λ.

A.9 Projecting the Angular Distribution on the S' axes

Upon integrating the joint angular distribution over ϕ_Λ in the helicity frame, all of the terms with $m \neq 0$ vanish [36].

$$\begin{aligned} I(\theta_\Lambda,\phi_p,\theta_p) &= \frac{1}{2}[(1+\alpha_\Lambda\alpha\hat{\Lambda}\cdot\hat{p})\sum_{L=0even}^{2J} n^J_{L0}t^*_{L0}Y_{L0} \\ &+ (\alpha + \alpha_\Lambda\hat{\Lambda}\cdot\hat{p})\sum_{L=0odd}^{2J} n^J_{L0}t^*_{L0}Y_{L0} \\ &- (2J+1)\alpha_\Lambda(\beta\hat{Y}\cdot\hat{p} - \gamma\hat{X}\cdot\hat{p})\sum_{L=0odd}^{2J} n^J_{L0}t_{L0}Y_{L1}e^{-i\phi}\sqrt{\frac{1}{L(L+1)}}] \end{aligned} \quad \text{(A.28)}$$

If $J = \frac{1}{2}$, as it does for Ξ^-, the distribution reduces to:

$$\begin{aligned} I(\theta_\Lambda,\phi_p,\theta_p) &= \frac{1}{8\pi}[(1+\alpha_\Xi P_\Xi\cos\theta_\Lambda) + \alpha_\Lambda\hat{\Lambda}\cdot\hat{p} + (\alpha_\Xi + P_\Xi\cos\theta_\Lambda) \\ &+ \alpha_\Lambda P_\Xi\sin\theta_\Lambda(\beta_\Xi\hat{Y}\cdot\hat{p} - \gamma_\Xi\hat{X}\cdot\hat{p})] \end{aligned} \quad \text{(A.29)}$$

In the previous equation the $\hat{z}$ axis is chosen to be along the polarization direction which means $P_\Xi = \vec{P}_\Xi\cdot\hat{n} = \sqrt{3}t_{10}$ since $P_{z\Xi} = \sqrt{\frac{J+1}{J}}t_{10}$. While the spin of the Ω^- has not been measured, it is interesting to examine the angular distribution assuming $j = \frac{3}{2}$ as expected from SU(3). From now on it will be assumed that the polarization is along the $\hat{z}$ axis. The result is:

$$\begin{aligned} I(\theta_\Lambda,\phi_p,\theta_p) &= \frac{1}{8\pi}((1+\alpha_\Lambda\alpha_\Omega\hat{\Lambda}\cdot\hat{p})[1-\sqrt{5}t_{20}(\frac{3}{2}\cos^2\theta_\Lambda - \frac{1}{2})] \\ &+ (\alpha_\Omega + \alpha_\Lambda\hat{\Lambda}\cdot\hat{p})[\frac{3}{5}P_\Omega\cos\theta_\Lambda - 3\sqrt{\frac{7}{5}}t_{30}(\frac{5}{3}\cos^3\theta_\Lambda - \frac{3}{2}\cos\theta_\Lambda)] \\ &+ 2\alpha_\Lambda(\beta_\Omega\hat{Y}\cdot\hat{p} - \gamma_\Omega\hat{X}\cdot\hat{p})[\frac{3}{5}P_\Omega\sin\theta_\Lambda - \frac{3}{4}\sqrt{\frac{7}{5}}t_{30}\sin\theta_\Lambda(5\cos^2\theta_\Lambda - 1)]) \end{aligned} \quad \text{(A.30)}$$

To measure the weak decay parameter α, the angular distribution can be projected onto the $\hat{\Lambda}$ axis by integrating over ϕ_p where $\cos\theta_p = \hat{\Lambda}\cdot\hat{p}$ in the Λ rest frame. Projections can be made onto other helicity frame axes in the same manner. For instance, to project onto the $\hat{Y}$ axis, define $\cos\theta_y = \hat{Y}\cdot\hat{p}$ and integrate over ϕ_y. For the case $J = \frac{1}{2}$ the angular distributions after integrating are:

$$I(\theta_\Lambda,\hat{\Lambda}\cdot\hat{p}) = \frac{1}{4}[(1+\alpha_\Xi P_\Xi\cos\theta_\Lambda) + \alpha_\Lambda\hat{\Lambda}\cdot\hat{p}(\alpha_\Xi + P_\Xi\cos\theta_\Lambda)] \quad \text{(A.31)}$$

$$I(\theta_\Lambda,\hat{X}\cdot\hat{p}) = \frac{1}{4}(1+\alpha_\Xi P_\Xi\cos\theta_\Lambda - \alpha_\Lambda P_\Xi\gamma_\Xi\sin\theta_\Lambda\hat{X}\cdot\hat{p}) \quad \text{(A.32)}$$

$$I(\theta_\Lambda,\hat{Y}\cdot\hat{p}) = \frac{1}{4}(1+\alpha_\Xi P_\Xi\cos\theta_\Lambda + \alpha_\Lambda P_\Xi\beta_\Xi\sin\theta_\Lambda\hat{Y}\cdot\hat{p}) \quad \text{(A.33)}$$

For the case $J = \frac{3}{2}$, the distributions are more complicated due to higher spin terms. In this case, the angular distributions after the appropriate ϕ integration become:

$$\begin{aligned} I(\theta_\Lambda,\hat{\Lambda}\cdot\hat{p}) &= \frac{1}{4}((1+\alpha_\Lambda\alpha_\Omega\hat{\Lambda}\cdot\hat{p})[1-\sqrt{5}t_{20}(\frac{3}{2}\cos^2\theta_\Lambda - \frac{1}{2})] \\ &+ (\alpha_\Omega + \alpha_\Lambda\hat{\Lambda}\cdot\hat{p})[\frac{3}{5}P_\Omega\cos\theta_\Lambda - 3\sqrt{\frac{7}{5}}t_{30}(\frac{5}{3}\cos^3\theta_\Lambda - \frac{3}{2}\cos\theta_\Lambda)]) \end{aligned} \quad \text{(A.34)}$$

$$
\begin{aligned}
I(\theta_\Lambda, \hat{X}\cdot\hat{p}) &= \frac{1}{4}(1 - \sqrt{5}t_{20}[\frac{3}{2}\cos^2\theta_\Lambda - \frac{1}{2}] \\
&\quad + \alpha_\Omega[\frac{3}{5}P_\Omega \cos\theta_\Lambda - 3\sqrt{\frac{7}{5}}t_{30}(\frac{5}{3}\cos^3\theta_\Lambda - \frac{3}{2}\cos\theta_\Lambda)] \\
&\quad - 2\alpha_\Lambda\gamma_\Omega\hat{X}\cdot\hat{p}\sin\theta_\Lambda\,[\frac{3}{5}P_\Omega - \frac{3}{4}\sqrt{\frac{7}{5}}t_{30}(5\cos^2\theta_\Lambda - 1)]) \quad \text{(A.35)}
\end{aligned}
$$

$$
\begin{aligned}
I(\theta_\Lambda, \hat{Y}\cdot\hat{p}) &= \frac{1}{4}(1 - \sqrt{5}t_{20}(\frac{3}{2}\cos^2\theta_\Lambda - \frac{1}{2}) \\
&\quad + \alpha_\Omega[\frac{3}{5}P_\Omega \cos\theta_\Lambda - 3\sqrt{\frac{7}{5}}t_{30}(\frac{5}{3}\cos^3\theta_\Lambda - \frac{3}{2}\cos\theta_\Lambda)] \\
&\quad + 2\alpha_\Lambda\beta_\Omega\hat{Y}\cdot\hat{p}\sin\theta_\Lambda\,[\frac{3}{5}P_\Omega - \frac{3}{4}\sqrt{\frac{7}{5}}t_{30}(5\cos^2\theta_\Lambda - 1)]) \quad \text{(A.36)}
\end{aligned}
$$

The next step is to integrate over $\cos\theta_\Lambda$. Notice that all terms with only odd powers of $\cos\theta_\Lambda$ drop out. Terms which go as an even power of $\cos\theta_\Lambda$, or as $\sin\theta_\Lambda$ remain. Also terms which are a product of the $\sin\theta_\Lambda$ and an even power of $\cos\theta_\Lambda$ survive the integration. After doing the integrations for the case $J = \frac{1}{2}$, the angular projections onto the helicity frame axes are found to be:

$$
\begin{aligned}
I(\hat{\Lambda}\cdot\hat{p}) &= \frac{1}{2}(1 + \alpha_\Lambda\alpha_\Xi\cos\theta_p) && \text{(A.37)} \\
I(\hat{X}\cdot\hat{p}) &= \frac{1}{2}(1 - \frac{\pi}{4}\alpha_\Lambda P_\Xi\gamma_\Xi\hat{X}\cdot\hat{p}) && \text{(A.38)} \\
I(\hat{Y}\cdot\hat{p}) &= \frac{1}{2}(1 + \frac{\pi}{4}\alpha_\Lambda P_\Xi\beta_\Xi\hat{Y}\cdot\hat{p}) && \text{(A.39)}
\end{aligned}
$$

The results for the case $j = \frac{3}{2}$ are:

$$
\begin{aligned}
I(\hat{\Lambda}\cdot\hat{p}) &= \frac{1}{2}(1 + \alpha_\Lambda\alpha_\Omega\cos\theta_p) && \text{(A.40)} \\
I(\hat{X}\cdot\hat{p}) &= \frac{1}{2}[1 - \frac{3\pi}{10}\alpha_\Lambda\gamma_\Omega\hat{X}\cdot\hat{p}(P_\Omega - \frac{5}{16}\sqrt{\frac{7}{5}}t_{30})] && \text{(A.41)} \\
I(\hat{Y}\cdot\hat{p}) &= \frac{1}{2}[1 + \frac{3\pi}{10}\alpha_\Lambda\beta_\Omega\hat{Y}\cdot\hat{p}(P_\Omega - \frac{5}{16}\sqrt{\frac{7}{5}}t_{30})] && \text{(A.42)}
\end{aligned}
$$

A.10 Wigner Rotation Matrices D^J_{Lm}

The rotation angles can be written in terms of the Euler angles α, β, γ and have the following orthogonality condition:

$$\int_0^{2\pi} d\alpha \int_0^{2\pi} d\gamma \int_0^{\pi} \sin\beta d\beta D^{J*}_{mn}(\alpha,\beta,\gamma) D^{J'}_{m'n'}(\alpha,\beta,\gamma) = \delta_{mm'}\delta_{nn'}\delta_{JJ'}\frac{8\pi^2}{2J+1}. \quad \text{(A.43)}$$

The Wigner rotation matrices in the previous equation are

$$D^J_{m'm}(\alpha,\beta,\gamma) = e^{-i(m'\alpha+m\gamma)}d^J_{m'm}.$$

In polar coordinates, $\alpha = \phi$, $\beta = \theta$, $\gamma = 0$ and looking at $n' = n = 1$ the orthogonality condition becomes

$$\int_0^{2\pi} d\phi \int_0^{\pi} \sin\theta d\theta D^{J*}_{m1}(\phi,\theta,0) D^{J'}_{m1}(\phi,\theta,0) = \delta_{mm'}\delta_{JJ'}\frac{4\pi}{2J+1}. \quad \text{(A.44)}$$

Some useful properties of the $D^J_{m'm}$'s and the $d^J_{m'm}$'s are:

$$
\begin{aligned}
d^{J*}_{m'm} &= d^J_{m'm} \\
d^J_{m'm} &= (-1)^{m-m'}d^J_{-m'-m} \\
D^J_{m'm} &= (-1)^{m-m'}D^{J*}_{-m'-m} \\
D^J_{m'm}(R^{-1}) &= D^{J*}_{mm'}(R)
\end{aligned}
$$

A useful relationship between the spherical harmonics and the rotation matrices [37]

$$D^{L*}_{m0}(\phi,\theta,0) = \sqrt{\frac{4\pi}{2L+1}}Y_{Lm}(\theta,\phi)$$

In deriving the formulas for the vector polarization and the angular distribution projections, the $J = \frac{1}{2}$ rotation matrices can be used to rewrite the axis–vectors. First note that for $J = 1$, the $D^J_{m'm}$'s reduce to:

$$D^1_{11} = e^{-i\phi}(\frac{1+\cos\theta}{2}) \quad , \quad D^{1*}_{11} = e^{i\phi}(\frac{1+cos\theta}{2})$$

$$D^1_{1-1} = e^{-i\phi}(\frac{1-\cos\theta}{2}) \quad , \quad D^{1*}_{1-1} = e^{i\phi}(\frac{1-\cos\theta}{2})$$

$$D^1_{-11} = e^{i\phi}(\frac{1-\cos\theta}{2}) \quad , \quad D^{1*}_{-11} = e^{-i\phi}(\frac{1-\cos\theta}{2})$$

$$D^1_{01} = (\frac{\sin\theta}{\sqrt{2}})$$

The appropriate spherical angle terms can be related to the rotation matrices as follows:

$$\begin{aligned} -\sin\phi_\Lambda &= \frac{i}{2}(D^{1*}_{11} - D^1_{11} + D^1_{-11} - D^{1*}_{-11}) \\ \cos\phi_\Lambda &= \frac{1}{2}(D^{1*}_{11} + D^1_{11} + D^1_{-11} + D^{1*}_{-11}) \\ \cos\phi_\Lambda \ \cos\theta_\Lambda &= \frac{1}{2}(D^{1*}_{11} - D^{1*}_{-11} + D^1_{11} - D^1_{-11}) \\ \sin\phi_\Lambda \ \cos\theta_\Lambda &= \frac{i}{2}(D^1_{11} - D^{1*}_{11} + D^1_{-11} - D^{1*}_{-11}) \\ -\sin\theta_\Lambda &= -\sqrt{2}D^1_{01} \end{aligned}$$

A.11 The Normalization Constants n^J_{L0}

The normalization constant n^J_{L0} is defined as

$$n^J_{L0} = (-1)^{J-\frac{1}{2}}\sqrt{\frac{2J+1}{4\pi}}\langle JJ\frac{1}{2} - \frac{1}{2} \mid L0\rangle \tag{A.45}$$

It should be noted that $n^{J*}_{L0} = n^J_{L0}$ since Clebsch-Gordon coefficients are real. The fact that the n_{L0}'s are real is consistent with the concept of a normalization constant. In the case of $L = 1$ a useful formula is [33]

$$n^J_{10} = \sqrt{\frac{3J}{4\pi(J+1)}\frac{1}{2J}}$$

We can define another normalization constant

$$n^J_{L1} = (-1)^{J-\frac{1}{2}}\sqrt{\frac{2J+1}{4\pi}}\langle JJ\frac{1}{2}\frac{1}{2} \mid L1\rangle$$

and it is easily shown that with this definition

$$n^J_{L1} = \frac{2J+1}{\sqrt{L(L+1)}}n^J_{L0}\delta_{L,odd}$$

From a table of Clebsch-Gordon coefficients it is easy to show that:

$$\begin{aligned} n^{\frac{1}{2}}_{00} &= \sqrt{\frac{1}{4\pi}} & n^{\frac{1}{2}}_{10} &= \sqrt{\frac{1}{4\pi}} \\ n^{\frac{3}{2}}_{00} &= \sqrt{\frac{1}{4\pi}} & n^{\frac{3}{2}}_{10} &= \sqrt{\frac{1}{20\pi}} \\ n^{\frac{3}{2}}_{20} &= -\sqrt{\frac{1}{4\pi}} & n^{\frac{3}{2}}_{30} &= -\sqrt{\frac{9}{20\pi}} \end{aligned}$$

$$\langle JJm - m \mid 00\rangle = (-1)^{J-m}\sqrt{\frac{1}{2J+1}} \tag{A.46}$$

Other relations useful in manipulating the normalization terms are:

$$\langle\frac{1}{2}L\pm\frac{1}{2}0 \mid J,\pm\frac{1}{2}\rangle = \sqrt{\frac{L+1}{2L+1}}\delta_{J,L+\frac{1}{2}}\pm\sqrt{\frac{L}{2L+1}}\delta_{J,L-\frac{1}{2}} \tag{A.47}$$

$$(-1)^{J-k}\langle JJm - k \mid LM\rangle = (-1)^L\langle LJMk \mid Jm\rangle\sqrt{\frac{2L+1}{2J+1}} \tag{A.48}$$

A.12 Properties of the t_{Lm} Spherical Harmonics

The t_{Lm}'s are defined to be

$$t_{Lm} = \sqrt{\frac{2J+1}{2L+1}}q_{Lm},$$

where the normalization is chosen so that $t_{00} = 1$. Since the t_{Lm}'s are spherical tensors, they also have the property

$$t^*_{Lm} = (-1)^{-m}t_{L-m}.$$

The vector polarization can be written in terms of the t_{Lm}'s as follows;

$$P_x = \frac{1}{\sqrt{2}}\sqrt{\frac{J+1}{J}}(t_{1-1} - t_{11})$$

$$P_y = \frac{i}{\sqrt{2}}\sqrt{\frac{J+1}{J}}(t_{1-1} + t_{11})$$

$$P_z = \sqrt{\frac{J+1}{J}}t_{10}$$

References

[1] J. Donoghue *et. al.* Low-energy weak interactions of quarks. *Phys. Rep.*, **131**:320, 1986.

[2] Mahiko Suzuki. Pole approximation to the decay of the Ω^- particle ($\simeq$ 1680 MeV). *Prog of Theor. Phys.*, **32**(1):138, 1964.

[3] T. D. Lee and C. N. Yang. General partial wave analysis of the decay of a hyperon of spin $\frac{1}{2}$. *Phys. Rev.*, **108**:1645, 1957.

[4] J. D. Jackson. *Classical Electrodynamics, 2nd edition*, chapter 11.11, pages 556–560. John Wiley & Sons, 1975. See equations 11.157-11.159 for the relationship between a 3-vector spin in the particle rest frame and a 4-vector spin in an arbitrary frame.

[5] O. E. Overseth and S. Pakvasa. Final-state interactions in nonleptonic hyperon decays. *Phys. Rev.*, **184**:1663, 1969.

[6] R. L. Cool *et. al.* Measurement of the magnetic moment and of the decay parameters of the Ξ^- hyperon. *Phys. Rev.*, **D10**:792, 1974.

[7] K. B. Luk *et. al.* New measurements of properties of the Ω^- hyperon. *Phys. Rev.*, **D38**:19, 1988.

[8] H. T. Diehl *et. al.* Measurement of the Ω^- magnetic moment. *Phys. Rev. Lett.*, **67**:804, 1991.

[9] Jewan Kim *et. al.* Polarization effects in spin-$\frac{3}{2}$ hyperon decay. *Phys. Rev. D*, **46**:1060, 1992.

[10] R. J. Hemingway *et. al.* Ω^- produced in K^-p reactions at 4.2 GeV/c. *Nucl. Phys.*, **B142**:205, 1978.

[11] M. Deutschman *et. al.* Spin and lifetime of the Ω^- hyperon. *Phys. Lett.*, **73B**:96, 1978.

[12] Keith Alan Thorne. *Precision Measurement of the Lifetime and Decay Asymmetry of the Cascade-Zero Baryon.* PhD thesis, University Of Minnesota, 1990. (unpublished).

[13] M. Bourquin *et. al.* Measurements of the Ω^- decay properties in the CERN SPS hyperon beam. *Nuc. Phys..*, **B241**:1, 1984.

[14] M. Lusignoli *et. al.* Nonleptonic decays of Ω^-. *Phys. Lett.*, **132B**:178, 1983.

[15] B. Stech and Q. P. Xu. Hyperon decays and quark-quark correlations. *Z. Phys. C.*, **49**:491, 1991.

[16] K. B. Luk *et. al.* Polarization of Ω^- hyperons produced in 800-GeV proton-beryllium collisions. *Phys. Rev. Lett.*, **70**:900, 1993.

[17] J. Duryea *et. al.* Polarization of Ξ^- hyperons produced by 800-GeV protons. *Phys. Rev. Lett.*, **67**:1193, 1991.

[18] G. Bunce *et. al.* Λ^0 hyperon polarization in inclusive production by 300-GeV protons on beryllium. *Phys. Rev. Lett.*, **36**:1113, 1976.

[19] Jeffrey Walton Duryea. *A Precision Measurement of the Polarization and Magnetic Moment of the Cascade-Minus Hyperon.* PhD thesis, University Of Minnesota, 1991. (unpublished).

[20] H. Haggerty *et. al.* A readout for multiwire proportional chambers. *NIM*, **115**:157, 1974.

[21] Data Acquisition Software Group. Vaxonline system user's guide. Technical Memo PN 252, Fermilab, 1987. (unpublished).

[22] Herman Thomas Diehl. *Omega Minus Polarization and Magnetic Moment.* PhD thesis, Rutgers, 1990. (unpublished).

[23] Particle Data Group. Review of particle properties. *Phys. Rev.*, **D45**:1, 1992.

[24] G. Bunce *et. al.* A monte carlo/data hybrid: A general technique to measure detection efficiency. *NIM*, **172**:553, 1980.

[25] R. Rameika *et. al.* Measurements of production polarization and decay asymmetry for Ξ^- hyperons. *Phys. Rev.*, **D33**:3172, 1986.

[26] P. M. Ho *et. al.* Production polarization and magnetic moment of $\overline{\Xi}^+$ antihyperons produced by 800-GeV/c protons. *Phys. Rev. Lett.*, **65**:1713, 1990.

[27] Noah Benjamin Wallace. *A Precesion Measurement of the Omega-Minus Magnetic Moment.* PhD thesis, University Of Minnesota, 1994 (Work in Progress).

[28] David McDill Woods. *A Study of Polarization in Hyperon Production Processes.* PhD thesis, University Of Minnesota, 1994 (Work in Progress).

[29] J. Duryea *et. al.* Precise measurement of the Ξ^- magnetic moment. *Phys. Rev. Lett.*, **68**:768, 1992.

[30] Regina Abby Rameika. *The Polarization and Magnetic Moment of the Ξ^- Hyperon.* PhD thesis, Rutgers, 1981. (unpublished).

[31] T. A. DeGrand *et. al.* Hyperon polarization asymmetry: Polarized beams and Ω^- production. *Phys. Rev.*, **D32**:2445, 1985.

[32] Byers and Fenster. Determination of spin and decay parameters of fermion states. *Phys. Rev. Lett.*, 11:52, 1963.

[33] Kam-Biu Luk. *A Study of the Omega Minus Hyperon.* PhD thesis, Rutgers, 1983. (unpublished).

[34] J. J. Sakurai. *Modern Quantum Mechanics*, page 238. Benjamin/Cummings Publishing Company, Inc., 1985.

[35] J. J. Sakurai. *Modern Quantum Mechanics*, chapter 3.7, page 216. Benjamin/Cummings Publishing Company, Inc., 1985. See equation 3.7.69.

[36] J. P. Berge et. al. Some properties of Ξ^- and Ξ^0 hyperons produced in K^-p interactions between 1.05 and 1.7 BeV/c. *Phys. Rev.*, **147**:945, 1966.

[37] J. J. Sakurai. *Modern Quantum Mechanics*, page 203. Benjamin/Cummings Publishing Company, Inc., 1985.